UC Santa Cruz
UC Santa Cruz Electronic Theses and Dissertations

Title
Exploration of Low-Temperature Hydrothermal Processes in North Pond, Mid-Atlantic

Permalink
https://escholarship.org/uc/item/3sf829qw

Author
Price, Adam Nicholas

Publication Date
2022

Supplemental Material
https://escholarship.org/uc/item/3sf829qw#supplemental

Copyright Information
This work is made available under the terms of a Creative Commons Attribution-NonCommercial-NoDerivatives License, availalbe at
https://creativecommons.org/licenses/by-nc-nd/4.0/

Peer reviewed|Thesis/dissertation

UNIVERSITY OF CALIFORNIA
SANTA CRUZ

EXPLORATION OF LOW-TEMPERATURE HYDROTHERMAL PROCESSES IN NORTH POND, MID-ATLANTIC

A dissertation submitted in partial satisfaction of the
requirements for the degree of

DOCTOR OF PHILOSOPHY

in

EARTH SCIENCES

by

Adam Nicholas Price

December 2022

The Dissertation of Adam Nicholas Price
is approved:

Andrew T. Fisher, Chair

Philip H. Stauffer

Francis Nimmo

Peter Biehl
Vice Provost and Dean of Graduate Studies

Copyright © by
Adam Nicholas Price
2022

Table of Contents

List of Figures and Tables

Chapter 1: Numerical Simulation of Cool Hydrothermal Processes in the Upper Volcanic Crust Beneath a Marine Sediment Pond: North Pond, North Atlantic Ocean

Chapter 2: The Influence of Permeability Anisotropy in the Upper Ocean Crust on Advective Heat Transport by a Ridge-flank Hydrothermal System

Chapter 3: Construction of Geologically Realistic, Three-Dimensional Meshes for Simulation of Subseafloor Hydrothermal Circulation, Including Bathymetric Relief and Patchy Sediment

Appendix A: Supporting Information for "Numerical Simulation of Cool Hydrothermal Processes in the Upper Volcanic Crust Beneath a Marine Sediment Pond: North Pond, North Atlantic Ocean"

Appendix B: Supplemental Information for "Construction of Geologically Realistic, Three-Dimensional Meshes for Simulation of

Subseafloor Hydrothermal Circulation, Including Bathymetric Relief and Patchy Sediment”

Abstract

Exploration of Low-Temperature Hydrothermal Processes in North Pond, Mid-Atlantic

Adam N. Price

Ridge-flank hydrothermal circulation is a critical crustal process that affects the Earth's global heat budget, geochemical signature of the Earth's oceans, and supports a vast and diverse subsurface biosphere. These hydrothermal systems are globally pervasive, found in ocean crust of varying ages, spreading rates, and depths. In addition to the broad spatial and structural occurrence, ridge-flank hydrothermal systems operate on a wide range of temperatures, some barely above the temperature of bottom sea water and others near boiling. This dissertation focuses on North Pond, an important end-member, ridge-flank, cool hydrothermal system located on slow-spreading crust in the North Atlantic Ocean. Here I present three original studies that elucidate hydrogeologic and thermal characteristics of North Pond. In chapter 1, I present the first coupled three-dimensional simulations of fluid and heat below North Pond revising many long-standing hypotheses in this system. In chapter 2, I extend three-dimensional simulations to incorporate anisotropic permeability representing important crustal processes and provide a more holistic approach to characterizing the hydrogeologic and thermal regimes of North Pond. Finally, in chapter 3, I develop a

workflow for constructing geologically realistic simulation domains and provide insights and rationale about important considerations during this process. The combination of these studies sheds light on the hydrogeological and thermal regime of this non-discharge dominated, end-member system and provides insights into the drivers of hydrological and thermal processes that are important across the spectrum of ridge-flank hydrothermal systems.

Dedication

In dedication to my person and wife Danielle,

\---

and to my mother Shannon, without whom this would have not been possible.

Acknowledgments

The saying “It takes a village..” rings true for many situations but not for a Ph.D. For a Ph.D. it takes a small city worth of people to inspire, guide, laugh and cry with on the way to this degree. For me there are so many people to name and would undoubtedly make up the longest chapter in this document.

I first want to thank my wife Danielle Price who has constantly inspired me to be a great person as well as a great scientist. She is what a true doctor looks like. Additionally, I want to thank my parents Shannon and David Price as well as my brothers John, Elijah, and Matthew Price and my sister Sarah Johnston and my Uncle Jeff Rivas.

I want to thank my academic advisor Andy Fisher for his patience, dedication to science, and endeavor to persevere! I would also like to thank my committee member Phil Stauffer whose guidance directly contributed to the success of my Ph.D. and Francis Nimmo whose conversations and instruction have widened my view and sparked interest in many aspects of science.

I would like to thank my colleagues and those who have taken mentorship roles. A huge thanks to Margaret Zimmer who has been a valuable mentor, colleague, and friend and working with her has changed the trajectory of my scientific career. Great colleagues and friends alike: Gavin Piccione, Jenny Pensky, Cary Lindsey, Kristin Dickerson, Nate Jones, John Hammond, Amanda Donaldson, Emilio Grande, Victor Bautista, Keir Becker, Emily Kam, Brock and Heather Goodstorm, and so many others.

Thank you all so much for your support through this process and in the future! I owe you all!

Chapter 1: Numerical Simulation of Cool Hydrothermal Processes in the Upper Volcanic Crust Beneath a Marine Sediment Pond: North Pond, North Atlantic Ocean

Reprinted from:

Price, A.N., Fisher, A.T., Stauffer, P.H., Gable, C.W., 2022 “Numerical Simulation of Cool Hydrothermal Processes in the Upper Volcanic Crust Beneath a Marine Sediment Pond: North Pond, North Atlantic Ocean,” Journal of Geophysical Research: Solid Earth 127.1, e2021JB023158 DOI: 10.1029/2021JB023158

JGR Solid Earth

RESEARCH ARTICLE
10.1029/2021JB023158

Numerical Simulation of Cool Hydrothermal Processes in the Upper Volcanic Crust Beneath a Marine Sediment Pond: North Pond, North Atlantic Ocean

A. N. Price[1], **A. T. Fisher**[1], **P. H. Stauffer**[2], **and C. W. Gable**[2]

[1]Earth and Planetary Sciences Department, University of California, Santa Cruz, CA, USA, [2]Computational Earth Science, Earth and Environmental Sciences Division, Los Alamos National Laboratory, Los Alamos, NM, USA

Key Points:

- Patterns of fluid flow in the ocean crust beneath North Pond are complex and time varying, rather than single pass and unidirectional
- Matching key surface and subsurface observations requires simulations with high aquifer permeability, $k_{aq} = 10^{-10}$–10^{-9} m^2
- North Pond hydrogeology differs considerably from isolated basement outcrops due to extensive seafloor connectivity to the overlying ocean

Supporting Information:

Supporting Information may be found in the online version of this article.

Correspondence to:

A. N. Price,
adnprice@ucsc.edu

Citation:

Price, A. N., Fisher, A. T., Stauffer, P. H., & Gable, C. W. (2022). Numerical simulation of cool hydrothermal processes in the upper volcanic crust beneath a marine sediment pond: North Pond, North Atlantic Ocean. *Journal of Geophysical Research: Solid Earth*, *127*, e2021JB023158. https://doi.org/10.1029/2021JB023158

Received 1 SEP 2021
Accepted 21 DEC 2021

Author Contributions:

Conceptualization: A. N. Price, A. T. Fisher, P. H. Stauffer, C. W. Gable
Data curation: A. N. Price
Formal analysis: A. N. Price
Funding acquisition: A. T. Fisher
Investigation: A. N. Price
Methodology: A. N. Price, A. T. Fisher, P. H. Stauffer, C. W. Gable
Software: P. H. Stauffer, C. W. Gable
Supervision: A. T. Fisher
Visualization: A. N. Price
Writing – original draft: A. N. Price, A. T. Fisher
Writing – review & editing: A. N. Price, A. T. Fisher, P. H. Stauffer, C. W. Gable

© 2021. American Geophysical Union. All Rights Reserved.

Abstract

Low temperature hydrothermal systems hosted in the volcanic oceanic crust are responsible for ∼20% of Earth's global heat loss. Marine sediment ponds comprise an important type setting on young ridge flanks where hydrothermal circulation advectively extracts lithospheric heat, but the nature of coupled fluid-heat transport in these settings remains poorly understood. Here we present coupled (fluid-heat) numerical simulations of ocean crustal hydrogeology in and below North Pond, a sediment pond on ∼8 Ma seafloor of the North Atlantic Ocean. Two- and three-dimensional simulations show that advective transport beneath North Pond is complex and time varying, with multiple spatial and temporal scales, consistent with seafloor and borehole observations. A unidirectional, single-pass flow system is neither favored nor needed to match the spatial distribution of seafloor heat flux through North Pond sediments. When the permeability of the crustal aquifer is relatively high (10^{-10}–10^{-9} m^2), simulations can replicate much of the observed variability and suppression of seafloor heat flux and can explain basement overpressures and transient perturbations in pressure and temperature in the upper volcanic crust. Simulation results can also help explain heterogeneity in pore fluid chemistry and microbiology in the crust. Although driven by the same physical processes, the dynamics of hydrothermal circulation below North Pond are different from those seen on "discharge-dominated" ridge flanks, where the permeability and exposed area of isolated basement outcrops control the extent of regional heat extraction.

Plain Language Summary

Cool hydrothermal systems (<20°C) are responsible for a significant portion of Earth's total heat loss. Marine sediment ponds that form in topographic lows surrounded by bathymetric highs are common features, but associated flows of water and heat are not well understood. Here we focus on North Pond, a marine sediment pond on young seafloor west of the Mid-Atlantic Ridge. Measurements of heat flux through North Pond sediments tend to be below that expected for volcanic crust of this age. These observations have been interpreted as unidirectional transport of hydrothermal fluid beneath North Pond, from one side to the other. We created numerical models of fluid and heat in two and three dimensions to test this hypothesis. Our simulations show that the physical properties needed to replicate key observations are consistent with the upper end of values inferred from other studies. Simulated fluid flow paths in the crust below North Pond are complex and vary with time, with no clear preference for flow from one side to the other. Inflow and outflow of fluid around North Pond, and irregular flow patterns below sediments, help to explain a variety of thermal, geochemical, and microbiological observations here and at other locales.

1. Introduction

1.1. Ridge-Flank Hydrothermal Circulation

A quarter of Earth's heat loss occurs by advective extraction of seafloor hydrothermal fluids (∼4–7 TW), mostly at moderate to low temperatures on the flanks of seafloor spreading centers (Hasterok, 2013b; Johnson & Pruis, 2003; Parsons & Sclater, 1977; Stein & Stein, 1994). Low-temperature hydrothermal circulation cycles a volume equivalent to Earth's ocean in and out of the seafloor every 100 k–500 kyr, equivalent to the global flow of rivers and streams (Elderfield & Schultz, 1996; Kadko et al., 1995). This circulation results in a conductive heat-flux deficit on ridge flanks younger than ∼65 Ma (Hasterok, 2013a; Stein & Stein, 1994). Ridge-flank hydrothermal flows impact the physical and chemical state of the lithosphere, influence seismic and tectonic processes at subduction zones, and help to sustain a vast, subseafloor biosphere (Alt, 2004; Orcutt et al., 2015; Peacock & Wang, 1999).

Ridge-flank hydrothermal systems operate across a range of flow rates, fluid reaction and discharge temperatures, and regional settings. In general, higher temperature ridge-flank systems occur as a result of lower fluid flow rates, deeper circulation, and/or longer flow paths within the volcanic crust, but numerous factors influence crustal hydrogeology (Edwards, Becker, & Colwell, 2012; Fisher & Wheat, 2010). For example, sluggish outcrop-to-outcrop hydrothermal circulation on 3.5–3.6 M.y. old seafloor on the eastern flank of the Juan de Fuca Ridge (JFR) results in anoxic basement fluids and crustal reaction temperatures near 65°C (Davis et al., 1992; Hutnak et al., 2006; Mottl et al., 1998; Wheat & Mottl, 2000). In this area, isolated basement outcrops separated by tens of kilometers limit fluid inflow and outflow to and from the volcanic ocean crust, and unusually thick sediments result in relatively high reaction temperatures (Davis et al., 1992; Elderfield et al., 1999; Fisher, 2003; Underwood et al., 2005). In contrast, faster and cooler circulation (10°C–20°C) of more oxic and less reacted basement fluids occurs on younger JFR flank seafloor to the west, where sediments are thinner and basement outcrops are more common and closely spaced (Elderfield et al., 1999; Hutnak et al., 2006; Stein & Fisher, 2003; Wheat et al., 2004).

Low temperatures associated with rapid ridge-flank hydrothermal circulation of oxic basement fluids also occur around Dorado outcrop on ∼23 M.y. old seafloor on the eastern flank of the East Pacific Rise (EPR) (Hutnak et al., 2008; Lauer et al., 2018; Wheat & Fisher, 2008; Wheat et al., 2017). The geometry of fluid circulation in this region is similar to that on the warmer JFR flank site, with isolated basement outcrops separated by tens of kilometers. Cooler circulation around Dorado outcrop may be facilitated by anomalously high basement permeability, resulting in rapid fluid transport and unusually efficient advective heat extraction (Hutnak et al., 2008; Lauer et al., 2018).

We present the first coupled numerical simulations of hydrothermal circulation below and around North Pond, a sediment-filled depression on ∼8 M.y. old seafloor on the western flank of the Mid-Atlantic Ridge (Figure 1, Hussong et al., 1979; Schmidt-Schierhorn et al., 2012). North Pond is surrounded by large areas of exposed upper volcanic crust basalt, in contrast to other ridge-flank sites for which earlier studies have developed simulations of coupled flows. Numerous observations indicate that the upper crust below North Pond is hydrogeologically active, but the nature of this fluid circulation is poorly understood. North Pond's setting is typical of many young ridge flanks, where bathymetric relief and modest sedimentation rates result in patchy or absent sediment cover; thus, simulations of this area have implications for large regions of the seafloor, where volcanic rock exposure is the rule rather than the exception. New simulations elucidate patterns and rates of hydrothermal flows, and the crustal characteristics needed for these flows to occur, where there is little restriction to fluid entering and leaving the volcanic crust on ridge flanks. In the following sections, we summarize key observations that motivate these simulations and, in several cases, provide valuable modeling constraints.

1.2. Setting and Thermal State of North Pond

Abyssal hills around North Pond have wavelengths of 5–15 km and heights of 200–1,500 m, with a crustal fabric that strikes ∼N10–20E, subparallel to the Mid-Atlantic Ridge, and volcanic edifices associated with ridge-segment ends and offsets (Figures 1 and Figure S1 in Supporting Information S1, Hussong et al., 1979; Ryan et al., 2009; Villinger et al., 2019). North Pond is located below a subtropical gyre, where pelagic sedimentation is slow, resulting in thin or no sediment cover over the volcanic upper crust across a wide region (Figure 1). The sediment-covered area of North Pond is ∼100 km^2, with the long axis oriented subparallel to the crustal fabric, and maximum sediment thickness ≤200 m (Langseth et al., 1992; Schmidt-Schierhorn et al., 2012).

Initial heat-flux measurements in North Pond sediments yielded values well below lithospheric predictions, consistent with advective extraction of a large fraction of crustal heat (Langseth et al., 1984). Subsequent and more extensive heat-flux surveys organized along transects, confirmed and extended this observation and revealed additional complexity in heat-flux patterns (Langseth et al., 1992; Schmidt-Schierhorn et al., 2012). Heat-flux values are generally highest in small clusters along the northwestern and northeastern sides of the basin, immediately adjacent to areas of basement exposure, and are highly variable on scales of 10–100s of meters (Figure 1). For this study, we filtered out heat-flux values immediately adjacent to mid-sediment pond outcrops in order to focus on values that are more representative of the dominant heat transfer mechanisms below North Pond (Figure 1b, Supporting Information S1). Within North Pond, 90% of seafloor heat-flux values are below lithospheric (170–190 mW/m^2, based on crustal age), with a majority (55%) of values ranging from 20 to 100 mW/m^2, ∼10–

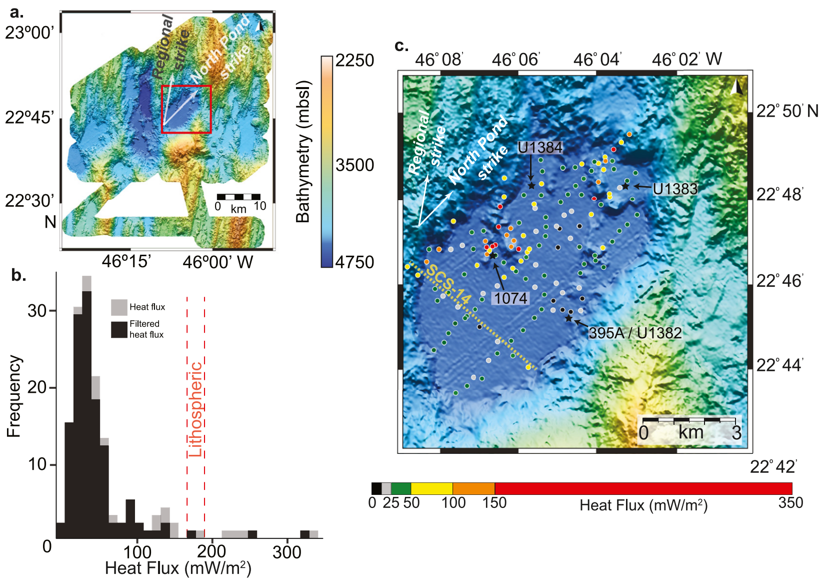

Figure 1. Setting and heat flux values at North Pond, on the western flank of the Mid-Atlantic Ridge. (a) Regional swath map showing bathymetry of North Pond and surrounding area. Red box shows area of panel (c), and white arrows distinguish regional strike direction versus North Pond long-axis strike direction. (b) Histogram of North Pond heat flux data (gray = all data, black = filtered to remove values above buried basement highs, discussed in text). Red dashed lines indicate the range of calculated lithospheric heat flux as function of crustal age. (c) Bathymetry on and around North Pond, with all seafloor heat-flux values colored by magnitude, stars marking locations of boreholes, yellow dashed line corresponds to seismic transect SCS-14 used for two-dimensional simulation domain, and white arrows distinguish regional strike direction versus North Pond long-axis strike direction. Bathymetric data from Schmidt-Schierhorn et al. (2012), heat flux data from Langseth et al. (1992) and Schmidt-Schierhorn et al. (2012).

55% of lithospheric (Figure 1). A recent remotely operated vehicle survey found evidence for distributed upward seepage of cool hydrothermal fluids from the crust adjacent to northern pond margins (Villinger et al., 2019).

1.3. Scientific Drilling and Borehole Measurements in North Pond

North Pond was first investigated during Deep Sea Drilling Project (DSDP) Leg 45, as typical young seafloor formed at a slow spreading rate (Melson et al., 1979). DSDP Hole 395A was drilled near the southeastern margin of North Pond (Figure 1), penetrating ~90 m of sediment and nearly 600 m of basaltic basement. Hole 395A was revisited multiple times for geophysical logging, which revealed cool and nearly isothermal conditions in the upper ~300 m of basement, indicative of rapid downflow of fluid, and crustal layering at scales of 10–100 m (Bartetzko et al., 2001; Becker et al., 1984; Gable et al., 1992; Mathews et al., 1984; Moos, 1990). Fluid flow down crustal boreholes does not require a natural "under-pressure" ($\Delta P < 0$), as the imposition of a cold, dense column of seawater in a borehole in warmer crust can create runaway downflow (Becker et al., 1983; Fisher et al., 1997; Winslow et al., 2013). Hole 395A was eventually sealed, more than 20 years after drilling, with a long-term borehole observatory (CORK), intended to prohibit rapid downflow of fluid and allow thermal and pressure recovery of the crustal aquifer (Becker et al., 1984, 2001; Morin et al., 1992).

Recent expeditions focusing on geochemical and microbiological investigations of North Pond drilled additional holes and installed CORK observatories. Integrated Ocean Drilling Program (IODP) Expedition 336 and related expeditions included CORK operations in Holes 395A, nearby Hole U1382A, and two holes at Site U1383 located ~6 km to the north, where the sediment thickness is 40–50 m (Figure 1, Becker et al., 2018; Expedition

336 Scientists, 2012; Wheat et al., 2012). Long-term pressure records from the CORK in Hole 395A indicate a few kPa of overpressure (Becker et al., 2018). Pressure data from newer CORKs show modest overpressures of $\Delta P \sim 11$ kPa in the upper 100 m of basement in Hole U1382A, and $\Delta P \sim 2$–13 kPa in the upper 170 m of basement in Hole U1383C. In U1383C, measurements in distinct crustal intervals indicate higher overpressures with greater depth. Measurements in the upper ∼50 m of basement in Hole U1383B (∼25 m from Hole U1383C) suggest a small under-pressure (Wheat et al., 2020), consistent with *in-situ* pore pressure measurements in North Pond sediments indicating modest underpressures in shallow basement (Langseth et al., 1992). Pressure differences in CORKs were noted to vary irregularly on multi-annual timescales, as do long-term temperature records. A cross-hole tracer experiment at Site U1383 is consistent with rapid transport and distinct flow paths in the shallow volcanic crust (Wheat et al., 2020).

1.4. Chemistry and Microbiology of North Pond

Alteration products in the upper volcanic crust below North Pond indicate water/rock reactions at $T \leq 15°C$ (Lawrence & Drever, 1981; Lawrence & Gieskes, 1981; Lawrence et al., 1978). Conditions in North Pond sediments are dominantly diffusive and reactive (McDuff, 1984; Orcutt et al., 2013; Ziebis et al., 2012). There is evidence for slow downward seepage through North Pond sediments (≤0.5 cm/yr; McDuff, 1984) consistent with later pore-pressure measurements and laboratory permeability tests of North Pond sediments (Langseth et al., 1992). Sedimentary pore fluids show oxygen concentrations that decrease with depth initially, then increase when approaching the sediment-basement interface, with upper basement fluids that have major ion concentrations similar to bottom seawater, but are depleted in oxygen and Sr (Orcutt et al., 2013). Similar patterns have been noted on multiple ridge-flanks where cool, relatively unaltered bottom water recharges the volcanic crust and flows rapidly below marine sediments (e.g., Baker et al., 1991; Elderfield et al., 1999; Versteegh et al., 2021). Diffusive limitations in the penetration of oxygen into North Pond sediments, despite having oxygen-rich water at both upper and lower boundaries, helps to explain the presence of an active nitrogen cycling microbial community (Reese et al., 2018; Wankel et al., 2015).

Microbes in the volcanic crust below North Pond are distinct compared to those in the overlying water column, with some taxa adapted to the cycling of nitrogen and iron (Meyer et al., 2016; Tully et al., 2018; Zhang et al., 2016). The colonization of crustal microbes in sealed boreholes in North Pond depends more on variations in crustal fluid composition (a function of fluid flow paths and histories) than it does on the nature of mineral substrate (Orcutt et al., 2021). Metagenomic analyses of time-series samples from sealed boreholes at North Pond suggest that microbial populations are dynamic on multi-annual timescales (Seyler et al., 2021; Tully et al., 2018). Carbon availability below North Pond sediments appears to help regulate microbial populations, adapted for both autotrophic and heterotrophic metabolisms, consistent with the presence and utilization of distinct carbon pools in the crust (Seyler et al., 2021; Shah Walter et al., 2018; Trembath-Reichert et al., 2021).

1.5. A Conceptual Model for Rapid Lateral Flow in the Crust Below North Pond

Geological, geophysical, geochemical and microbiological observations from North Pond have been organized and interpreted using an idealized conceptual model in which cold and unaltered ocean bottom water flows downward into the volcanic crust surrounding the sediments, moves laterally under the pond, then rises upwards on the opposite side of pond and discharges at the seafloor (Langseth et al., 1984). This idealized model provides a useful conceptual framework, but it neglects key observations that indicate significant complexity and dynamics in flow patterns and processes. In the present study, we apply numerical simulations of coupled fluid flow and heat transport below North Pond to answer these questions:

1. Is rapid fluid flow in the volcanic crust below North Pond dominated by a stable, single-pass, lateral-transport geometry?
2. What crustal properties are most consistent with the partitioning of advective and conductive heat transport through and around North Pond?
3. How does crustal hydrogeology below North Pond compare to that within other ridge flanks where similar processes are thought to occur?

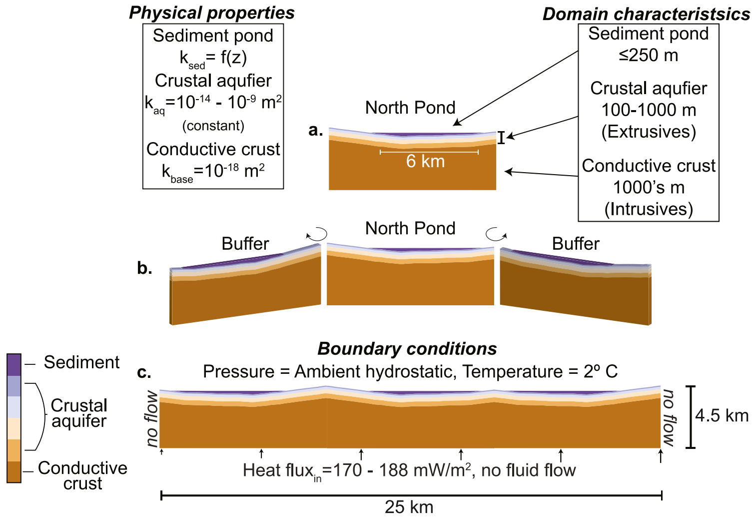

Figure 2. Two-dimensional simulation domain showing geological layers, boundary conditions, and associated physical properties. (a) Simulation domain of interest representing North Pond with associated physical properties and characteristics. (b) Simulation domain of interest with two (2) mirrored "buffer regions" rotated and appended to main area of interest. (c) Complete North Pond domain with scale and associated boundary conditions.

2. Simulation Methods

2.1. Numerical Model

We simulated coupled fluid and heat transport in the volcanic ocean crust below North Pond with the numerical code, Finite Element Heat and Mass (FEHM), which uses a node-centered, finite-volume representation of storage and transport in porous media (Zyvoloski et al., 2015). FEHM uses a fully implicit solver with variable upstream-downstream weighting to solve conservation of mass and enthalpy including gravitational potential energy which is necessary for deep subseafloor systems (Stauffer et al., 2014). Simulation domains were developed as Delaunay meshes of triangular (two-dimensional) and tetrahedral (three-dimensional) cells using the Los Alamos Grid Toolbox (Los Alamos Grid Toolbox, LaGriT, 2019).

2.1.1. Simulation Domains

Simulations were completed in two and three dimensions, with geometry guided by bathymetric and seismic reflection data (Schmidt-Schierhorn et al., 2012; Villinger et al., 2018). Simulation grids were defined in a cartesian coordinate system; for purposes of simulation and to ease the discussion that follows, we conceptualize and describe North Pond as having a long axis oriented "north to south," and a short axis oriented "west to east." In reality, the regional structural trend and directions of North Pond's long and short axes are rotated 10–20° east and are slightly offset relative to each other (Figure 1, Figure S1 in Supporting Information S1).

Domains were built as stacked sequences of sediment and volcanic rock layers. North Pond sediments were made thickest in the southwest section of the pond and pinch out as sediments drape over the sloping contacts on the sides of North Pond, whereas volcanic crustal layers were assigned consistent vertical thicknesses below the top of basement, tied to geophysical observations (Figures 2 and 3). We tested aquifer layers in the uppermost volcanic crust with thicknesses of 100, 300, 600, and 1,000 m, based on stratigraphy inferred from scientific drilling boreholes, cores, and geophysical logs (Bartetzko et al., 2001; Mathews et al., 1984; Moos, 1990). We incorporated a 3–4-km-thick conductive boundary layer below the crustal aquifer to allow warping of isotherms in the deeper crust that can form because of advective heat transport in the shallower crust. We applied spatially

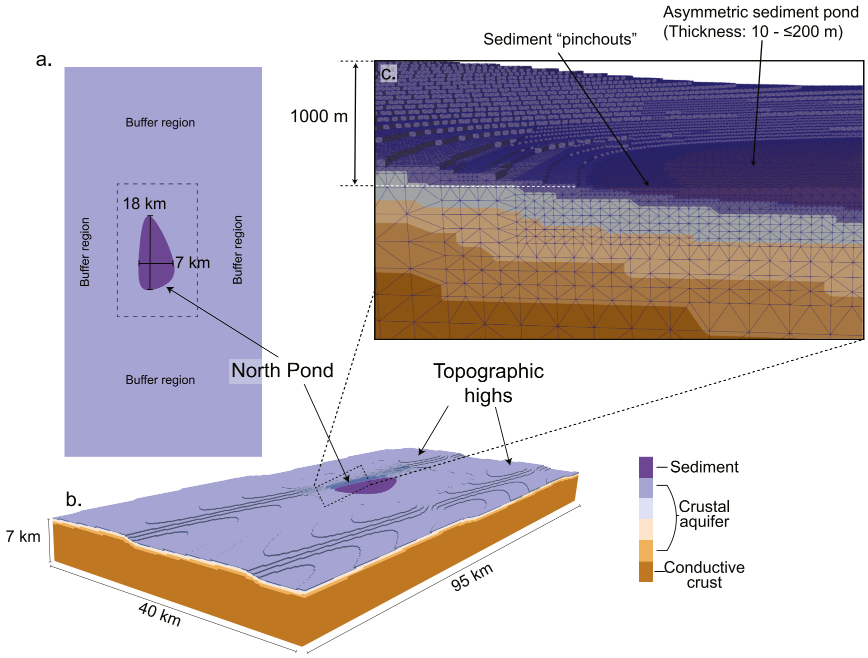

Figure 3. Three-dimensional simulation grid (a) Map view of simulation grid with geometry of sedimented pond displaying asymmetry along and across strike. Buffer regions containing additional ponds were added to minimize the influence of domain side boundaries on processes in and below North Pond. (b) Entire simulation grid with geometry and sediment pond representing North Pond and surrounding topographic highs. (c) Cross-section of a fraction of the simulation domain showing variable node spacing (2 × vertical exaggeration).

varying heat flux at the base of the domain as a function of crustal age (Supporting Information S1), with a mean heat input of ~180 mW/m^2.

In all simulations, we placed North Pond in the center of a larger domain surrounded by "buffer regions" to minimize the influence of lateral boundaries on fluid and heat flow patterns through and near North Pond. Side and bottom domain boundaries allowed no fluid flow, no heat transport was allowed through the side boundaries, and the top boundary was assigned constant temperature, pressure as a function of water depth, and free flow for fluid and heat. Grid resolution varied spatially, with the smallest node spacing below and around North Pond, particularly near sedimentary pinchouts at the pond edges. Larger grid spacing was used with greater depth and greater lateral distance from North Pond.

2.1.2. Two-Dimensional Simulation Domains

Two-dimensional simulation domains were designed using geometric constraints from seismic reflection line 14 (SCS14) (Figure S2 in Supporting Information S1, Schmidt-Schierhorn et al., 2012). SCS14 is oriented along the short axis of North Pond, clearly defines the geometry of basement relief and sedimentary layering and is collocated with a transect of heat-flux measurements. With North Pond sediments and the surrounding basement highs defined to the limit of seismic data, we buffered the simulation domain by inserting "mirror-images" of North Pond geometry on either side of the selected profile (Figure 2), to reduce the influence of no-flow boundaries on patterns of circulation below and near North Pond.

The upper volcanic crust below and adjacent to North Pond was assigned to one of five layers. The upper 1,000 m was divided into four layers having thicknesses of 100, 200, 300, and 400 m (Figure 2), allowing one or more

Table 1
Values of Physical Formation Properties for Two- and Three-Dimensional Simulation Domains

Dimensions	Layer	Permeability (m^2)	Porosity (−)	Thermal conductivity (W/m K)
Two	Sediment [a]	9.6×10^{-16}–2.5×10^{-16}	0.59–0.67	0.99–1.1
	Crustal aquifer	10^{-16}–10^{-9}	0.02–0.1	1.8–2.0
	Conductive crust	10^{-18}	0.01	2.0
Three	Sediment [a]	4.0×10^{-16}	0.62	1.06
	Crustal aquifer	10^{-16}–10^{-9}	0.02–0.1	1.8–2.0
	Conductive crust	10^{-17}	0.01	2.0

[a] Sediment properties varied with depth below seafloor for two-dimensional simulations, and were set to intermediate, constant values for three-dimensional simulations.

of these to be assigned elevated permeability and function as a crustal aquifer. The final two-dimensional grid comprises 3.6×10^4 vertices with vertex spacing ranging from 4 to 200 m.

2.1.3. Three-Dimensional Simulation Domains

Three-dimensional simulation domains represent regional patterns of bathymetric relief and sediment cover, without attempting to replicate details that are poorly resolved in available data. We used bathymetric and seismic data to develop an analytic function that represents the top of the volcanic crust below and around North Pond (Supporting Information S1). This function was extended in both along-strike and across-strike directions, placing the North Pond basin in the center of the domain (Figure 3). We created a buffer region around North Pond that separates this feature from no-flow boundary conditions. A horizontal plain representing the top of sediment was intersected with the basement surface within the North Pond basin, whereas no sediment was placed over basement lows in the surrounding buffer region. The long-axis and short-axis lengths of the sediment pond are 18 and 7 km, respectively, maximum sediment thickness is 200 m, and the deepest part of the sediment pond occurs in the southwestern quadrant. The top of volcanic basement dips asymmetrically below North Pond, most steeply along western and southern margins (∼15% slope), and more gradually along the eastern and northern margins (∼5% slope).

Once again, volcanic rock layers were defined to allow permeability to be varied by depth, and vertex spacing differed with location (finer near and below North Pond) (Figure 3). The final three-dimensional domain has dimensions of 95 km along-strike, 40 km across-strike, 6–7 km vertically, and contains 1.4×10^6 vertices with spacing of 11–1,000 m (Figure 3).

2.2. Domain Properties

2.2.1. Porosity and Thermal Conductivity

Simulated sediment porosity and thermal conductivity were assigned based on core data from North Pond Sites U1382-84 (Edwards, Bach, & Klaus et al., 2012). Depth varying sediment properties were assigned to two-dimensional domains, whereas constant sediment properties appropriate for North Pond were applied for three-dimensional domains (Table 1). Basement rocks were assigned bulk properties (porosity, thermal conductivity) based on data from North Pond and other drilled locations (e.g., Bartetzko & Fisher, 2008; Becker et al., 2001, 1983; Shipboard Scientific Party, 1997). Properties varied with depth depending on whether or not individual layers were intended to be part of a crustal aquifer. We assigned porosity of 10% to the most permeable, upper crustal (aquifer) layers, lower porosity to deeper (but still permeable) layers, and 1% to the conductive boundary region at depth. Associated thermal conductivity values were determined as a geometric mean of massive basalt and seawater, ranging from 2.0 W/m-K for the lowest porosity to 1.8 W/m-K in the crustal aquifer (Table 1).

2.2.2. Permeability

Simulated sediment permeability (k_{sed}) was linked to porosity for pelagic sediments (Spinelli et al., 2004), resulting in values of $k_{sed} \sim 10^{-16}$–10^{-15} m^2 (Table 1), consistent with laboratory measurements of North Pond core samples (Langseth et al., 1992). Basement permeability in the ocean crust is less well constrained by observations and was treated as a free parameter within a range defined by observations from North Pond boreholes and basaltic ocean crust in general. Borehole tests in Hole 395A suggest bulk permeability at 300–500 m sub-basement (msb) that is 10^{-17}–10^{-14} m^2 (Becker, 1990) and a cross-hole tracer experiment run at Site U1383 indicates permeability up to 10^{-9} m^2 (Wheat et al., 2020). Global observations from packer experiments and borehole thermal data indicate basalt permeability values in the upper 500 msb of 10^{-14}–10^{-10} m^2 (Becker, 1990; Becker & Fisher, 2008; Becker et al., 1994; Fisher et al., 2014; Winslow et al., 2013).

Coupled simulations from two ridge-flank studies provide additional information on physical properties. Three-dimensional simulations of outcrop-to-outcrop flow on the eastern flank of the Juan de Fuca Ridge found that permeabilities of 10^{-13}–10^{-12} m^2 in the upper 300 m of volcanic crust were most consistent in sustaining a hydrothermal siphon with modest throughput (∼10 kg/s) and limited thermal influence on conductive heat flux through the surrounding seafloor (Winslow et al., 2016). Simulations of outcrop-to-outcrop flow on older seafloor of the eastern flank of the EPR, where 60%–90% of lithospheric heat is extracted on a regional basis (Fisher et al., 2003; Hutnak et al., 2008), suggest that crustal aquifer permeability of 10^{-10}–10^{-9} m^2 may be required, and hydrothermal discharge is $\geq 10^3$ kg/s (Lauer et al., 2018). Given all of this information, the permeability of the upper ocean crust below North Pond seems likely to be within a range of 10^{-14}–10^{-9} m^2 in the upper 100–600 m of basement.

2.3. Simulation Initial Conditions and Dynamic Steady State

Initial conditions for two- and three-dimensional, coupled simulations were established by running conductive simulations, which allowed assessment of conductive refraction in distributing seafloor heat flux. Conductive refraction is facilitated by two main processes: (a) bathymetric relief at the seafloor (a constant temperature boundary), and (b) spatial (lateral, depth) variations in thermal conductivity. Conductive refraction results in warping of subsurface isotherms, causing heat-flux variations, even in the absence of fluid flow (Blackwell et al., 1980; Lachenbruch, 1968; Lee, 1991).

Beginning with a conductive thermal structure, initial coupled simulations were run with low permeability in crustal aquifer layers (10^{-17} m^2) to calculate ambient hydrostatic pressure values consistent with dominantly conductive conditions. Simulations with high aquifer permeability were initiated with results of low permeability simulations, once the latter achieved dynamic steady state. Dynamic steady state was achieved in fully coupled simulations after typical simulation times of 3–5 × 10^5 yr, long enough so that thermal conditions below the crustal aquifer have equilibrated with advective heat extraction in overlying layers. For higher permeability values, dynamic steady state occurs when there is no long-term trend in temperatures or pressure values (generally $\Delta T/\Delta t < 0.01$ °C/kyr, $\Delta P/\Delta t < 0.1$ kPa/kyr), independent of oscillations within the crustal aquifer.

3. Simulation Results

3.1. Simulation Constraints and Metrics

Successful fluid-heat flow simulations of North Pond should replicate key observations, including:

1. Suppression of average values and local variability in seafloor heat flux (Figure 1), including measurements of elevated and suppressed heat flux through sediment adjacent to pond margins (Langseth et al., 1992; Schmidt-Schierhorn et al., 2012).
2. Conductive and diffusive/reactive conditions in North Pond sediments, indicating slow or no significant fluid flow, and rapid fluid circulation in volcanic crust leading to cool conditions (McDuff, 1984; Orcutt et al., 2013; Ziebis et al., 2012).
3. Modest underpressures and overpressures (≤10s of kPa) in the upper volcanic crust below North Pond sediments, including higher overpressures with depth (Becker et al., 2018; Langseth et al., 1992; Wheat et al., 2020).
4. Time-varying fluid pressures and formation temperatures in the volcanic crust, with changes occurring on multiannual timescales (Becker et al., 2018).

In addition to these qualitative and quantitative constraints, we used several metrics to assess the nature of hydrothermal processes, including rates and patterns of fluid transport in the volcanic crust.

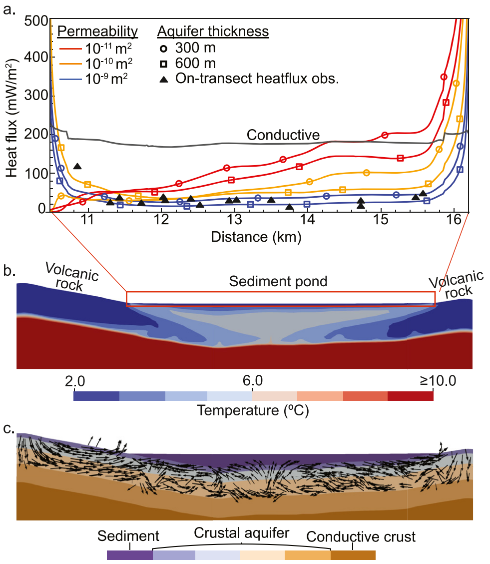

Figure 4. Two-dimensional simulation output of heat flux data and corresponding temperature and velocity fields. (a) Plot of two-dimensional simulation results showing heat flux values in mW/m^2 as a function of distance in km across-strike in the sedimented pond for different simulated aquifer permeabilities and thickness. Solid triangles are along-transect heat flux measurements seen in Figure 1c. Error bars for these measurements are smaller than the size of the symbol. Permeabilities of $k_{aq} = 10^{-11}$–10^{-9} m^2 are represented by different colors and aquifer thickness of 300 and 600 m are delineated by open circles and squares, respectively. (b) Simulation output for $k_{aq} = 10^{-9}$ m^2 with temperature field in °C, red box denotes position of heat flux values in Figure 2a. Isotherms show "pooling" of heat beneath the sediments of North Pond and convection occurring near the aquifer/conductive basement contact. (c) Vector representation of fluid flow in the volcanic aquifer overlain on the aquifer and sediment units beneath North Pond.

3.2. Conductive and Coupled North Pond Simulations in Two Dimensions

A simulated, conductive heat flux profile across North Pond has small positive anomalies (5–10 mW/m^2) near sediment pinchouts at pond edges and slightly suppressed values near the pond center (Figure 4). This pattern is a consequence of thermal refraction, with some heat flow bypassing the low-conductivity sediment pond, and locally elevated values near the break in slope near the pond margins. Coupled simulations with low aquifer permeability result in conductive conditions; once aquifer permeability $k_{\text{aq}} \geq 10^{-12}$ m^2, small-scale convection begins to redistribute heat locally, and a heat flow deficit develops for $k_{\text{aq}} \geq 10^{-11}$ m^2 (Figure 4). The onset of thermally significant convection in the crustal aquifer is broadly consistent with Rayleigh number calculations (Figure S4 in Supporting Information S1), but importantly, sloping and irregular aquifer boundaries help drive convection even for subcritical Rayleigh numbers (Criss & Hofmeister, 1991).

For two-dimensional simulations of North Pond, aquifer permeability of $k_{\text{aq}} = 10^{-11}$ m^2, and thickness of 300–600 m, results in seafloor heat flux depressed by 60%–70% (relative to lithospheric) on one side of the aquifer, and heat-flux elevation on the opposite side (Figure 4). For $k_{\text{aq}} = 10^{-10}$–10^{-9} m^2, there is more consistent heat-flux suppression across North Pond, with a larger fraction of advective transport. In these simulations, cool fluids enter the crustal aquifer from both sides of the pond, recharging to the aquifer base as they flow laterally. Fluids are warmed by lithospheric heating, forming an unstable, buoyant plume below and around the pond center, where sediment is thickest. Fluids rise in this plume to the base of the sediment, then spread laterally toward the pond edges and exit at the seafloor surrounding the sedimented pond. Sediments in North Pond limit vertical heat transport through this insulating lid, so the efficiency of advective heat extraction is controlled by mixing and lateral flow in the underlying aquifer. Simulated fluid convection in basement becomes increasingly unstable at high permeability values, with larger and smaller cells forming near the center of North Pond and migrating toward both sides before collapsing and reforming (Figure 4, Movie S1). Median values of fluid specific discharge in the crustal aquifer are 7.5 m/yr and 6.7 m/yr for $k_{\text{aq}} = 10^{-9}$ m^2 and aquifer thickness of 300 and 600 m, respectively (Table S2).

The asymmetric pattern of seafloor heat flux across North Pond in simulations with $k_{\text{aq}} = 10^{-11}$–10^{-9} m^2 is broadly consistent with the pattern associated with the idealized conceptual model (Langseth et al., 1984), except that the eastern side of the transect has higher heat flux than the western side. But, rather than resulting from a single-pass, unidirectional fluid flow pattern, this asymmetry in simulated heat flux is caused by differences in fluid flow rates in the crustal aquifer on either side of the pond. Simulated convection is more vigorous on the western side of North Pond, where the aquifer base is more steeply sloped, and slower to the east. For $k_{\text{aq}} = 10^{-9}$ m^2, for both 300 and 600 m aquifers, heat flux is suppressed consistently across North Pond to values that are 10%–20% of lithospheric, matching observations along seismic profile SCS-14 (Figure 4). Lithospheric heat-flux input into the base of the domain is slightly higher on the eastern side of North Pond simulations, based on crustal age, but this difference is too small (<1%) to have a measurable influence on fluid flow and seafloor heat-flux patterns, given sediment pond geometry.

3.3. Conductive and Coupled North Pond Simulations in Three Dimensions

Conductive simulations of the three-dimensional domain result in heat-flux output through North Pond that is reduced by up to 50% relative to lithospheric input, as a consequence of thermal refraction (Figure 5, Figure S3 in Supporting Information S1). This is a greater impact from refraction than seen for two-dimensional, conductive simulations (Figure 4) because there is a proportionately larger region of bare and bathymetrically elevated

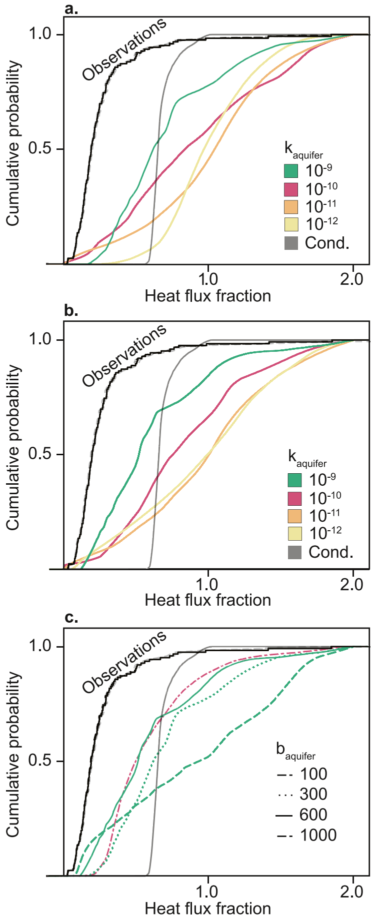

Figure 5. Empirical cumulative distribution function of heat flux fraction (heat flux into domain/heat flux out through sediments) for (a) aquifer thickness 300 m and k_{aq} = 10^{-12}–10^{9} m^2 (b) aquifer thickness 600 m and k_{aq} = 10^{-12}–10^{9} m^2 (c) maximum permeabilities (k_{aq} = 10^{-10} m^2 for 1000m thick, k_{aq} = 10^{-9} m^2 for all others) simulated across the range of aquifer thickness: 100–1,000 m. All plots have filtered heat flux observations from North Pond shown with a solid black line, range of observations in dashed gray lines, and initial conductive simulation in solid gray line.

crustal rocks in three dimensions compared to two. This allows a greater opportunity for warping of isotherms at depth below North Pond to increase the fraction of lateral conductive heat transport that bypasses sediments.

As with two-dimensional domains, three-dimensional coupled simulations with moderate aquifer permeabilities ($k_{aq} \leq 10^{-13}$ m^2) result in slow convection in basement rocks below and around North Pond, at rates too slow to measurably influence conductive heat transport. In contrast, when permeability is k_{aq} = 10^{-12}–10^{-11} m^2, for aquifer thickness b = 300–600 m, the median heat flux through North Pond is about the same as input at the base of the domain, and considerably higher than seen for the conductive case (Figure 5). This behavior results from an increase in the local efficiency of lateral heat transport once convection in the aquifer becomes sufficiently rapid due to higher aquifer permeability. Under these conditions convection in the aquifer homogenizes fluid temperature below North Pond, moving heat laterally so that it can bypass the insulating lid formed by sediments. As a consequence, there is more heat drawn toward the crust below North Pond and, at moderate k_{aq}, North Pond sediments shift from being a barrier to heat extraction to functioning like a heat sink on a regional basis.

At k_{aq} = 10^{-10}–10^{-9} m^2, convection in the crustal aquifer becomes increasingly vigorous and median heat output falls below both lithospheric input and conductive output (Figure 5). A thicker crustal aquifer (b = 300–1,000 m) extracts more heat than a thinner aquifer (b = 100 m) (Figure 5) because the size of convection cells and the vigor of lateral heat transport scales with aquifer thickness. Furthermore, a smaller number of large cells that extend deeper is more efficient for drawing heat from depth, moving heat laterally to the pond edges, and entraining cold recharge. At the highest permeabilities tested for this study (k_{aq} = 10^{-10}–10^{-9} m^2) advective extraction comprises 30%–35% of lithospheric heat removed from below North Pond.

For k_{aq} = 10^{-9} m^2, pressures in the basement aquifer below North Pond are generally consistent with CORK observations (Becker et al., 2018; Wheat et al., 2020), deviating from hydrostatic by 10s of kPa in the upper 0–200 m below the sediment-basement interface (Figure 6).

Observations of greater overpressures with depth in these simulations are consistent with measurements made where there is a rising plume of buoyant fluid. Simulations include multiple scales of transient convection in the crustal aquifer, producing overpressures and underpressures in different locations, varying with time as plumes form, rise, shift position, and collapse. These modest deviations from hydrostatic conditions in shallow basement below North Pond result in very slow seepage through overlying sediments, on the order of 0.1–1 mm/yr (Figure 6, Figure S4 in Supporting Information S1), too slow to influence heat flux, but with potential to advect solutes.

Convection in three-dimensional simulations is unstable at high permeabilities (for all aquifer thicknesses), leading to complex, time-varying patterns of fluid circulation and seafloor heat flux (Figure 7, Movie S2). Convection comprises a mixture of transient plumes and rolls having a range of shapes and dimensions. Plumes form in multiple locations along the base of the aquifer, including a large central plume that forms where the sediment is thickest and the aquifer is deepest (Figure 8, Figure S5 in Supporting Information S1, Movie S2). Water is pulled into the basement aquifer at multiple locations around the edges of North Pond, chilling basement rocks and returning warmer fluid to the seafloor in other locations. As a consequence, there are patches of lower and higher seafloor heat flux through North Pond sediments, some of which remain stable and others that migrate over time, leading to spatial variability at length scales of 10–100s of meters

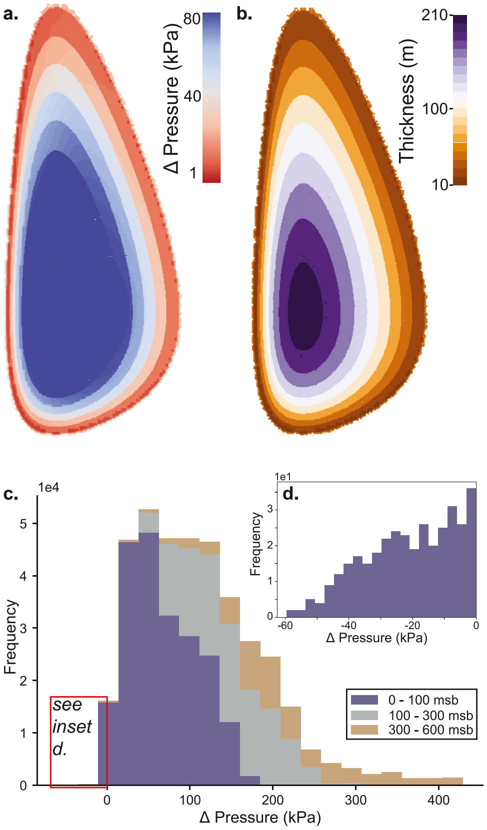

Figure 6. Plots of differential pressures observed in simulation of $k_{\mathrm{aq}} = 10^{-9}$ with thickness 600 m. (a) Map view of differential pressures observed in the aquifer nodes directly below sedimented pond. (b) Map view of sediment thickness (m) between seafloor and aquifer nodes directly below sedimented pond. (c) Stacked histogram of differential pressures calculated in the entire aquifer directly below the sedimented pond described as a range of aquifer thickness 0–100 msb (meters sub-basement) (purple), 100–300 msb (gray), and 300–600 msb (tan). Red box shows the area of detail plotted in panel (d). (d) Histogram of negative differential pressures, simulated only in part of the shallowest 100 msb below North Pond.

(Figure 7, Movie S2), consistent with the distribution of seafloor heat flux (Figure 1).

Small-scale convective rolls in the aquifer result in bands of lower and higher heat flux through North Pond sediments that extend laterally across-strike (Figure 7). In general, the lowest simulated heat-flux values are found close to sediment margins where focused recharge occurs (Figures 7 and 8). Along the western and southern margins of the sediment pond, where the slope of the sediment-basement interface is steepest, patches of higher and lower heat flux tend to be small and located immediately adjacent to sediment pinch-outs. In contrast along the eastern and northern margins, where there is a shallower slope at the aquifer base, patches of simulated higher and lower heat-flux values tend to be wider and extend farther toward the center of the pond.

Mixed convection in the crustal aquifer below North Pond results in temperature oscillations that have multiple amplitudes and periods. The geometries and timescales of associated flow patterns vary with the permeability and thickness of the crustal aquifer. The dominant convective mode, with the largest temperature variations and the longest timescale, is associated with a central plume that entrains recharge at the pond margins and rises below the thickest sediment (Figure 8, Movie S2). Although this is a three-dimensional flow pattern, it is dominated by across-strike transport (along the short axis of the pond), similar to the pattern simulated in two dimensions (compare the plume patterns in Figures 4 and 8) but is not unidirectional. The importance of the across-strike flow direction increases as the permeability of the crustal aquifer increases from $k_{\mathrm{aq}} = 10^{-11}$ m^2–10^{-9} m^2 (Figure S5 and S6 in Supporting Information S1). At the high end of this permeability range, the dominant circulation pattern creates a band of rising, buoyant fluid that runs in the along-strike direction down the long axis of North Pond, where sediment tends to be thickest (Figure 8, Figure S5 in Supporting Information S1**).**

At $k_{\mathrm{aq}} = 10^{-11}$ m^2–10^{-10} m^2, there is a clear pattern of secondary convective rolls superimposed on the larger-scale flow system, with roll axes aligned along the across-strike direction, and a linear plume oriented along-strike. At $k_{\mathrm{aq}} = 10^{-9}$ m^2, basement fluid temperatures become nearly homogenized and the secondary convection pattern is suppressed due to the increased efficiency in advective transport within the crustal aquifer (Figure 8, Movie S2). All simulated convective modes are transient, with plumes and rolls that form, shift back and forth, migrate, breakup, and reform. At the upper limit of permeabilities simulated, $k_{\mathrm{aq}} = 10^{-9}$ m^2, temperatures of small-scale rolls and plumes in a 600 m aquifer vary on periods of ~10^1–10^2 years (Figure S7 in Supporting Information S1).

A comparison of the rates and directions of horizontal flow in the aquifer below North Pond helps to illustrate the shift in dominant flow patterns as a function of aquifer permeability (Figure S6 in Supporting Information S1). When $k_{\mathrm{aq}} = 10^{-11}$ m^2, horizontal flow rates up to 2.5 m/yr tend to be randomly oriented by azimuth. At $k_{\mathrm{aq}} = 10^{-10}$ m^2, the highest horizontal flow rates are 7.5 m/yr and, for a thicker aquifer, across-strike flow becomes more organized. At the highest aquifer permeability tested, $k_{\mathrm{aq}} = 10^{-9}$ m^2, horizontal flow reaches 15 m/yr and is dominantly across-strike, along the short axis of North Pond (Figures S5 and S6 in Supporting Information S1). Thus, simulations indicate a preference for across-strike rather than along-strike fluid transport, but not as part of a single-pass, unidirectional flow system. Instead, the simulations indicate complex, three-dimensional and transient fluid flow, from which the dominance of across-strike transport is an emergent behavior.

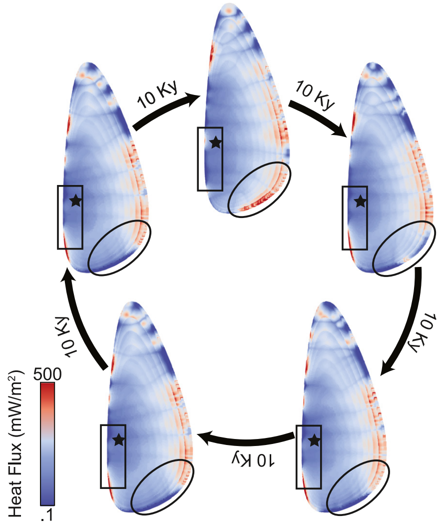

Figure 7. Map view of sediment pond heat flux at permeability $k_{aq} = 10^{-10}$ m^2 and thickness 600 m. Time steps between views are 10,000 years where boxes outline areas where high heat flux values are located directly adjacent to low heat flux values, ovals outline an area of heat flux that exhibits a transient response with high and low heat flux values as a function of time, and stars denote the location of the nodes used in the frequency analysis shown in Figure S7 in Supporting Information S1.

4. Discussion: A Revised Understanding of North Pond Hydrogeology

4.1. Patterns of Fluid and Heat Flow Below North Pond

Heat flux through North Pond is (a) generally suppressed below lithospheric values, (b) higher in clusters of measurements near the western and northern margins, and (c) variable on a spatial scale of 10^1–10^2 m (Figure 1). Rather than being explained by unidirectional, single-pass flow along the short axis of North Pond (across-strike), coupled simulations in two and three dimensions are best able to replicate the observed heat-flux pattern with fluid circulation that is complex and time-varying (Figure 9). Unidirectional, single-pass flow is neither favored or required to explain the broad pattern of heat-flux suppression nor clusters of elevated values near pond margins.

Small scale variability in basement relief was not simulated in the present study but some variations in seafloor heat flux associated with shallow basement relief are likely caused by thin sediments overlying buried basement highs (Davis et al., 1992; Fisher & Harris, 2010; Hutnak et al., 2008). Local basement highs appear to be more common along the western and northern margins of North Pond, where there are clusters of the most extreme heat-flux values (Figure 1) but are difficult to resolve in seismic profiles because of rough and sloping basement surfaces (Figure S2 in Supporting Information S1). While these local bathymetric highs might alter local heat and fluid flux patterns, they are unlikely to alter the overall flow geometry and characteristics of the North Pond system.

The vigorous and dynamic nature of simulated fluid and heat flux in the crustal aquifer below North Pond helps to explain pressure and temperature observations. Simulations with relatively high basement permeability (10^{-11}–10^{-9} m^2) result in pressure differentials, relative to ambient hydrostatic, of 10s of kPa, similar to those observed in sealed crustal boreholes (Figure 6, Becker et al., 2018). An increase in the magnitude of the crustal overpressure with depth into the aquifer is consistent with an upward component of fluid flow, as occurs within and around a rising plume of warm

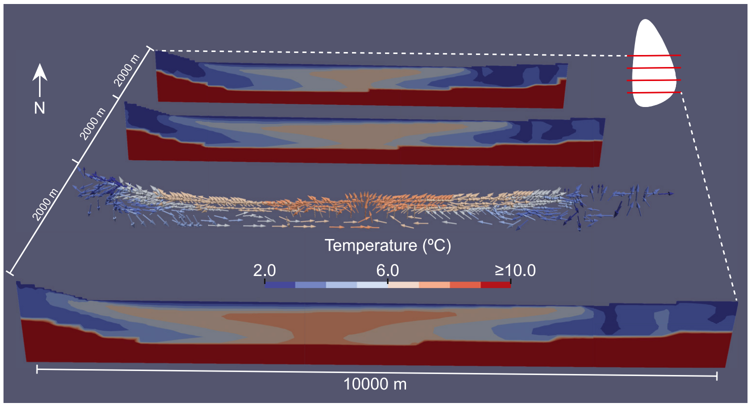

Figure 8. Fence diagram of temperature and velocity observed in simulation of $k_{aq} = 10^{-9}$ with thickness 600 m. Transects are at 6,000, 8,000, 10,000, and 12,000 m (in domain coordinates) with locations noted in red lines on generalized map view of North Pond. Transects at 6,000 m, 10,000 m, and 12,000 m are contour plots of temperature and transect at 8,000 m is a sample of ~5,000 velocity vector X-Z components colored by temperature at the vector location.

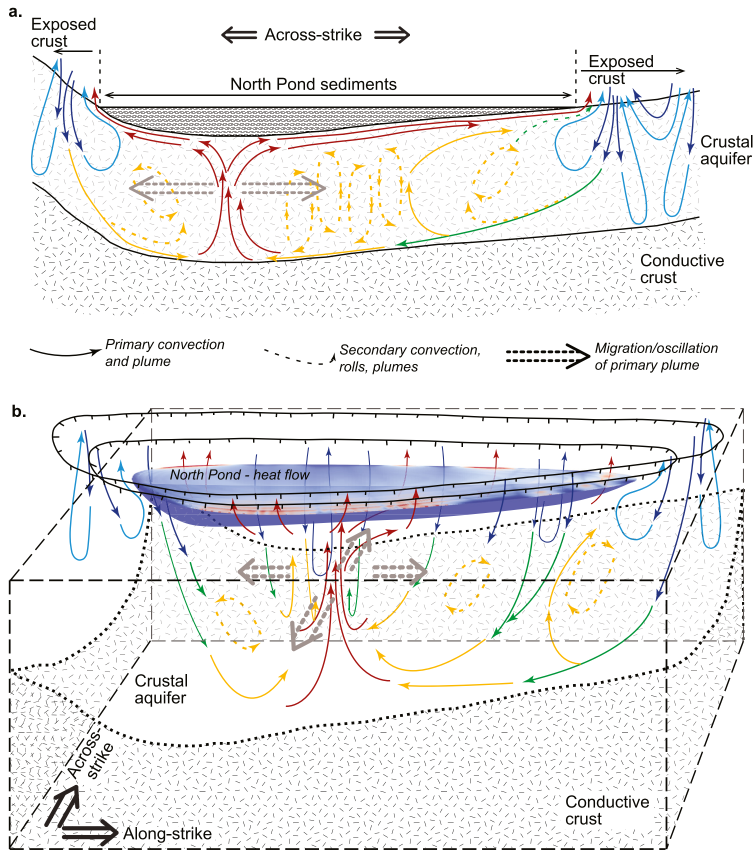

Figure 9. Conceptual diagrams showing key features of fluid-heat transport below North Pond based on observations and coupled simulations. (a) Two-dimensional circulation features. (b) Three-dimensional circulation patterns. Updated conceptual model for three-dimensional flux beneath North Pond. Localized convection and subsequent upwelling and downwelling control the manifestation of surface heat flux. Fluid recharges and discharges diffusely in the outcropping basement surrounding North Pond with very little unidirectional flow.

hydrothermal fluid. Cool and essentially isothermal conditions in the upper few hundred meters of the crustal aquifer are readily explained by vigorous convection that draws in cold bottom water from the seafloor surrounding North Pond, then warms and mixes that fluid before it flows laterally and discharges (Figure 8 and Movie S2).

To the extent that flow in the crustal aquifer never becomes fully stable, as simulated with $k_{aq} = 10^{-11}$–10^{-9} m^2, transient perturbations in temperature and pressure conditions at depth (Becker et al., 2018) require no external forcing. The timescale for the thermal response (τ) of the sedimentary boundary layer forming the thermal lid of North Pond is likely to be on the order of 10^1–10^3 yr, given $\tau = L^2/\kappa$, sediment thickness of $L = 10$–200 m, and thermal diffusivity of $\kappa = 3 \times 10^{-7}$ m^2/s. Therefore, variations in convection patterns on a timescale of $\geq 10^3$–10^4 yr should result in time-varying seafloor heat flux.

The complexity of simulated fluid flow and thermal patterns also help to explain chemical and microbiological observations in North Pond sedimentary and basement fluids. Rapid recharge and lateral circulation close to the sediment-basement contact helps to maintain an oxic and nutrient-rich boundary condition at the base of North

Pond sediments (Orcutt et al., 2013). Closely spaced regions of hydrothermal upflow and downflow, and locations that are more proximal or distal to areas of recharge from around North Pond, will result in differences in fluid residence time and thus oxygen and carbon content. These results help to explain distinct communities of subseafloor microbes that are optimized for processing different oxidants and forms of organic carbon, where the nature of transported fluids varies heterogeneously along distinct flow pathways (Orcutt et al., 2021; Shah Walter et al., 2018; Trembath-Reichert et al., 2021). Hydrodynamic stagnation points between plumes could result in patches of the basement aquifer and adjacent crust that act as reservoirs for older carbon. Transient variations in fluid flow paths and properties are also consistent with temporal variability in microbial ecology (Seyler et al., 2021; Tully et al., 2018).

4.2. Crustal Permeability Below North Pond

Coupled North Pond simulations replicate key aspects of the seafloor heat-flux distribution when crustal aquifer permeability is $k_{aq} = 10^{-11}$–10^{-9} m^2. For $k_{aq} = 10^{-11}$–10^{-10} m^2, two dimensional simulations suppress the seafloor heat flux across much of the pond and elevate heat flux through the remaining sediment (Figure 4). At $k_{aq} = 10^{-9}$ m^2, seafloor heat flux is suppressed across the full two-dimensional profile by 60%–90%. For three-dimensional simulations, $k_{aq} = 10^{-11}$–10^{-10} m^2 does well matching variability in seafloor heat flux, including closely spaced regions of lower and higher heat flux along pond margins, where crustal fluids recharge and discharge, respectively. But none of the three-dimensional simulations completed to date result in the overall fraction of heat-flux suppression observed at North Pond (Figure 5). At $k_{aq} = 10^{-9}$ m^2 in three-dimensional simulations for 600 and 1,000 m aquifers, the median conductive heat flux through North Pond sediments is ∼50% of lithospheric, whereas observations suggest that advective extraction plus refraction results in median heat flux ∼20% of lithospheric, equivalent to ∼55% of the simulated heat output through North Pond sediments. Therefore, an additional ∼55% of simulated heat output must be removed advectively to match observations (Figure S8 in Supporting Information S1).

Interestingly, for $k_{aq} = 10^{-9}$ m^2 and 600 m aquifer, when the heat input at the base of the full simulation domain is lowered by an additional 55%, the heat flux through North Pond sediments is reduced by only ∼10% relative to the full lithospheric input simulations (Figure S8 in Supporting Information S1). Even with lower heat input, vigorous convection in the basement aquifer below North Pond mines and focuses heat from the surrounding crust, reducing the impact of advective heat extraction. This suggests that an anomalously low heat flux from the lithosphere in this area is not likely to explain the low heat flux through North Pond. It is also unlikely that incomplete hydrothermal rebound (Hutnak & Fisher, 2007; Spinelli & Harris, 2011) can explain the remaining difference between simulated and observed heat flux (Supporting Information S1).

The fundamental challenge is that the increase in advective extraction of lithospheric heat results in bending of isotherms deeper in the crust, bringing in more heat from a larger area toward North Pond. As a consequence, the crustal region cooled by convection below North Pond extends laterally well beyond the pond margins, and the size of this region expands with the efficiency of advective heat extraction. This emergent behavior leads to a negative feedback where higher permeability leads to more vigorous local convection, making it easier for crustal heat to escape, but also draws in more heat from a larger region deep in the simulation domain. This suggests that continuing to increase the bulk permeability of the crustal aquifer beyond $k_{aq} = 10^{-9}$ m^2 will not help to match heat-flux observations at the seafloor.

On the southern flank of the Costa Rica Rift, simulations incorporating anisotropy in crustal permeability were found to enhance the lateral redistribution of heat by ridge-flank hydrothermal circulation (Fisher & Becker, 1995; Fisher et al., 1994); this was accomplished numerically by creating thin layers of higher and lower permeability in the upper crust, which encouraged rapid lateral flow and suppressed small-scale convection. Applying a similar approach to the crustal aquifer below North Pond could help to achieve a similar result, better matching thermal observations.

Simulations completed to date have explored processes within isotropic and homogeneous aquifer layers 100–1,000 m thick. Borehole geophysical logs indicate that volcanic basement beneath North Pond is layered at a scale of meters to tens of meters, with alternating massive and porous/brecciated units (Bartetzko et al., 2001; Becker et al., 2001). Rapid transport through thin zones could facilitate more efficient lateral heat extraction while also limiting small-scale convection. It may also be that azimuthal anisotropy helps to partition the removal of crustal heat, with elevated permeability in the along-strike direction in association with abyssal hill topography and the regional crustal fabric (Figures 1 and S1 in Supporting Information S1). Three-dimensional simulations presented in this study show that, for simulations with isotropic crustal permeability, across-strike transport is favored for higher permeability cases (Figures S5 and S6 in Supporting Information S1). Enhancing along-strike permeability, either across the full domain or in swaths representative of fault zones, could shift both large-scale patterns of fluid circulation and enhance the efficiency of heat extraction more generally. Other configurations are possible, including larger-scale and deeper circulation paths that mine crustal heat via lateral circulation, perhaps including flow between adjacent or distant sets of crustal ridges and troughs (Figure 1). At present, it remains challenging to resolve complex patterns of fluid circulation and crustal properties at a setting in which sediment cover is the exception rather than the rule. That said, additional exploration of options for the distribution of crustal permeability should provide useful insights and testable hypotheses.

4.3. North Pond Crustal Hydrogeology Compared to Other Ridge Flanks

Thermal conditions and flow rates around North Pond are similar to those surrounding Dorado outcrop on ~23 M.y. old seafloor formed on the EPR (Hutnak et al., 2008; Lauer et al., 2018; Wheat et al., 2019), where simulated aquifer permeability of 10^{-10}–10^{-9} m^2 is most consistent with cool hydrothermal conditions in the upper crust ($\leq$20°C), lateral fluid flow occurs at $\leq$10 m/yr, and heat flux is suppressed regionally by 60%–90%. In contrast, 3–4 M.y. old seafloor on the eastern flank of the JFR hosts slower ridge-flank circulation, with warmer crustal temperatures (60–70°C), lateral fluid flow in the aquifer <1 m/y, lower crustal permeability, and no measurable regional heat-flux suppression (Hutnak et al., 2006; Winslow et al., 2016). Importantly, both of these systems involve a significant component of outcrop-to-outcrop fluid flow that both drives and dominates the pattern of hydrothermal circulation, where volcanic rock exposure is the exception, and the rest of the seafloor is covered by thick layers of less permeable sediment.

Outcrop-to-outcrop circulation systems are clearly "discharge dominated" (Cann & Strens, 1989; Lauer et al., 2018; Winslow & Fisher, 2015), as the ease of fluid flow at sites of recharge is much higher than that at sites of discharge. Rates of fluid flow and heat extraction through these discharge-dominated hydrothermal siphons are throttled by the limited connectivity between the crust and overlying ocean, caused by the contrast in properties between marine sediments (covering most of the volcanic crust) and spatially rare outcrops. In simulations of outcrop-to-outcrop flow, increasing the permeability and/or surface area of outcrops at discharge sites results in relatively large increases in advective heat extraction, but at lower fluid temperatures. Reducing permeability and/or outcrop size results in lower overall advective heat loss from the crust, but advection occurs at higher fluid temperatures.

The hydrogeologic character of hydrothermal circulation around and below North Pond is defined by both recharge and discharge, meaning water can enter and leave the crust essentially anywhere not covered by sediments. Simulated rates of fluid flow and the efficiency of heat extraction around North Pond are much less limited by discharge dynamics. As a result, some of the lessons learned about relations between crustal permeability and heat extraction at other ridge-flank sites are not applicable to North Pond. Approximations of these distinct systems in two dimensions are different: for outcrop-to-outcrop flow, the two-dimensional simulations tend to require higher crustal permeability to achieve equivalent crustal heat extraction compared to three-dimensional simulations. In contrast, for fluid-heat transport below a sediment pond, two-dimensional simulations appear to be more efficient at extracting heat.

5. Summary and Conclusions

Cool hydrothermal fluids flowing in the volcanic crust below North Pond help to explain a variety of observations, including patterns of heat extraction, deviations and variability in crustal pressures and temperatures, and the presence of cool and oxygen-rich water underlying seafloor sediments. A long-standing conceptual model of North Pond hydrogeology included single-pass flow moving laterally under the sediment pond, but two- and three-dimensional coupled simulations developed for the present study suggest that fluid flow patterns are more complex.

Two-dimensional simulations have fluids entering and exiting the crustal aquifer on both sides of North Pond, and three-dimensional simulations have numerous sites of recharge and discharge surrounding the sediment pond.

Both sets of simulations include shallow circulation pathways, with fluids that recharge and discharge after a short time and with slightly elevated temperatures, and deeper circulation supports development of warmer plumes and longer fluid residence times. Two-dimensional simulations can suppress heat flux across North Pond by ~80% of lithospheric, consistent with observations, when the crustal aquifer is 300–600 m thick and permeability is $k_{aq} = 10^{-9}$ m^2. Three-dimensional simulations are most consistent with spatial heat-flux variability in North Pond for the same aquifer thicknesses and $k_{aq} = 10^{-10}$ m^2, and result in advective removal of lithospheric heat that is closest to observations for $k_{aq} = 10^{-9}$ m^2. Three-dimensional simulations also result in differential pressures, and time varying pressures and temperatures in the crustal aquifer, consistent with observations. These simulations suggest that there are multiple modes of convection active in the crust below North Pond, operating across a range of spatial and temporal scales.

However, three-dimensional North Pond simulations are less efficient at removing lithospheric heat than are two-dimensional simulations with equivalent properties. In numerical studies of other ridge flanks for which volcanic outcrops are limited and surrounded by thick and continuous sediment, the opposite trend emerged, with three-dimensional simulations being more efficient in extracting heat from the crust. We draw two important conclusions from this finding. First, ridge-flank hydrothermal circulation systems below and surrounding sediment ponds are governed by different rules than systems driven by outcrop-to-outcrop flow, even though the fundamental physics is the same. Patterns of fluid circulation for the former are complex and difficult to resolve, whereas flow through the latter systems is geometrically constrained and tends to be discharge dominated, with outflow properties regulating the magnitude of regional heat extraction. Second, while heat extraction by outcrop-to-outcrop hydrothermal systems can match observations using simulations having crustal properties that are isotropic and homogeneous, additional complexity in properties may be required for ridge-flank systems that are characterized by abundant bare rock at the seafloor. This could include more detailed layering of crustal units, anisotropy associated with faulting and broader crustal fabric, and/or heterogeneous property distributions associated with eruptive and intrusive events, layering, and tectonism. We also wonder if there may be a systematic, long-term evolution between the styles of ridge-flank circulation that occur below sediment ponds to more isolated outcrops of exposed basement rocks. These and other issues remain to be explored in future studies.

Simulations are useful for narrowing the range of possible system properties and ranges of flow rates and for developing testable hypotheses, but hard observational constraints are essential for advancing understanding. North Pond is one of the best studied ridge-flank hydrothermal systems on Earth, an important end-member setting for low-temperature hydrogeologic, chemical, and microbiological conditions and processes, yet we are just learning how to map patterns and rates of coupled flow in the crust in this setting. Our understanding of these global systems will continue to improve along with simulation, measurement, and sampling tools and techniques, particularly when integrated through interdisciplinary studies.

Data Availability Statement

Data sets for this research are available in the DRYAD data repository at https://doi.org/10.7291/D1G67P (Price et al., 2021).

Acknowledgments
This research was supported by National Science Foundation grants OIA-0939564 and OCE-1924384 and was motivated and inspired by numerous observations and experiments conducted by researchers who are part of the Center for Dark Energy Biosphere Investigations (C-DEBI) and the Integrated Ocean Drilling Program and its predecessors. An early version of this manuscript benefitted from valuable comments by Keir Becker, and Tess Weathers assisted with development of the simulation scheme. The initial submission was greatly improved by reviews from B. Tutolo and an anonymous reviewer. This is C-DEBI contribution 580.

References

Alt, J. C. (2004). Alteration of the upper oceanic crust: Mineralogy, chemistry, and processes. In *Hydrogeology of the oceanic lithosphere* (pp. 495–433). Cambridge University Press.

Baker, P., Stout, P., Kastner, M., & Elderfield, H. (1991). Large-scale lateral advection of seawater through oceanic crust in the central equatorial Pacific. *Earth and Planetary Science Letters*, *105*, 522–533. https://doi.org/10.1016/0012-821x(91)90189-o

Bartetzko, A., & Fisher, A. T. (2008). Physical properties of young (3.5 Ma) oceanic crust from the eastern flank of the Juan de Fuca Ridge: Comparison of wireline and core measurements with global data. *Journal of Geophysical Research*, *113*(B5), B05105. https://doi.org/10.1029/2007JB005268

Bartetzko, A., Pezard, P., Goldberg, D., Sun, Y.-F., & Becker, K. (2001). Volcanic stratigraphy of DSDP/ODP Hole 395A: An interpretation using well-logging data. *Marine Geophysical Researches*, *22*(2), 111–127.

Becker, K. (1990). Measurements of the permeability of the upper oceanic crust at Hole 395A, ODP Leg 109. In R. Detrick, J. Honnorez, W. B. Bryan, T. Juteau, et al. (Eds.), *Proc. ODP, scientific. Results* (pp. 213–222). https://doi.org/10.2973/odp.proc.sr.106109.146.1990

Becker, K., Bartetzko, A., & Davis, E. E. (2001). Leg 174B synopsis: Revisiting hole 395A for logging and long-term monitoring of off-axis hydrothermal processes in young oceanic crust. In K. Becker, & M. J. Malone (Eds.), *Proceedings of the ocean drilling program, science results* (pp. 1–12). Ocean Drilling Program. https://doi.org/10.2973/odp.proc.sr.174B.2001

Becker, K., & Fisher, A. T. (2008). Borehole packer tests at multiple depths resolve distinct hydrologic intervals in 3.5-Ma upper oceanic crust on the eastern flank of Juan de Fuca Ridge. *Journal of Geophysical Research*, *113*(B7). https://doi.org/10.1029/2007JB005447

Becker, K., Langseth, M. G., & Hyndman, R. D. (1984). Temperature measurements in hole 395A, Leg 78B. In *Initial reports of the Deep Sea drilling Project 78B* (pp. 689–698). U.S. Government Printing Office. https://doi.org/10.2973/dsdp.proc.78b.105.1984

Becker, K., Langseth, M. G., Von Herzen, R. P., & Anderson, R. N. (1983). Deep crustal geothermal measurements, hole 504B, Costa Rica Rift. *Journal of Geophysical Research*, *88*(B4), 3447–3457. https://doi.org/10.1029/JB088iB04p03447

Becker, K., Morin, R. H., & Davis, E. E. (1994). Permeabilities in the Middle Valley hydrothermal system measured with packer and flowmeter experiments. In *Proceedings of the ocean drilling program* (pp. 613–626). Scientific results. https://doi.org/10.2973/odp.proc.sr.139.252.1994

Becker, K., Wheat, C. G., Villinger, H. W., & Davis, E. (2018). New long-term subseafloor pressure records from the IODP expedition 336 CORKs at North pond, western flank of the mid-Atlantic Ridge. In *AGU fall meeting abstracts* (pp. V43G–V0216).

Blackwell, D. D., Steele, J. L., & Brott, C. A. (1980). The terrain effect on terrestrial heat flow. *Journal of Geophysical Research*, *85*(B9), 4757–4772. https://doi.org/10.1029/JB085iB09p04757

Cann, J. R., & Strens, M. R. (1989). Modeling periodic megaplume emission by black smoker systems. *Journal of Geophysical Research*, *94*(B9), 12227–12237. https://doi.org/10.1029/JB094iB09p12227

Criss, R. E., & Hofmeister, A. M. (1991). Application of fluid dynamics principles in tilted permeable media to terrestrial hydrothermal systems. *Geophysical Research Letters*, *18*(2), 199–202. https://doi.org/10.1029/91GL00216

Davis, E. E., Chapman, D. S., Mottl, M. J., Bentkowski, W. J., Dadey, K., Forster, C., et al. (1992). FlankFlux: An experiment to study the nature of hydrothermal circulation in young oceanic crust. *Canadian Journal of Earth Sciences*, *29*(5), 925–952. https://doi.org/10.1139/e92-078

Edwards, K. J., Bach, W., Klaus, A., & the Expedition 336 Scientists. (2012). *Proceedings of the integrated ocean drilling program volume 336 expedition reports* (p. 16).

Edwards, K. J., Becker, K., & Colwell, F. (2012). The deep, dark energy biosphere: Intraterrestrial life on earth. *Annual Review of Earth and Planetary Sciences*, *40*(1), 551–568. https://doi.org/10.1146/annurev-earth-042711-105500

Elderfield, H., & Schultz, A. (1996). Mid-ocean ridge hydrothermal fluxes and the chemical composition of the ocean. *Annual Review of Earth and Planetary Sciences*, *24*(1), 191–224. https://doi.org/10.1146/annurev.earth.24.1.191

Elderfield, H., Wheat, C. G., Mottl, M. J., Monnin, C., & Spiro, B. (1999). Fluid and geochemical transport through oceanic crust: A transect across the eastern flank of the Juan de Fuca Ridge. *Earth and Planetary Science Letters*, *172*(1–2), 151–165. https://doi.org/10.1016/S0012-821X(99)00191-0

Expedition 336 Scientists. (2012). Expedition 336 summary. *Proceedings of the Integrated Ocean Drilling Program*, *336*. https://doi.org/10.2204/iodp.proc.336.101.2012

Fisher, A. T. (2003). Geophysical constraints on hydrothermal circulation: Observations and models. In P. Halbach, V. Tunnicliffe, & J. Hein (Eds.), *Energy and mass transfer in submarine hydrothermal systems* (pp. 29–52). Dahlem University Press.

Fisher, A. T., Alt, J., & Bach, W. (2014). Hydrogeologic properties, processes, and alteration in the igneous ocean crust. In *Developments in marine geology* (pp. 507–551). Elsevier. https://doi.org/10.1016/B978-0-444-62617-2.00018-9

Fisher, A. T., & Becker, K. (1995). Correlation between sea-floor heat-flow and basement relief: Observational and numerical examples and implications for upper crustal permeability. *Journal of Geophysical Research*, *100*(B7), 12641–12657. https://doi.org/10.1029/95JB00315

Fisher, A. T., Becker, K., & Davis, E. E. (1997). The permeability of young oceanic crust east of Juan de Fuca Ridge Determined using borehole thermal measurements. *Geophysical Research Letters*, *24*(11), 1311–1314. https://doi.org/10.1029/97GL01286

Fisher, A. T., Becker, K., & Narasimhan, T. N. (1994). Off-axis hydrothermal circulation: Parametric tests of a refined model of processes at deep sea drilling project/ocean drilling program site 504. *Journal of Geophysical Research*, *99*(B2), 3097–3121. https://doi.org/10.1029/93JB02741

Fisher, A. T., & Harris, R. N. (2010). Using seafloor heat flow as a tracer to map subseafloor fluid flow in the ocean crust. *Geofluids*, *10*(1–2), 142–160. https://doi.org/10.1111/j.1468-8123.2009.00274.x

Fisher, A. T., Stein, C. A., Harris, R. N., Wang, K., Silver, E. A., Pfender, M., et al. (2003). Abrupt thermal transition reveals hydrothermal boundary and role of seamounts within the Cocos Plate. *Geophysical Research Letters*, *30*(11). https://doi.org/10.1029/2002GL016766

Fisher, A. T., & Wheat, C. G. (2010). Seamounts as conduits for massive fluid, heat, and solute fluxes on ridge flanks. *Oceanography*, *23*(01), 74–87. https://doi.org/10.5670/oceanog.2010.63

Gable, R., Morin, R. H., & Becker, K. (1992). Geothermal state of DSDP holes 333A, 395A and 534A: Results from the dianaut Program. *Geophysical Research Letters*, *19*(5), 505–508. https://doi.org/10.1029/92GL00333

Hasterok, D. (2013a). Global patterns and vigor of ventilated hydrothermal circulation through young seafloor. *Earth and Planetary Science Letters*, *380*, 12–20. https://doi.org/10.1016/j.epsl.2013.08.016

Hasterok, D. (2013b). A heat flow based cooling model for tectonic plates. *Earth and Planetary Science Letters*, *361*, 34–43. https://doi.org/10.1016/j.epsl.2012.10.036

Hussong, D. M., Fryer, P. B., Tuthill, J. D., & Wipperman, L. K. (1979). The geological and geophysical setting near DSDP Site 395, North Atlantic Ocean. *Melson, WG, Rabinowitz, PD, et al., Init. Repts. DSDP*, *45*, 23–37.

Hutnak, M., & Fisher, A. T. (2007). Influence of sedimentation, local and regional hydrothermal circulation, and thermal rebound on measurements of seafloor heat flux. *Journal of Geophysical Research*, *112*(B12). https://doi.org/10.1029/2007JB005022

Hutnak, M., Fisher, A. T., Harris, R., Stein, C., Wang, K., Spinelli, G., et al. (2008). Large heat and fluid fluxes driven through mid-plate outcrops on ocean crust. *Nature Geoscience*, *1*(9), 611–614. https://doi.org/10.1038/ngeo264

Hutnak, M., Fisher, A. T., Zühlsdorff, L., Spiess, V., Stauffer, P. H., & Gable, C. W. (2006). Hydrothermal recharge and discharge guided by basement outcrops on 0.7–3.6 Ma seafloor east of the Juan de Fuca Ridge: Observations and numerical models. *Geochemistry, Geophysics, Geosystems*, *7*(7). https://doi.org/10.1029/2006GC001242

Johnson, H. P., & Pruis, M. J. (2003). Fluxes of fluid and heat from the oceanic crustal reservoir. *Earth and Planetary Science Letters*, *216*(4), 565–574. https://doi.org/10.1016/S0012-821X(03)00545-4

Kadko, D., Baross, J., & Alt, J. (1995). The magnitude and global implications of hydrothermal flux. In *Seafloor hydrothermal systems: Physical, chemical, biological, and geological interactions* (pp. 446–466). American Geophysical Union (AGU). https://doi.org/10.1029/GM091p0446

Lachenbruch, A. H. (1968). Rapid estimation of the topographic disturbance to superficial thermal gradients. *Reviews of Geophysics*, *6*(3), 365–400. https://doi.org/10.1029/RG006i003p00365

Langseth, M. G., Becker, K., Von Herzen, R. P., & Schultheiss, P. (1992). Heat and fluid flux through sediment on the western flank of the mid-Atlantic Ridge: A hydrogeological study of North pond. *Geophysical Research Letters*, *19*(5), 517–520. https://doi.org/10.1029/92GL00079

Langseth, M. G., Hyndman, R. D., Becker, K., Hickman, S. H., & Salisbury, M. H. (1984). The hydrogeological regime of isolated sediments ponds in mid-oceanic ridges. In *Initial reports of the deep sea drilling Project, 78B* (pp. 825–837). https://doi.org/10.2973/dsdp.proc.78b.1984

Lauer, R. M., Fisher, A. T., & Winslow, D. M. (2018). Three-dimensional models of hydrothermal circulation through a seamount network on fast-spreading crust. *Earth and Planetary Science Letters*, *501*, 138–151. https://doi.org/10.1016/j.epsl.2018.08.025

Lawrence, J., Drever, J., & Kastner, M. (1978). Low temperature alteration of basalts predominates at DSDP Site 395. *Initial Reports of the Deep Sea Drilling Project*, *45*, 609–612.

Lawrence, J. R., & Drever, J. I. (1981). Evidence for cold water circulation at DSDP site 395: Isotopes and chemistry of alteration products. *Journal of Geophysical Research*, *86*(B6), 5125–5133. https://doi.org/10.1029/JB086iB06p05125

Lawrence, J. R., & Gieskes, J. M. (1981). Constraints on water transport and alteration in the oceanic crust from the isotopic composition of pore water. *Journal of Geophysical Research*, *86*(B9), 7924–7934. https://doi.org/10.1029/JB086iB09p07924

Lee, T.-C. (1991). On terrain corrections in terrestrial heat flow. *Pure and Applied Geophysics*, *135*(1), 1–13. https://doi.org/10.1007/BF00877005

Los Alamos Grid Toolbox, LaGriT. (2019). *Los Alamos national laboratory*. Retrieved from http://lagrit.lanl.gov

Mathews, M., Salisbury, M., Hyndman, R., (1984). Basement logging on the Mid-Atlantic Ridge, deep sea drilling project hole 395A. *Init. Repts. DSDP B*, *78*, 717–730. https://doi.org/10.2973/dsdp.proc.78b.108.1984

McDuff, R. E. (1984). The chemistry of interstitial waters from the upper ocean crust, Site 395, deep sea drilling project leg 78B. In R. D. Hyndman, M. H. Salisbury (Eds.), *Init. Repts. DSDP, 78B* (pp. 795–799). U.S. Govt. Printing Office. https://doi.org/10.2973/dsdp.proc.78b.114.1984

Melson, W. G., Rabinowitz, P. D., Natland, J. H., Bougault, H., & Johnson, H. P. (1979). Cruise objectives and major results, analytical procedures, and explanatory notes. *Initial Reports of the Deep Sea Drilling Project*, *45*, 5–20.

Meyer, J. L., Jaekel, U., Tully, B. J., Glazer, B. T., Wheat, C. G., Lin, H.-T., et al. (2016). A distinct and active bacterial community in cold oxygenated fluids circulating beneath the western flank of the Mid-Atlantic ridge. *Scientific Reports*, *6*(1), 22541. https://doi.org/10.1038/srep22541

Moos, D. (1990). Petrophysical results from logging in DSDP hole 395A, ODP Leg 109. *Proceedings of the Ocean Drilling Program, Scientific Results*, *106109*, 237–253.

Morin, R. H., Hess, A. E., & Becker, K. (1992). In situ measurements of fluid flow in DSDP Holes 395A and 534A: Results from the Dianaut program. *Geophysical Research Letters*, *19*(5), 509–512. https://doi.org/10.1029/91GL02947

Mottl, M. J., Wheat, G., Baker, E., Becker, N., Davis, E., Feely, R., et al. (1998). Warm springs discovered on 3.5 Ma oceanic crust, eastern flank of the Juan de Fuca Ridge. *Geology*, *26*(1), 51–54. https://doi.org/10.1130/0091-7613(1998)026<0051:WSDOMO>2.3.CO;2

Orcutt, B., Wheat, C., Rouxel, O., Hulme, S., Edwards, K. J., & Bach, W., (2013). Oxygen consumption rates in subseafloor basaltic crust derived from a reaction transport model. *Nature Communications*, *4*, 2539. https://doi.org/10.1038/ncomms3539

Orcutt, B. N., D'Angelo, T., Wheat, C. G., & Trembath-Reichert, E. (2021). Microbe-mineral biogeography from multi-year incubations in oceanic crust at North Pond, Mid-Atlantic Ridge. *Environmental Microbiology*, *23*. https://doi.org/10.1111/1462-2920.15366

Orcutt, B. N., Sylvan, J. B., Rogers, D. R., Delaney, J., Lee, R. W., & Girguis, P. R. (2015). Carbon fixation by basalt-hosted microbial communities. *Frontiers in Microbiology*, *6*, 904. https://doi.10.3389/fmicb.2015.00904

Parsons, B., & Sclater, J. G. (1977). An analysis of the variation of ocean floor bathymetry and heat flow with age. *Journal of Geophysical Research*, *82*(5), 803–827. https://doi.org/10.1029/JB082i005p00803

Peacock, S. M., & Wang, K. (1999). Seismic consequences of warm versus cool subduction metamorphism: Examples from Southwest and Northeast Japan. *Science*, *286*(5441), 937–939. https://doi.org/10.1126/science.286.5441.937

Price, A. N., Fisher, A. T., Stauffer, P. H., & Gable, C. W. (2021). Data from: Numerical simulation of cool hydrothermal processes in the upper volcanic crust beneath a marine sediment pond: North Pond, North Atlantic Ocean [Dataset], Dryad. https://doi.org/10.7291/D1G67P

Reese, B. K., Zinke, L. A., Sobol, M. S., LaRowe, D. E., Orcutt, B. N., Zhang, X., et al. (2018). Nitrogen cycling of active bacteria within oligotrophic sediment of the mid-Atlantic Ridge flank. *Geomicrobiology Journal*, *35*(6), 468–483. https://doi.org/10.1080/01490451.2017.1392649

Ryan, W. B. F., Carbotte, S. M., Coplan, J. O., O'Hara, S., Melkonian, A., Arko, R., et al. (2009). Global multi-resolution topography synthesis. *Geochemistry, Geophysics, Geosystems*, *10*(3). https://doi.org/10.1029/2008GC002332

Schmidt-Schierhorn, F., Kaul, N., Stephan, S., & Villinger, H. (2012). In K. J. Edwards, W. Bach, A. Klaus, & the Expedition, 336 (Eds.), *Geophysical site survey results from North pond (mid-Atlantic Ridge)*.

Seyler, L. M., Trembath-Reichert, E., Tully, B. J., & Huber, J. A. (2021). Time-series transcriptomics from cold, oxic subseafloor crustal fluids reveals a motile, mixotrophic microbial community. *The ISME Journal*, *15*(4), 1192–1206. https://doi.org/10.1038/s41396-020-00843-4

Shah Walter, S. R., Jaekel, U., Osterholz, H., Fisher, A. T., Huber, J. A., Pearson, A., et al. (2018). Microbial decomposition of marine dissolved organic matter in cool oceanic crust. *Nature Geoscience*, *11*(5), 334–339. https://doi.org/10.1038/s41561-018-0109-5

Shipboard Scientific Party. (1997). Rough basement transect (sites 1026 and 1027). In E. E. Davis, A. T. Fisher, & J. Firth (Eds.), *Proceedings of the ocean drilling program initial reports, 168* (pp. 101–160). Ocean Drilling Program. https://doi.org/10.2973/odp.proc.ir.168.105.1997

Spinelli, G. A., Giambalvo, E. R., & Fisher, A. T. (2004). Sediment permeability, distribution, and influence on fluxes in oceanic basement. In E. E. Davis, & H. Elderfield (Eds.), *Hydrogeology of the oceanic lithosphere* (pp. 151–188). Cambridge University Press.

Spinelli, G. A., & Harris, R. N. (2011). Effects of the legacy of axial cooling on partitioning of hydrothermal heat extraction from oceanic lithosphere. *Journal of Geophysical Research*, *116*(B9). https://doi.org/10.1029/2011JB008248

Stauffer, P. H., Lewis, K. C., Stein, J. S., Travis, B. J., Lichtner, P., & Zyvoloski, G. (2014). Joule–thomson effects on the flow of liquid water. *Transport in Porous Media*, *105*(3), 471–485. https://doi.org/10.1007/s11242-014-0379-3

Stein, C., & Stein, S. (1994). Constraints on hydrothermal heat-flux through the oceanic lithosphere from global heat-flow. *Journal of Geophysical Research*, *99*(B2), 3081–3095. https://doi.org/10.1029/93JB02222

Stein, J. S., & Fisher, A. T. (2003). Observations and models of lateral hydrothermal circulation on a young ridge flank: Numerical evaluation of thermal and chemical constraints. *Geochemistry, Geophysics, Geosystems*, *4*(3). https://doi.org/10.1029/2002GC000415

Trembath-Reichert, E., Walter, S. R. S., Ortiz, M. A. F., Carter, P. D., Girguis, P. R., & Huber, J. A. (2021). Multiple carbon incorporation strategies support microbial survival in cold subseafloor crustal fluids. *Science Advances*, *7*(18), eabg0153. https://doi.org/10.1126/sciadv.abg0153

Tully, B. J., Wheat, C. G., Glazer, B. T., & Huber, J. A. (2018). A dynamic microbial community with high functional redundancy inhabits the cold, oxic subseafloor aquifer. *The ISME Journal*, *12*(1), 1–16. https://doi.org/10.1038/ismej.2017.187

Underwood, M. B., Hoke, K. D., Fisher, A. T., Davis, E. E., Giambalvo, E., Zühlsdorff, L., & Spinelli, G. A. (2005). Provenance, stratigraphic architecture, and hydrogeologic influence of turbidites on the mid-ocean ridge flank of northwestern cascadia basin, Pacific ocean. *Journal of Sedimentary Research*, *75*(1), 149–164. https://doi.org/10.2110/jsr.2005.012

Versteegh, G. J. M., Koschinsky, A., Kuhn, T., Preuss, I., & Kasten, S. (2021). Geochemical consequences of oxygen diffusion from the oceanic crust into overlying sediments and its significance for biogeochemical cycles based on sediments of the northeast Pacific. *Biogeosciences*, *18*(17), 4965–4984. https://doi.org/10.5194/bg-18-4965-2021

Villinger, H., Strack, A., Gaide, S., & Thal, J. (2018). *Gridded bathymetry of North Pond (MAR) from multibeam echosounder EM120 and EM122 data of cruises MSM20/5 (2012) and MSM37 (2014)*. Department of Geosciences, Bremen University. https://doi.org/10.1594/PANGAEA.889439

Villinger, H. W., Müller, P., Bach, W., Becker, K., Orcutt, B. N., Kaul, N., & Wheat, C. G. (2019). Evidence for low-temperature diffuse venting at North pond, western flank of the mid-Atlantic Ridge. *Geochemistry, Geophysics, Geosystems*, *20*(6), 2572–2584. https://doi.org/10.1029/2018GC008113

Wankel, S. D., Buchwald, C., Ziebis, W., Wenk, C. B., & Lehmann, M. F. (2015). Nitrogen cycling in the deep sedimentary biosphere: Nitrate isotopes in porewaters underlying the oligotrophic North Atlantic. *Biogeosciences*, *12*(24), 7483–7502. https://doi.org/10.5194/bg-12-7483-2015

Wheat, C. G., Becker, K., Villinger, H., Orcutt, B. N., Fournier, T., Hartwell, A., & Paul, C. (2020). Subseafloor cross-hole tracer experiment reveals hydrologic properties, heterogeneities, and reactions in slow-spreading oceanic crust. *Geochemistry, Geophysics, Geosystems*, *21*(1), e2019GC008804. https://doi.org/10.1029/2019GC008804

Wheat, C. G., Edwards, K. J., Pettigrew, T., Jannasch, H. W., Becker, K., Davis, E. E., et al. (2012). CORK-Lite: Bringing legacy boreholes back to life. *Scientific Drilling*, *14*, 39–43. https://doi.org/10.5194/sd-14-39-2012

Wheat, C. G., & Fisher, A. T. (2008). Massive, low-temperature hydrothermal flow from a basaltic outcrop on 23 Ma seafloor of the Cocos Plate: Chemical constraints and implications. *Geochemistry, Geophysics, Geosystems*, *9*(12). https://doi.org/10.1029/2008GC002136

Wheat, C. G., Fisher, A. T., McManus, J., Hulme, S. M., & Orcutt, B. N. (2017). Cool seafloor hydrothermal springs reveal global geochemical fluxes. *Earth and Planetary Science Letters*, *476*, 179–188. https://doi.org/10.1016/j.epsl.2017.07.049

Wheat, C. G., Hartwell, A. M., McManus, J., Fisher, A. T., Orcutt, B. N., Schlicht, L. E. M., et al. (2019). Geology and fluid discharge at Dorado outcrop, a low temperature ridge-flank hydrothermal system. *Geochemistry, Geophysics, Geosystems*, *20*(1), 487–504. https://doi.org/10.1029/2018GC007933

Wheat, C. G., Jannasch, H. W., Kastner, M., Plant, J. N., DeCarlo, E. H., & Lebon, G. (2004). Venting formation fluids from deep-sea boreholes in a Ridge flank setting: ODP sites 1025 and 1026. *Geochemistry, Geophysics, Geosystems*, *5*(8). https://doi.org/10.1029/2004GC000710

Wheat, C. G., & Mottl, M. J. (2000). Composition of pore and spring waters from baby bare: Global implications of geochemical fluxes from a Ridge flank hydrothermal system. *Geochimica et Cosmochimica Acta*, *64*(4), 629–642. https://doi.org/10.1016/S0016-7037(99)00347-6

Winslow, D. M., Fisher, A., & Becker, K. (2013). Characterizing borehole fluid flow and formation permeability in the ocean crust using linked analytic models and Markov chain Monte Carlo analysis. *Geochemistry, Geophysics, Geosystems*, *14*(9), 3857–3874.

Winslow, D. M., & Fisher, A. T. (2015). Sustainability and dynamics of outcrop-to-outcrop hydrothermal circulation. *Nature Communications*, *6*(1), 1–7. https://doi.org/10.1038/ncomms8567

Winslow, D. M., Fisher, A. T., Stauffer, P. H., Gable, C. W., & Zyvoloski, G. A. (2016). Three-dimensional modeling of outcrop-to-outcrop hydrothermal circulation on the eastern flank of the Juan de Fuca Ridge. *Journal of Geophysical Research: Solid Earth*, *121*(3), 1365–1382. https://doi.org/10.1002/2015JB012606

Zhang, X., Fang, J., Bach, W., Edwards, K. J., Orcutt, B. N., & Wang, F. (2016). Nitrogen stimulates the growth of subsurface basalt-associated microorganisms at the western flank of the mid-Atlantic Ridge. *Frontiers in Microbiology*, *0*. https://doi.org/10.3389/fmicb.2016.00633

Ziebis, W., McManus, J., Ferdelman, T., Schmidt-Schierhorn, F., Bach, W., Muratli, J., et al. (2012). Interstitial fluid chemistry of sediments underlying the North Atlantic gyre and the influence of subsurface fluid flow. *Earth and Planetary Science Letters*, *323*(324), 79–91. https://doi.org/10.1016/j.epsl.2012.01.018

Zyvoloski, G. A., Robinson, B. A., Dash, Z. V., Kelkar, S., Viswanathan, H. S., Pawar, R. J., et al. (2015). *Software users manual (UM) for the FEHM application version 3.1 - 3.X*. Los Alamos National Laboratory.

References From the Supporting Information

Fisher, A. T. (2003). Geophysical Constraints on Hydrothermal Circulation Observations and Models. In *Energy and mass transfer in submarine hydrothermal systems* (pp. 29–52).

Hasterok, D. (2013). A heat flow based cooling model for tectonic plates. *Earth and Planetary Science Letters*, *361*, 34–43. https://doi.org/10.1016/j.epsl.2012.10.036

Hobart, M., Langseth, M., & Anderson, R. N. (1985). A Geothermal and Geophysical Survey on the South Flank of the Costa Rica Rift: Sites 504 and 505. https://doi.org/10.2973/DSDP.PROC.83.122.1985

Hutnak, M., Fisher, A., Harris, R., Stein, C., Wang, K., Spinelli, G., et al. (2008). Large heat and fluid fluxes driven through mid-plate outcrops on ocean crust. *Nature Geoscience*, *1*, 611–614. https://doi.org/10.1038/ngeo264

Hutnak, M., & Fisher, A. T. (2007). Influence of sedimentation, local and regional hydrothermal circulation, and thermal rebound on measurements of seafloor heat flux. *Journal of Geophysical Research: Solid Earth*, *112*(B12). https://doi.org/10.1029/2007JB005022

Ingebritsen, S. E., & Sanford, W. E. (1999). *Groundwater in Geologic Processes*. Cambridge University Press.

Langseth, M. G., von Herzen, R. P., Becker, K., Müller, P., & Villinger, H. (2018). Heat flux in sedimented ponds, MAR-flanks 22-24°N, RV Atlantis II 123-2, 1989. *PANGAEA*. https://doi.org/10.1594/PANGAEA.896168

Nield, D. A. (1968). Onset of thermohaline convection in a porous medium. *Water Resources Research*, *4*, 553–560. https://doi.org/10.1029/wr004i003p00553

Parsons, B., & Sclater, J. G. (1977). An analysis of the variation of ocean floor bathymetry and heat flow with age. *Journal of Geophysical Research*, *82*(5), 803–827. https://doi.org/10.1029/JB082i005p00803

Schmidt-Schierhorn, F., Kaul, N., Stephan, S., & Villinger, H. (2012). Geophysical site survey results from North Pond (mid-Atlantic Ridge) In Edwards K. J., Bach W., Klaus A., & the Expedition 336 Scientists (Eds.), *Proceedings of the IODP* (Vol. 336). *Integrated Ocean Drilling Program Management International, Inc*. https://doi.org/10.2204/iodp.proc.336.107.2012

Spinelli, G. A., & Harris, R. N. (2011). Effects of the legacy of axial cooling on partitioning of hydrothermal heat extraction from oceanic lithosphere. *Journal of Geophysical Research: Solid Earth*, *116*(B9). https://doi.org/10.1029/2011JB008248

Stein, C., & Stein, S. (1994). Constraints on hydrothermal heat flux through the oceanic lithosphere from global heat flow. *Journal of Geophysical Research-Solid Earth*, *99*(B2), 3081–3095. https://doi.org/10.1029/93JB02222

Villinger, H., Strack, A., Gaide, S., & Thal, J. (2018). Gridded bathymetry of North Pond (MAR) from multibeam echosounder EM120 and EM122 data of cruises MSM20/5 (2012) and MSM37 (2014) [Dataset]. Department of Geosciences, Bremen University, PANGAEA. https://doi.org/10.1594/PANGAEA.889439

Chapter 2: The Influence of Permeability Anisotropy in the Upper Ocean Crust on Advective Heat Transport by a Ridge-flank Hydrothermal System

Abstract

The influence of permeability anisotropy related to crustal structure on the hydrogeological regimes has been neglected in earlier simulations of ridge-flank hydrothermal systems. North Pond, a marine sediment pond, is a low-temperature, end-member ridge-flank hydrothermal system on ~8 Ma seafloor in the North Atlantic. Previous simulations of North Pond elucidated important crustal processes and long-standing hypotheses concerning hydrothermal fluid and heat transport in the upper volcanic crust but failed to fully explain observed patterns of seafloor heat flux in this area. Here we use variography, a geostatistical method, to quantify relations between seafloor heat-flux measurements, and coupled numerical simulations of fluid and heat flow to permeability anisotropy in the volcanic crust on hydrogeology and advective heat transport in the crustal aquifer beneath North Pond. Directional variography shows that heat flux observations are correlated along-strike of the regional crustal fabric. Three-dimensional simulations that include permeability anisotropy are able to replicate seafloor heat flux patterns across North Pond. However, the simulations that result in the closest match to thermal data incorporate permeability anisotropy in the horizontal (x-y) plane. The feedback between permeability anisotropy and the asymmetric geometry North Pond geometry combine to produce a more efficient mode of advective removal of heat and mass within the crustal aquifer. These findings motivate the exploration of how permeability anisotropy in the volcanic upper crust may influence ridge-flank hydrothermal circulation more broadly.

2.1 Introduction

2.1.1 Ridge-flank hydrothermal circulation as a global hydrologic process

Low- and moderate-temperature seafloor hydrothermal circulation on the flanks of mid-ocean ridges is responsible for the advective removal of ~20% of Earth's heat (Hasterok, 2013). Ridge-flank hydrothermal systems are globally pervasive and circulate the volume of Earth's ocean every ~10^5 to 10^6 years (Kadko et al., 1995), which has profound effects on the thermal evolution of the lithosphere, the geochemistry of the ocean, and maintains a vast crustal biosphere (Edwards et al., 2012).

Ridge-flank hydrothermal systems are easiest to investigate where fluid flow in and out of the seafloor is restricted by the presence of seafloor sediment, with either slow seepage through thin sediments (Giambalvo et al., 2002; Wheat and McDuff, 1995) or near highly permeable volcanic outcrops that provide pathways to bypass lower-permeability sediments (Davis et al., 1992; Fisher et al., 2003). Sediments above the volcanic crust limit vertical exchange with the overlying ocean, form a conductive boundary layer through which seafloor heat flux can be measured, and facilitate the lateral transport of hydrothermal fluids across tens of kilometers (Hutnak et al., 2008; Langseth et al., 1992).

Within ridge-flank hydrothermal systems, there is a trade-off between fluid residence time and the temperature of water-rock reactions, controlled in part by the permeability of the ocean crustal aquifer through which most fluid flow occurs. Rapid lateral fluid flow can be very efficient in cooling the upper crust and removing lithospheric heat, and this tends to occur at relatively low temperatures and in settings where there is extensive exposure of basement rocks and/or high crustal permeability

(Davis et al., 1992). In contrast, when lateral flow is slower, temperatures of water-rock interaction and fluid discharge tend to be higher, but relatively less lithospheric heat is advected from the crust as a result (Fisher et al., 2003).

Here we present simulations of hydrothermal circulation below and around North Pond, a sediment pond on the western flank of the Mid-Atlantic Ridge (MAR). North Pond hosts a low-temperature hydrothermal system with inferred rapid lateral fluid flow in the volcanic upper crust below marine sediments and heat flux at the seafloor that tends to be well below lithospheric values (Langseth et al., 1992, 1984; Schmidt-Schierhorn et al., 2012). An earlier numerical study of this system explored system geometry and bulk formation properties, including permeability in the upper crust, as needed to explain patterns of seafloor heat flux (Price et al., 2022). In the present study, we examine the potential influence of crustal anisotropy on fluid flow and associated heat extraction.

2.1.2 Field setting for North Pond, western flank of the Mid-Atlantic Ridge

North Pond is located on ~8 M.y. old seafloor west of the MAR in a bathymetric depression filled with pelagic sediments (seafloor depth ~4,400 m), surrounded by exposed basaltic rocks of the volcanic upper crust (**Figure 2-1**). Multibeam mapping and seismic reflection profiling across North Pond (Schmidt-Schierhorn et al., 2012) reveal an asymmetric basin, with steeper slopes defined by the sediment-basement interface along the western and southern margins and shallower slopes to the north and east. The maximum sediment thickness in North Pond is ~250 m. North Pond is roughly oval in shape, with dimensions of ~8 x 14 km to the edges of sediment, with the long axis of

North Pond rotated by ~20° east with respect to the general crustal fabric (~N10ºE) defined by fault-bounded abyssal hills and other features (**Figure 2-1**). Throughout this study, we refer to both the long axis of North Pond and the general trend of crustal fabric as being "along-strike," and the orthogonal direction as being "across-strike".

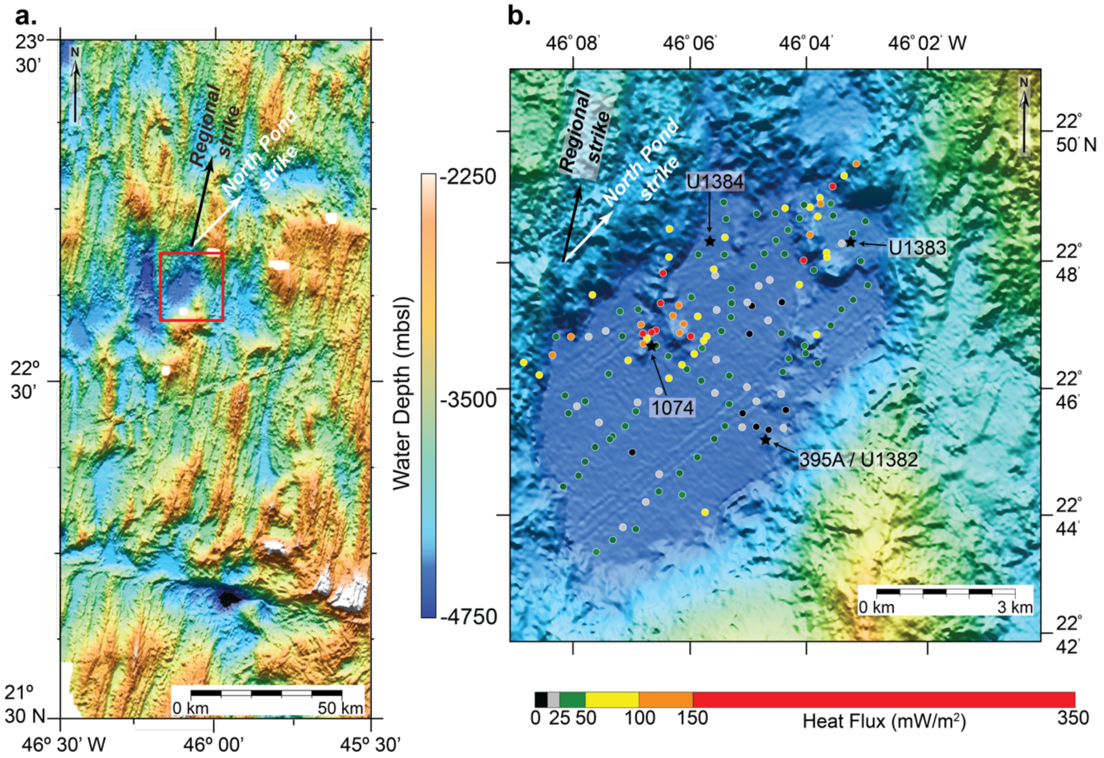

Figure 2-1: Maps showing field setting, bathymetry, and seafloor heat flux. **A.** Regional bathymetry around North Pond on the western flank of the Mid-Atlantic Ridge. Regional strike of crustal fabric is ~N10°E (white arrow) and the North Pond basin with the long axis striking ~N30°E (black arrow). Red box is the area shown in greater detail in figure b. Base map made with GeoMapApp (www.geomapapp.org) / CC BY. **B.** Bathymetric map of North Pond and surrounding seafloor overlain with heat flux data (Langseth et al., 1992; Schmidt-Schierhorn et al., 2012), and borehole locations (black stars).

North Pond has been the focus of numerous coring, drilling, geophysical, geochemical, and microbiological studies, and is considered to be a type setting or end-member for ridge-flank hydrothermal processes involving rapid flow of cool crustal fluids. Seafloor heat flux measurements in North Pond (Langseth et al., 1992, 1984; Schmidt-Schierhorn et al., 2012) indicate a median of 37 mW/m^2 (majority of values ~10 to 60 mW/m^2), considerably lower than the lithospheric input of ~180 mW/m^2 (Harris and Chapman, 2004). An early interpretation of the seafloor heat flux distribution suggested dominantly advective heat extraction from the volcanic crust below North Pond, with a single-pass, east-to-west flow geometry aligned with the short axis (across-strike) of the basin (Langseth et al., 1984).

A recent study of North Pond hydrogeology using two- and three-dimensional numerical simulations found more complex, time-varying fluid-flow geometries (Price et al., 2022). Relatively high permeabilities were needed for upper crustal aquifer layers ($k_{aq} = 10^{-11}$ to 10^{-9} m^2) to replicate key observations from North Pond. These simulations replicated advective extraction of a large fraction of lithospheric heat, small-scale spatial variations in seafloor heat flux (including elevated and suppressed values within 10s to 100s of meters of each other), little or no seepage of fluids through North Pond sediments, transient changes in upper crustal temperatures, and small underpressures and overpressures in different crustal locations and depths (Becker et al., 2022; Langseth et al., 1992; McDuff, 1984; Price et al., 2022; Wheat et al., 2020). However, three-dimensional simulations that best matched average and small-scale variations in seafloor heat flux had different permeability values, and none of the simulations completed previously were able to replicate the extent of advective heat extraction from the volcanic crust below North Pond (Price et al., 2022). Although these earlier simulations included crustal layering and property variations with depth, permeabilities were isotropic within each unit.

2.1.3 Evidence for anisotropy in the upper volcanic ocean crust on ridge flanks

Multiple studies have investigated azimuthal seismic anisotropy within the upper ocean crust flanks (Detrick et al., 1998; Fryer et al., 1989; Stephen, 1981), thought to be associated mainly with faults and cracks that develop in response to tectonic stresses during and after crustal formation. Fast-spreading crust tends to be characterized by more common magmatic centers and more frequent eruptions, whereas slow-spreading seafloor may be more extensively influenced by tectonic processes (Delaney et al., 1998; Karson, 2002; Karson and Elthon, 1987), so one might anticipate greater anisotropy on moderate- to slow-spreading ridge flanks. Anisotropy leading to azimuthal differences in permeability is not well constrained in the ocean crust, in part because of limited access to the upper crustal aquifer. Boreholes that penetrate beyond the upper 100-200 m sub-basement (msb) are relatively rare in the history of scientific ocean drilling, there are few direct measurements of upper crustal permeability, and the vast majority of measurements are based on data from single boreholes (Fisher et al., 2014). A hydrogeologic study using cross-hole data from boreholes separated by 2.2 km, in a direction oblique to strike, found lower apparent permeability compared to that determined from single hole tests in the same region (Fisher et al., 2008). One explanation for this difference is higher permeability in the along-strike direction, but this hypothesis remains to be tested directly.

2.1.4 Study goals

In the present study, we examine the distribution of seafloor heat flux measurements in North Pond to see if spatial correlations exist between nearby heat flux values as a function of their orientation and separation distance. We use numerical simulations to explore how differences in permeability anisotropy could influence the geometry of hydrothermal circulation, the efficiency of advective heat extraction, and patterns of seafloor heat flux. We test multiple forms of permeability anisotropy in the upper ocean crust, as might be created by faulting, cracking, and/or layering of volcanic units. We compare results of coupled flow simulations that include permeability anisotropy having multiple forms (direction, magnitude) to see which best replicate seafloor heat flux observations. Finally, we consider what observations and simulations suggest about the importance of permeability anisotropy to hydrothermal signature of the upper crust of ridge flanks more generally.

2.2 Spatial correlation and numerical simulation of hydrothermal processes

2.2.1 Quantifying spatial correlation of seafloor heat flux across North Pond

Bathymetric data from the region surrounding North Pond are spatially correlated, with differences that depend on azimuth of analysis (Herzfeld, 1993; **Figure 2-1)** While the directionality of bathymetric "grain" is readily apparent from visual inspection (with a dominant regional trend oriented (~N10°E), it is less clear whether heat flux observations in North Pond are similarly correlated. We use a geostatistical technique called variography which is commonly used to quantify the magnitude and direction of spatial correlation of underlying generating processes in geologic and hydrothermal systems

(Anderson and Fairley, 2008; Matheron, 1963). We apply this approach to assess the magnitude and directions of spatial correlation of heat flux data from North Pond.

The semivariance (γ) for a given spatial distance (lag) is defined as:

$$\gamma(h) \ = \frac{1}{2|N(h)|}\sum_{N(h)}(z_i + z_j)^2$$

where h is the lag distance, $N(h)$ the number of unique pairs at lag h, z is the data value (heat flux in this study) at points i and j. Plotting semivariance versus lag (i.e., a variogram) allows determination of the range, or the maximum spatial distance at which points are correlated. We constructed both omnidirectional and directional variograms. An omnidirectional variogram calculates the semivariance between all sets of points while a directional variogram calculates semivariance between points that lie along a specified azimuth, usually a tolerance is applied to capture more data pairs along the azimuth.

To generate variograms of North Pond heat flux data, irregularly spaced observations are declustered to avoid bias towards areas of oversampling (Olea, 2007) and normal score transformed to satisfy assumptions of the geostatistical methodologies used in this analysis (Pyrcz and Deutsch, 2018). To account for this potential sampling bias, we employ a cell-based declustering technique that groups data into cells that minimizes the mean of declustered values (Lindsey et al., 2022). Omni-directional and directional variograms of seafloor heat flux values from North Pond were calculated using normal-score transformed and declustered data, with directional variograms calculated for 15° increments from 0° (north) to 165°. We used a lag distance of 300m and 10 lags for all variograms, as longer total lag distances can't be supported by the heat-flux dataset from North Pond, given the limited spatial distribution of heat flux data.

2.2.2 Simulation of ridge-flank hydrothermal circulation below and around North Pond

2.2.2.1 Numerical simulation code (FEHM)

We simulate coupled fluid and heat transport in the volcanic ocean crust below North Pond with the numerical code, Finite Element Heat and Mass (FEHM), which uses a node-centered, finite-volume representation of storage and transport in porous media (Zyvoloski et al., 2015). FEHM uses a fully implicit solver with variable upstream-downstream weighting to solve conservation of mass and enthalpy, including gravitational potential energy which is necessary for deep bottom water systems (Stauffer et al., 2014). All simulations are run to a “dynamic steady-state” where the stability is achieved when changes in the mass and energy balance between simulated timesteps (≥25 days) are ≤0.01%.

2.2.2.2 Geometry of North Pond simulation domain

Geometry of the simulation domain in this study is the same as used in earlier simulations of North Pond (Price et al., 2022). The simulation domain was constructed with Delaunay meshes of tetrahedral (three-dimensional) cells using the Los Alamos Grid Toolbox (“Los Alamos Grid Toolbox, LaGriT,” 2019). The domain was created based on bathymetric and seismic reflection data that define the geometry of North Pond (e.g., relief of the exposed volcanic crust, sediment thickness, location of sediment pinchouts)

(Schmidt-Schierhorn et al., 2012; **Figure 2-2**). The domain is 95 km along-strike, 45 km across-strike, and 6-7 km thick, with an asymmetric, sediment-filled depression (sediment thickness ≤250 m) near the center. The simulation domain is significantly larger than North Pond so that domain boundaries are placed far from the region of primary interest. The simulation domain consists of sediment, upper volcanic crust (aquifer), and conductive layers that allow for assignment of distinct physical properties to each. Previous studies have treated the thickness of the crustal aquifer layer as a free parameter, but for the current study we use aquifer thickness of 600 m, consistent with earlier simulations and observations from the upper volcanic crust in this area (Becker, 1990; Fisher et al., 2014; Lindsey et al., 2022).

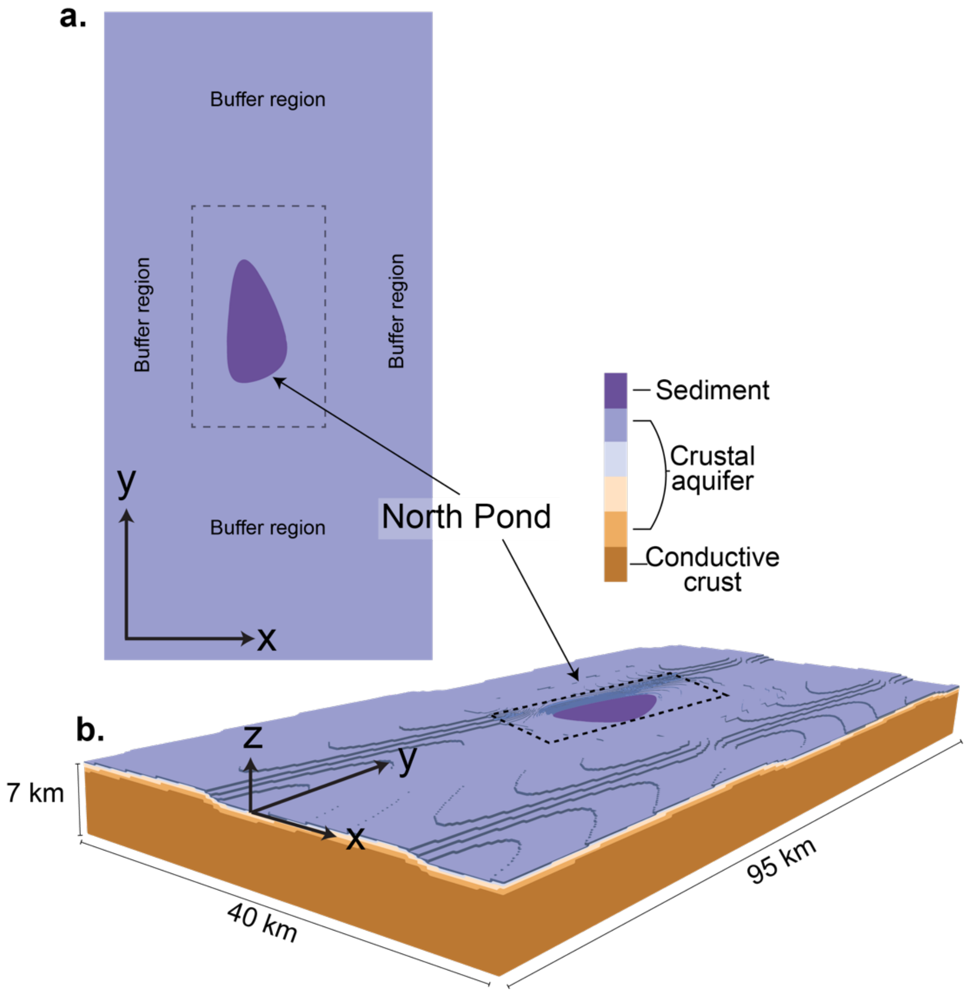

Figure 2-2: Geometry of three-dimensional simulation domain. **A.** Map view of simulation domain. Filled purple polygon is the sedimented surface of North Pond. Arrows show cartesian directions used to represent system geometry and permeability anisotropy. **B.** Perspective view of North Pond simulation domain with dashed box being the area representing North Pond surrounded by buffer regions, crustal layering represented by sediment (purple), crustal aquifer layers (blue, light blue, light orange, orange) and conductive crust (dark orange). Black axis labels denote the nomenclature used in defining permeability for the simulation domain.

Permeability simulations		
Layer	**Permeability orientation**	**Log-Permeability (kx, ky, kz) (m2)**
Crustal aquifer	Isotropic	-9[a]
		-10[a]
	Azimuthal (x-axis)	-9,-10,-10
		-9,-10,-10
		-10,-11,-11
	Azimuthal (y-axis)	-10,-9,-10
		-11,-9,-11
	Planar (x- and y-axes)	-9,-9,-10
		-9,3,-9.3,-10
		-9,-9,-11
	Vertical and azimuthal (y- and z-axes)	-10,-9,-9
		-11,-10,-10
Sediment	Isotropic	-15.4
Conductive crust	Isotropic	-17
Bulk properties		
Layer	**Porosity (-)**	**Thermal conductivity (W/m K)**
Crustal aquifer	0.02 - 0.1	1.8 - 2.0
Sediment	0.62	1.06
Conductive crust	0.01	2.0

[a] Simulations from Price et al. (2022)

Table 2-1: Values of physical properties for permeability anisotropy simulations

2.2.2.3 Domain properties: boundary and initial conditions, bulk properties

Lateral domain boundaries are no-flow for fluid and heat, whereas the bottom boundary is no-flow for fluid and spatially varying heat flux, based on crustal age (Harris and Chapman, 2004). The upper boundary (seafloor) held at a constant temperature (2°C) and pressure corresponding to water depth (~4400 mbsl across North Pond), while remaining free flow for heat and fluid. Pressure and temperature initial conditions for this study were final conditions from earlier simulations that used isotropic permeability (Price et al., 2022). Bulk properties are the same for all simulations in this study (Table 1), including sediment porosity of 62% and thermal conductivity of 1.06 W/m K^{-1} based on core data from North Pond sites U1382-84 (Edwards et al., 2012). Basement rocks porosity and thermal conductivity are set based on core data from North Pond and other crustal sites (Becker et al., 2001; Fisher et al., 2014); rock porosities are 1 to 10%, and thermal conductivities are 1.8 to 2.0 W/m-K (**Table 2-1**).

2.2.2.4 Permeability anisotropy in the upper crustal aquifer

We assign anisotropic permeability to crustal aquifer layers beneath North Pond in the x (across-strike), y (along-strike), and z (vertical) axis. We test for different orientations of permeability anisotropy: (1) aligned with x-axis, (2) aligned with y-axis, (3) aligned with the x-y-plane, and (4) aligned with the y-z-plane. Each of these orientations corresponds to a representation of one or more geological processes that could result in permeability anisotropy. For example, elevated permeability in the x-y plane (horizontal) could result from crustal construction in well-defined layers, whereas elevated permeability in a y-z (vertical) plane could result from faulting and/or a pervasive crustal fabric that runs parallel to MAR orientation (**Figure 2-1**). Preferential crustal fabric could also contribute to elevated permeability mainly in x-axis or y-axis directions, as could the intersection of planar fabrics (e.g., layering/faulting along x-y and y-z planes could result in elevated permeability particularly along the y-axis).Values of crustal permeability are assigned on the basis of packer tests and borehole logs and tests from North Pond and elsewhere (Becker, 1990; Fisher et al., 2014; Langseth et al., 1984; Wheat et al., 2020), and earlier simulations of North Pond (Price et al., 2022). For each of these permeability anisotropy orientations, we vary the directional contrast in permeability by 0.5, 1, and 2 orders of magnitude (**Table 2-1**).

2.3 Evidence for anisotropy from variograms of heat flux and simulations of coupled fluid-heat transport

2.3.1 Variography of seafloor heat flux measurements in North Pond

Omnidirectional variograms suggest that heat flux observations taken from North Pond are correlated to a distance of ~1700 m strictly based on where the variance crosses the sill (**Figure 2-3b**). Directional variograms show a clear azimuthal correlation between heat flux observations. The azimuth of maximum correlation is along N15ºE, consistent with the general trend of bathymetric relief around North Pond (**Figure 2-1a**). The directional variogram for the maximum correlation azimuth never reaches the sill along N15ºE. The directional variogram for the minimum correlation azimuth (N75ºW) reaches the sill at a range ~250 m. The azimuth of maximum correlation aligns with the regional strike of bathymetric data determined from a regional study of data from the western flank of the MAR (Herzfeld, 1993). The spatial analysis of heat flux data shows that there is a preferred orientation of correlation that runs parallel to the fabric volcanic crust, suggesting that anisotropy in crustal permeability could be influencing patterns of seafloor hydrothermal circulation in the upper volcanic crust below North Pond.

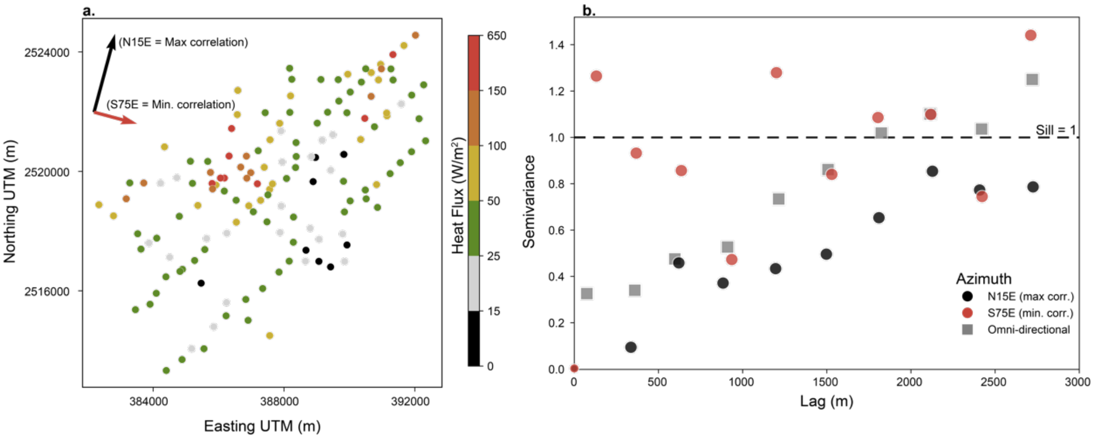

Figure 2-3: Spatial distribution of heat flux and variogram from heat flux data. **A.** Seafloor heat flux observations from North Pond (Langseth et al., 1992; Schmidt-Schierhorn et al., 2012) plotted in UTM coordinates (meters). Orientation of azimuths of maximum correlation (N15°E) in black and minimum correlation (S75°E) in red, as determined from variography. **B.** Variography of heat flux illustrating isotropic variogram (dotted gray line, filled squares), directional variogram at maximum correlation azimuth of N15°E (solid black line, filled circles), and directional variogram at minimum correlation azimuth of S75°E (red dashed line, filled circles). Horizontal gray line at semi-variance (λ) = 1 indicates the sill.

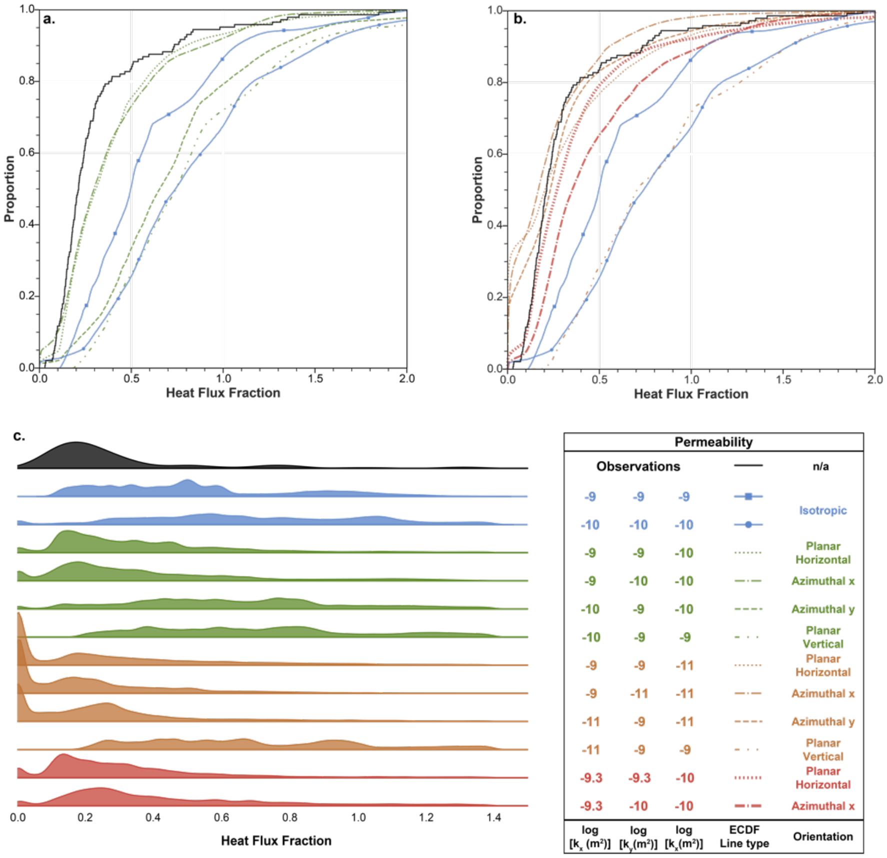

Figure 2-4: Empirical cumulative distribution functions (ECDF) and ridge plots of observed and simulated heat flux fraction through North Pond sediments (hfout / hfin). A. ECDF of observed (solid black line) and simulated heat flux fraction for isotropic (solid blue lines) and anisotropic with 1-order of magnitude of contrast in permeability (green lines). B. ECDF of observed (solid black line) and simulated heat flux fractions for isotropic (solid blue lines) and anisotropic with 0.5-order of magnitude of contrast in permeability (red lines), and anisotropic with 2-order of magnitude of contrast in permeability (orange lines). Each line type in the ECDF represents separate orientations of increased permeability in the x-y plane (dotted), x-axis (dash-dot-dash), y-axis (dashed), and x-z plane (dash-dot-dot). C. Ridge plots of observed (black) and simulated [isotropic (blue) and anisotropic 1-order of magnitude of permeability contrast (green), 2-order of magnitude of permeability contrast (orange), and 0.5-order of magnitude permeability contrast (red) simulations of heat flux fraction.

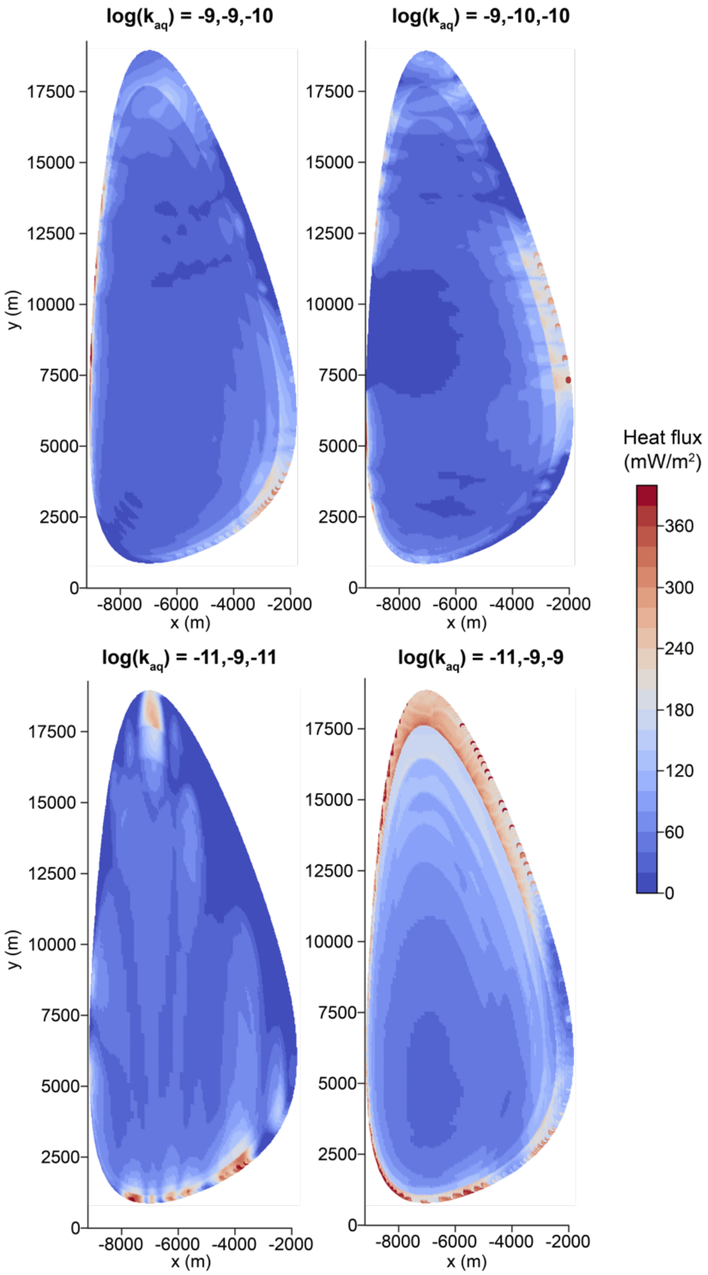

Figure 2-5: Heat maps of simulated heat fluxes through North Pond sediments. Heat maps are faceted by permeability orientation and colored by warmer colors representing higher heat fluxes and cooler colors representing lower heat flux values. Heat fluxes are reported in mW/m^2. X and Y values correspond to simulation domain coordinates.

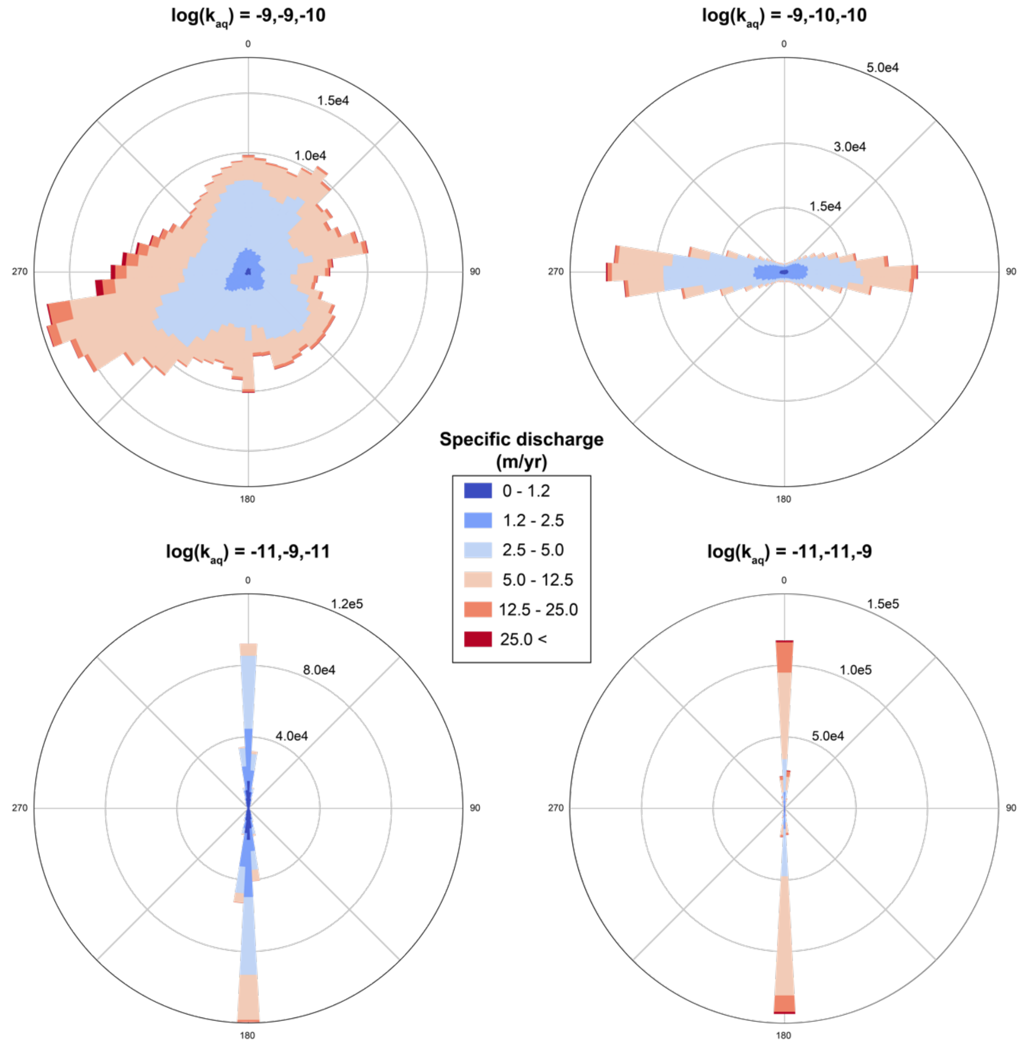

Figure 2-6: Rose diagrams of specific discharge for selected anisotropic simulations of North Pond (corresponding to the four plots shown in Fig. 5), using data from the crustal aquifer that is beneath the sediment. Rose diagrams are faceted by permeability orientation and binned by azimuth 6° bins. Y-axis (or radial scales) differ to better visualize the directional distribution of specific discharge.

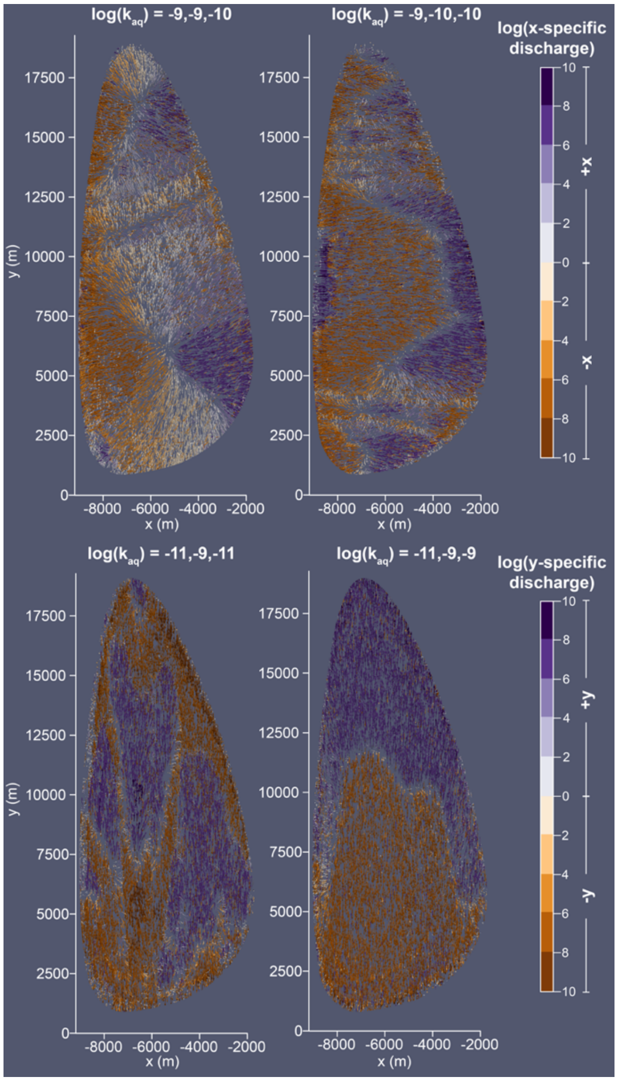

Figure 2-7: Vector plots of fluid flow patterns in the volcanic crustal aquifer below North Pond sediments. Vector plots are faceted by permeability orientation. Specific discharge vectors are colored by the x-component of specific discharge vectors for the top row of vector plots and the y-component of specific discharge vectors for the bottom row of vector plots. Vectors are log-scaled by the highest specific discharge value for each simulation. X and Y values correspond to simulation domain coordinates.

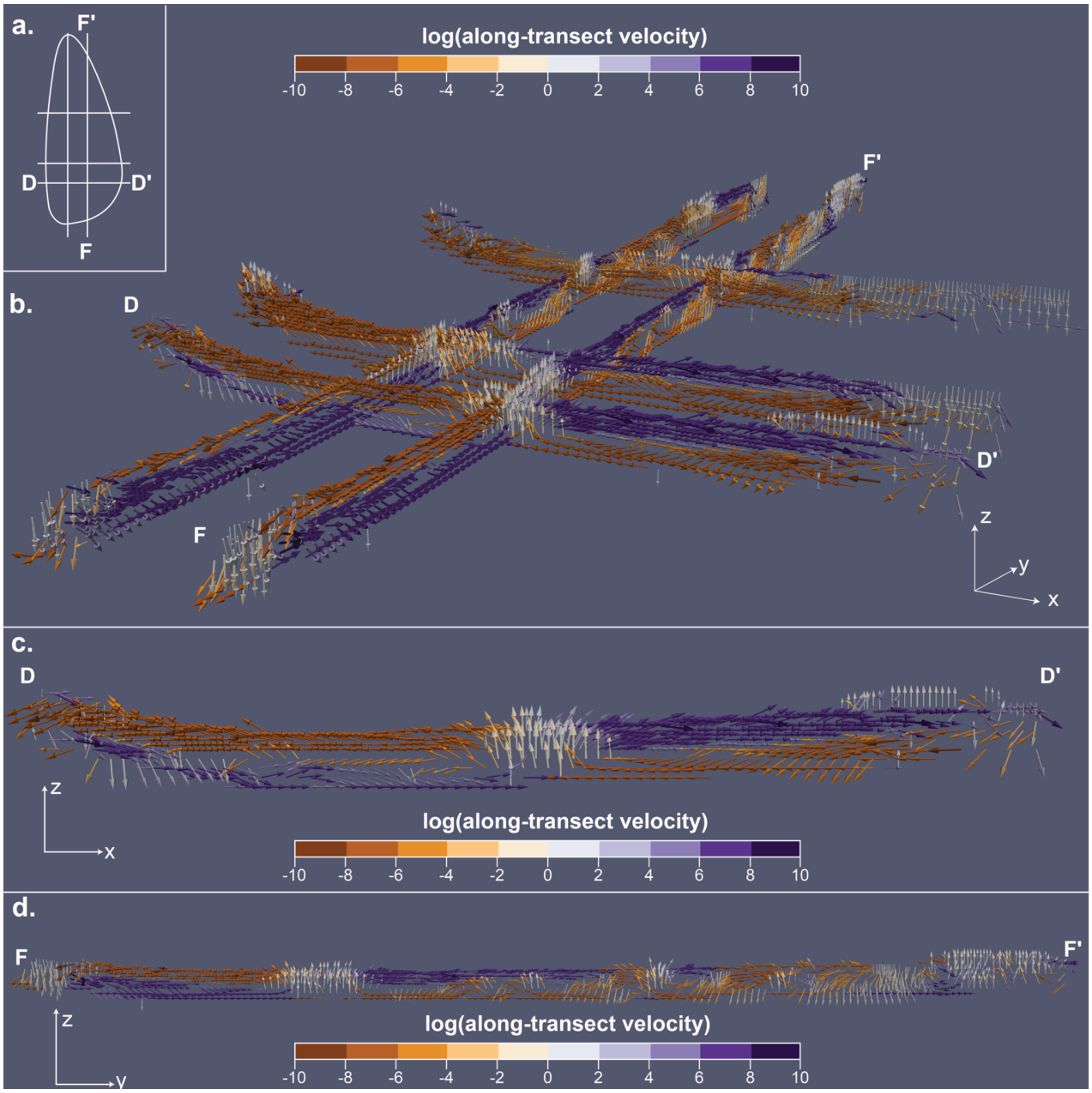

Figure 2-8: Vector plots of cross-sections of North Pond for simulated specific discharges of aquifer permeability loq[k_{aq}] = -9, -9, -10. **A.** Locations of specific discharge transects overlain on North Pond simulation domain **b.** Vector fence diagram of along-strike and across-strike fluid fluxes. **C.** Vector cross-section of D-D′ (parallel to x-axis or across-strike). **D.** Vector cross-section of F-F′ (parallel to y-axis or along-strike). All vectors are colored and log-scaled by along-transect fluid specific discharge.

2.3.2 Coupled simulations using isotropic and anisotropic permeability

Previous studies of coupled fluid and heat fluxes beneath North Pond utilized isotropic permeability distributions within the crustal aquifer (Price et al., 2022). Simulations with isotropic permeability of $k_{aq} = 10^{-9}$ m^2 resulted in mean conductive heat flux through the sedimented pond that was ~50% of lithospheric input. Observations indicate that heat-flux values are ~20% of lithospheric, so an additional ~30% of lithospheric heat must be removed advectively. Isotropic simulations with somewhat lower permeability in the upper volcanic crust ($k_{aq} = 10^{-10}$ m^2) more closely matched observed heat flux variability with higher and lower heat flux values in close proximity, particularly around the western and northern margins of North Pond. Flow geometries associated with isotropic simulations showed a preference for across-strike transport, although this net transport below North Pond was slowed somewhat by local (secondary) small-scale convection and mining of heat from the deeper crust across a larger region, limiting the efficiency of heat extraction (Price et al., 2022).

New simulations with azimuthal permeability anisotropy, either in the x- or y-axis only, result in significant differences in simulated heat fluxes through North Pond sediments (**Figure 2-4**). Simulated heat flux values based on this orientation of permeability anisotropy are closer to observations (i.e., ~20% of lithospheric heat input) but there are important differences depending on the magnitude of the permeability contrast. Simulations with azimuthal permeability anisotropy that produce the closest match to observations have elevated permeability in the x-axis direction, with a contrast of 1 order of magnitude ($k_{aq\text{-}x} = 10^{-9}$ m^2; $k_{aq\text{-}y} = k_{aq\text{-}z} = 10^{-10}$ m^2) or a contrast of 0.5 order of magnitude ($k_{aq\text{-}x} = 10^{-9.3}$ m^2; $k_{aq\text{-}y} = k_{aq\text{-}z} = 10^{-10}$ m^2) (Figure 4). The former results in a particularly good match to the empirical cumulative distribution function of observations at the upper end of the distribution, where heat flux is elevated above the lithospheric value (**Figure 2-4**). When the same direction of permeability anisotropy is simulated but with a 0.5 order of magnitude directional contrast, simulated heat extraction is less efficient. Increasing the permeability contrast to 2 orders of magnitude contrast ($k_{\text{aq-x}} = 10^{-9}$ m^2; $k_{\text{aq-y}} = k_{\text{aq-z}} = 10^{-11}$ m^2) removed too much heat around the margin of North Pond, making the simulation inconsistent with observations. Elevating permeability along only the y-axis ($k_{\text{aq-y}} = 10^{-9}$ m^2; $k_{\text{aq-y}} = k_{\text{aq-z}} = 10^{-10}$ m^2) results in less efficient advective extraction of heat and a poorer match to the distribution of observations. When this form of anisotropy is increased to a contrast of 2 orders of magnitude contrast ($k_{\text{aq-y}} = 10^{-9}$ m^2 and $k_{\text{aq-y}} = k_{\text{aq-z}} = 10^{-11}$ m^2), too much heat is extracted around the pond margins, as occurred with azimuthal permeability anisotropy along the x-axis (**Figures 2-4b and 2-4c**).

For simulations with a single direction of azimuthal anisotropy, a permeability contrast of 1 order of magnitude generates a better match to heat flux data than do similar simulations with a permeability contrast of 0.5 to 2 orders of magnitude. Simulations with a permeability contrast of 2 orders of magnitude result in greater continuity (or streaks) of higher and lower heat flux values oriented in the higher-permeability direction (**Figure 2-5**), which is consistent with geostatistical analysis (**Figure 2-3b**) and the general trend of the crustal fabric (**Figure 2-1**). However, this results in large areas along the margin of North Pond having heat flux <10% of lithospheric. Rose diagrams (**Figure 2-6**) and vector plots (**Figure 2-7**) of specific discharge from simulations with a single direction of azimuthal anisotropy illustrate the extent to which fluid flows are impacted by the imposition of permeability anisotropy. Unsurprisingly, fluid fluxes in simulations with azimuthal permeability anisotropy tend to align parallel to the direction of highest permeability, with very little flow in the orthogonal direction (**Figure 2-7**).

To our surprise, simulations with permeability anisotropy in a vertical plane oriented along the long axis of North Pond result in advective removal of very little lithospheric heat in comparison to all other anisotropic permeability simulations (**Figure 2-4**). The efficiently of heat extraction in these simulations, incorporating a range of permeability contrasts (1-2), is little different from that seen in earlier simulations with isotropic permeability (Price et al., 2022). These simulations also result in large patches of elevated heat flux along the northern and southern edges of North Pond, and areas of suppressed heat flux along the eastern and western margins of the basin. In addition, simulations with planar vertical anisotropy result in preferential flow along the y-z plane, including secondary convection cells, and this tends to suppress local variability in seafloor heat flux. Observational data are not consistent with this pattern exhibiting more local variability than these simulations predict indicating more efficient heat extraction overall.

Simulations with elevated permeability in the horizontal plane (higher $k_{\text{aq-x}}$ and $k_{\text{aq-y}}$ compared to $k_{\text{aq-z}}$) result in the best match to seafloor heat flux observations (**Figures 2-4 and 2-5**). In these simulations with planar permeability elevated by 0.5 or 1 order of magnitude relative to vertical permeability, the magnitude and distribution of seafloor heat flux values comprise a better match to observations than those from earlier simulations using isotropic permeability (Price et al., 2022), with a mode near 10-30% of lithospheric and considerable small-scale variability. In addition, simulations with horizontal anisotropy do not result in excessive areas of very low heat flux that were apparent for simulations having a single direction of elevated permeability. However, when $k_{aq\text{-}x}$ and $k_{aq\text{-}y}$ are elevated compared to $k_{aq\text{-}z}$ by 2 orders of magnitude, heat extraction becomes too efficient, and large areas of very low heat flux develop around the margins of the simulated sediment pond (**Figure 2-4**). Fluid flow patterns in simulations with higher planar permeability indicate more variability and complexity both along and across strike compared to other forms of permeability anisotropy. Across- and along-strike flows are more evenly distributed and contribute more equally to the overall flow geometry (**Figures 2-6 and 2-7**). Even though lateral heat extraction is enhanced in these simulations compared to equivalent simulations with isotropic permeability, anisotropic simulations still include small-scale convection that forms in along-strike and across-strike orientations (**Figure 2-8**) with a strong central plume below the deepest part of North Pond, and smaller convection cells and rolls that form around the edges of the basin. In summary, of the anisotropic permeability simulations, those with moderate elevation in horizontal permeability seems to promote the best balance in extracting the correct amount of lithospheric heat and fostering local variations in seafloor heat flux through North Pond sediments. Simulations with other forms of permeability anisotropy, and with larger or no directional contrast in permeability, tend to generate a poorer match to observations.

2.4. Evidence of Anisotropy in Crustal Permeability

2.4.1 Heat transport and extraction from the crust below North Pond

Earlier hydrogeologic simulations of North Pond using isotropic permeability in the volcanic crust helped explain some of the observed heat flux deficit and replicated small-scale heat-flux variability measured at the seafloor (Price et al., 2022). These simulations also showed that fluid flow patterns in the upper crust are more complex than the single-pass, unidirectional system hypothesized in earlier studies, with mixed convection superimposed on rapid lateral flow and time-varying deviations in fluid temperature and pressure in the upper crust. However, no single isotropic simulation was able to match both the magnitude and spatial distribution of heat flux observations. Instead, lower aquifer permeabilities $k_{aq}= 10^{-10}$ m^2 more closely matched the spatial distribution of high and low heat flux values, while the highest permeabilities simulated $k_{aq}= 10^{-9}$ m^2 more closely matched the overall distribution of heat flux observations (**Figure 2-4**). Elevating isotropic permeability did not sufficiently reduce seafloor heat flux at North Pond because increasingly vigorous, secondary convection in the upper crust extracted more heat from a larger areal region of the deeper crust and throttled and decreased the efficiency of the lateral transport of fluids from beneath the sedimented pond.

Including permeability anisotropy in hydrothermal simulations of North Pond in the present study helps to address these limitations, but in unexpected ways. Given the strong ridge-parallel structural fabric apparent in regional bathymetry around North Pond (**Figure 2-1**), including large-offset normal faults bounding abyssal hills and variograms of seafloor heat flux that indicate the strongest continuity in the along-strike direction

(**Figure 2-3**), we expected that simulations using anisotropic permeability, with higher values associated with along-strike faults and cracks oriented in the y-z plane ($k_{aq\text{-}y}$ and $k_{aq\text{-}z} > k_{aq\text{-}x}$), might yield a better match between simulated and observed heat flux patterns. Instead, we found that simulations with elevated horizontal permeability ($k_{aq\text{-}x}$ and $k_{aq\text{-}y} > k_{aq\text{-}z}$) provide a better combination of efficient regional heat extraction and local heat-flux variability. In addition, the magnitude of permeability anisotropy that best matches heat flux observations is moderate, with $k_{aq\text{-}x}$ and $k_{aq\text{-}y}$ elevated by 0.5 to 1 order of magnitude relative to $k_{aq\text{-}z}$.

Horizontal layering in volcanic construction of the upper crust (Bartetzko et al., 2001; Chadwick et al., 2001; Karson, 2002) could favor lateral continuity in permeable deposits of pillows, rubble, and breccia, with more massive and extensive basalt flows helping to isolate relatively thin crustal intervals (**Figure 2-9a**). In contrast, high-angle faulting like that associated with abyssal hill topography and smaller scale fractures and cracks (Harris et al., 2017; Macdonald et al., 1996) could enhance fluid flow and advective heat transport subparallel to the seafloor spreading center that produced the crust, including subvertical convection cells oriented along strike (**Figure 2-9b**). However, neither of these explanations appears to be solely responsible for patterns of hydrothermal circulation and heat transfer in the volcanic crust below North Pond.

Instead, patterns of fluid flow, heat redistribution and extraction below and around North Pond seem to be emergent phenomena, resulting from interactions between the anisotropic character of the volcanic upper crust and the geometry and scale of the bathymetric depression of North Pond (**Figure 2-9c**). The disparity in the dimensions of North Pond in the along-strike and across-strike directions seems to favor a component of

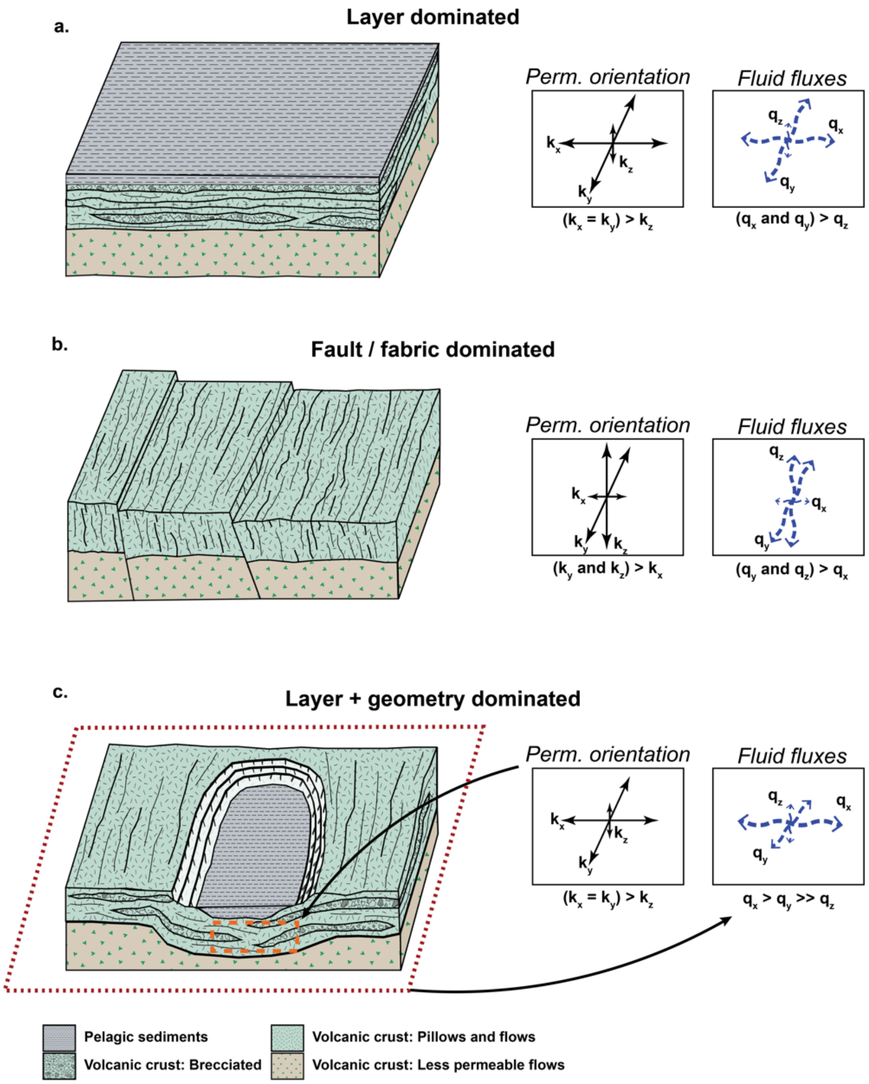

Figure 2-9: Conceptual diagrams of crustal factors that could result in permeability anisotropy and/or preferential fluid flow directions. **A.** Crustal layering with limited horizontal continuity of the most permeable regions. **B.** High-angle faults and cracks associated with crustal subparallel to orientation of the spreading ridge at which crust was formed. **C.** Layering and geometry of a sediment pond resulting in a preferential flow direction.

across-strike flow, but not as strong as seen when $k_{\text{aq-x}}$ alone is elevated (**Figure 2-6**). Given the formation of a central convection cell below North Pond, with a rising plume below the thickest sediment (**Figure 2-8**), there is a shorter path between inflow and outflow, and a steeper sloping contact at the sediment-basement interface, in the across-strike direction compared to the along-strike direction. These geometric characteristics and the contrast in properties between the volcanic upper crust and overlying sediments, coupled with the permeability anisotropy intrinsic to layering of the upper crustal aquifer, combine to produce the complex hydrogeologic character observed at North Pond. In the surrounding region where there is no conductive boundary layer at the top of volcanic basement (sediment), we expect that permeability anisotropy of the upper crustal aquifer may play a stronger role in determining hydrothermal flow patterns.

2.4.2 Broader implications of permeability anisotropy in the ocean crust for ridge-flank hydrothermal circulation.

While direct measurements are scarce, there is abundant, often indirect, evidence for permeability anisotropy on ridge flanks in the upper ocean crust. The most fundamental evidence is layering, as seen in crustal boreholes, the walls of fracture zones and tectonic windows, and ophiolites. Seafloor spreading is discontinuous in both space and time, leading to heterogeneous layering of rock units as different magmatic, tectonic, and alteration processes occur at spreading centers and as the crust subsequently evolves, leading to widely varying physical properties with depth at scales of centimeters to hundreds of meters (Bartetzko et al., 2001; Gillis and Robinson, 1988; Karson, 2002). There are relatively few studies of the permeability and lithostratigraphy within nearby upper crustal holes in the ocean crust, and these mainly show consistent permeability values, with lateral continuity of layers and alteration demonstrated mainly in the along-strike direction (Alt et al., 1996; Becker et al., 2013).

Two-dimensional numerical simulations of the southern flank of the Costa Rica Rift that incorporated layering were better able to replicate the extent of lateral heat transport associated with ridge-flank circulation compared with simulations that lacked layering (Fisher et al., 1994), and higher resolution simulations resulted in the formation of small-scale convection cells that were less efficient in moving heat laterally (Fisher and Becker, 1995). Similar results were obtained for simulations of the eastern flank of the Juan de Fuca Ridge (Stein and Fisher, 2001), with rapid lateral flow efficiently mining heat from depth, provided small-scale local mixing was suppressed. Given that seafloor heat flux is a powerful tracer of underlying advection in the volcanic crust, the occurrence of large regions within which heat flux is well below lithospheric values (Davis et al., 1992; Hutnak et al., 2008; Langseth et al., 1992) is powerful evidence for rapid lateral flow, which is both faster and more efficient at mining heat when horizontal permeability is elevated and secondary mixing is limited.

Evidence for azimuthal anisotropy in the upper ocean crust based on seismic velocities (Detrick et al., 1998; Fryer et al., 1989; Stephen, 1981) could be associated with permeability anisotropy if the same crustal fabric were responsible, but a global consideration of crustal evolution suggests that elevated permeability is retained long after alteration processes leading to increased seismic velocities are essentially complete (Anderson et al., 2012; Fisher and Becker, 2000). A comparison of permeability values calculated from cross-hole pressure response and single-hole permeability measurements may be explained by elevated along-strike permeability (Fisher et al., 2008). In general, crustal faults that carry fluids are expected to enhance flow in the along-strike direction, both within faults and in the surrounding damaged zones, but may also lead to lower permeability in the cross-strike direction (Caine et al., 1996; López and Smith, 1996).

We infer from earlier work and new results from the present study that anisotropy in the advective extraction of lithospheric heat may not be determined by a single set of crustal parameters. Ultimately, anisotropy in ridge-flank hydrogeology appears to be an emergent property, one that develops as a consequence of multiple processes and conditions, including layering, faulting, and interactions with components like seafloor relief and a patchy conductive boundary layer at the seafloor. There may be no single explanation for the pattern of subseafloor fluid and heat transport below and around North Pond, and for the associated pattern of seafloor heat flux. If we think about ridge-flank circulation more broadly, including areas like North Pond (where basement exposure at the seafloor is common) and the eastern flank of the Juan de Fuca Ridge (where basement exposure is limited to a few outcrops across a large area), crustal anisotropy may have developed across multiple phases of construction and tectonism, and may therefore be a common feature, but for different reasons in different settings. The form of permeability anisotropy that appears to be most critical in determining the nature of ridge-flank hydrogeology at multiple sites appears to be associated with fundamental (constructional) crustal layering. This layering simultaneously favors rapid lateral flow in the crust and suppresses the formation of small convection cells that would serve to reduce the efficiency of heat extraction. How hydrothermal flows are influenced by permeability anisotropy may vary greatly depending on local conditions, including the causes and nature of basement relief and the extent of sediment cover (**Figure 2-9**). It appears in the case of North Pond that along-strike flow may be modestly favored (based on spatial analysis of seafloor heat flux values, **Figure 2-3**), but it can't be too strongly favored without causing a mismatch between the measured and simulated extent of advective heat extraction (**Figure 2-4**). Azimuthal anisotropy may be more strongly favored in settings where the direct connection between volcanic crustal rocks and the overlying ocean is more limited, like the eastern flank of the Juan de Fuca Ridge.

Given that permeability anisotropy may be best considered to be a consequence of crustal conditions, next steps in the simulation of ridge-flank hydrothermal systems should consider explicit representation of crustal heterogeneity (Frippiat and Holeyman, 2008; Schulze-Makuch et al., 1999). Seafloor heat flux data may provide limited constraints on more complex representations of permeability in the crust, because thermal conductivity is relatively high but results of recent solute tracer tests in the ocean crust may prove more sensitive (Neira et al., 2016; Wheat et al., 2020). The detailed scales of spatial variability in bulk properties are not well defined for most of the ocean crust, except vertically in isolated boreholes, but the few studies that have examined kilometer-scale variability (Alt et al., 1996; Becker et al., 2013) could help for setting upper limits on the lateral extent of continuity of key units. More detailed simulations would allow inclusion and comparison of structures that could be combined to result in anisotropic behavior, including primary crustal layering, differential alteration, and faulting. Importantly, the next generation of models can provide testable hypotheses that are ready to be assessed through carefully placed boreholes used to recover crustal rocks and make direct in-situ measurements of formation properties.

2.5. Summary and conclusions

Seafloor heat flux observations from North Pond sediments are azimuthally correlated in the along-strike direction, consistent with regional bathymetry. This suggests that there could be a preference for fluid flow in the along-strike direction as well. Numerical simulations that incorporate permeability anisotropy in the volcanic crust below North Pond improve the match between observed and simulated heat flux compared to simulations using isotropic permeability in the upper crust. Interestingly, the correlation between simulated and observed heat flux is improved most with simulations having planar anisotropic permeability, representative of crustal layering, instead of permeability anisotropy along a single azimuth or along a vertical plane running parallel to the crustal fabric.

Within the volcanic crust below North Pond, the efficient extraction of lithospheric heat is facilitated not simply by increasing permeability overall, but rather by having: (a) a contrast between horizontal and vertical permeability, and (b) an asymmetric sediment pond with a long-axis oriented sub-parallel to the trend of the crustal fabric. The permeability contrast associated with crustal layering helps to enhance the advective extraction of lithospheric heat by limiting the extent of secondary mixing, and lateral gradients associated with the shape of North Pond and the contrast between rock and sediment properties help to drive a mixture of along-strike and across-strike flow. Therefore, permeability anisotropy and geometry of the sediment-basement interface below North Pond combine to produce the emergent characteristics of fluid and heat transport in the crustal aquifer

There is no reason to expect that the upper crust below and around North Pond is anomalous compared to other ridge-flank sites. Site-specific conditions like spreading rate, sediment thickness and continuity, and off-axis volcanism are important, but global mechanisms of ocean crustal construction and tectonic modification should apply more broadly. Permeability anisotropy associated with crustal layering seems to be important in multiple ridge-flank settings for helping to explain patterns of advective heat transport. The mediating factor that permeability anisotropy imposes on the connectivity of the crustal aquifer with the overlying ocean is important for determining the overall hydrogeologic characteristics of a ridge-flank hydrothermal system. However, ridge-flank systems where connection of the overlying ocean to the volcanic aquifer is limited, the degree to which and how much layered permeability anisotropy affects the hydrothermal character in these systems is unclear.

Understanding the nature, causes, and implications of permeability anisotropy for ridge-flank hydrogeology with greater confidence will require exploration and simulation of these systems at higher resolution. Direct testing is needed using borehole networks to resolve directly the nature of connections at different levels in the upper crust and laterally in different directions. Future investigations of ridge-flank systems should incorporate permeability anisotropy of multiple forms, in addition to crustal characteristics such as heterogeneity, faults, and the extent of lateral continuity of crustal layers. Simulating water-rock reactions and microbial processes within these systems will require even more detailed representations of permeable channel networks, including their geometries, surface areas, and other factors controlling the evolution of ridge-flank fluids and crustal rocks.

Acknowledgments

This chapter reflects a manuscript in preparation with the following coauthors: Andrew T. Fisher, Cary R. Lindsey, Philip H. Stauffer, and Carl W. Gable.

This research was supported by National Science Foundation grants OIA-0939564 and OCE-1924384 and was motivated and inspired by numerous observations and experiments conducted by researchers who are part of the Center for Dark Energy Biosphere Investigations (C-DEBI) and the Integrated Ocean Drilling Program and its predecessors. Philip Stauffer is supported by Los Alamos National Laboratory which is operated by Triad National Security for the National Nuclear Security Administration of the USDOE (Contract no. 89233218CNA000001).

Data Availability Statement

Data sets for this research are available in the DRYAD data repository at https://datadryad.org/stash/share/D3ujn-wbsLKbFzE8lMsLPed9ZpHbi01ii4P4XzwVYfo and https://doi.org/10.7291/D1G67P

References

Alt, J.C., Teagle, D.A.H., Laverne, C., Bach, W., Honnorez, J., Becker, K., Ayadi, M., Pezard, P.A.,1996. Ridge-Flank Alteration of Upper Ocean Crust in the Eastern Pacific: Synthesis of Results for Volcanic Rocks of Holes 504B and 896A, in: Alt, J.C., Kinoshita, H., Stokking, L.B., Michael, P.J. (Eds.), Proceedings of the Ocean Drilling Program, 148 Scientific Results, Proceedings of the Ocean Drilling Program. Ocean Drilling Program. https://doi.org/10.2973/odp.proc.sr.148.150.1996

Anderson, B.W., Coogan, L.A., Gillis, K.M., 2012. The role of outcrop-to-outcrop fluid flow in off-axis oceanic hydrothermal systems under abyssal sedimentation conditions: OUTCROP-TO-OUTCROP FLUID FLOW. J. Geophys. Res. 117, n/a-n/a. https://doi.org/10.1029/2011JB009052

Anderson, T.R., Fairley, J.P., 2008. Relating permeability to the structural setting of a fault-controlled hydrothermal system in southeast Oregon, USA. J. Geophys. Res. 113, B05402. https://doi.org/10.1029/2007JB004962

Bartetzko, A., Pezard, P., Goldberg, D., Sun, Y.-F., Becker, K., 2001. Volcanic stratigraphy of DSDP/ODP Hole 395A: An interpretation using well-logging data. Marine Geophysical Researches 22, 111–127. https://doi.org/10.1023/A:1010359128574

Becker, K., 1990. Measurements of the permeability of the upper oceanic crust at Hole 395A, ODP Leg 109, in: Detrick, R., Honnorez, J., Bryan, W.B., Juteau, T., et al., Proc. ODP, Sci. Results, 106/109. College Station, TX, pp. 213–222.

Becker, K., Bazrtetzko, A., Davis, E.E. (Eds.), 2001. Leg 174B Synopsis: Revisiting Hole 395A for logging and long-term monitoring of off-axis hydrothermal processes in young oceanic crust., in: Proceedings of the Ocean Drilling Program, 174B Scientific Results. Ocean Drilling Program. https://doi.org/10.2973/odp.proc.sr.174B.2001

Becker, K., Fisher, A.T., Tsuji, T., 2013. New packer experiments and borehole logs in upper oceanic crust: Evidence for ridge-parallel consistency in crustal hydrogeological properties. Geochemistry, Geophysics, Geosystems 14, 2900–2915. https://doi.org/10.1002/ggge.20201

Becker, K., Wheat, C.G., Villinger, H., Davis, E., 2022. Long-Term Observations of Subseafloor Temperatures and Pressures in a Low-Temperature, Off-axis Hydrothermal System in North Pond on the Western Flank of the Mid-Atlantic Ridge, *Geochemistry, Geophysics, Geosystems*. https://doi.org/10.1029/2022GC010496

Caine, J.S., Evans, J.P., Forster, C.B., 1996. Fault zone architecture and permeability structure. Geol 24, 1025. https://doi.org/10.1130/0091-7613(1996)024<1025:FZAAPS>2.3.CO;2

Chadwick, W.W., Scheirer, D.S., Embley, R.W., Johnson, H.P., 2001. High-resolution bathymetric surveys using scanning sonars: Lava flow morphology, hydrothermal vents, and geologic structure at recent eruption sites on the Juan de Fuca Ridge. J. Geophys. Res. 106, 16075–16099. https://doi.org/10.1029/2001JB000297

Davis, E.E., Chapman, D.S., Mottl, M.J., Bentkowski, W.J., Dadey, K., Forster, C., Harris, R., Nagihara, S., Rohr, K., Wheat, G., Whiticar, M., 1992. FlankFlux: an experiment to study the nature of hydrothermal circulation in young oceanic crust. Can. J. Earth Sci. 29, 925–952. https://doi.org/10.1139/e92-078

Delaney, J.R., Kelley, D.S., Lilley, M.D., Butterfield, D.A., Baross, J.A., Wilcock, W.S.D., Embley, R.W., Summit, M., 1998. The Quantum Event of Oceanic Crustal Accretion: Impacts of Diking at Mid-Ocean Ridges. Science 281, 222–230. https://doi.org/10.1126/science.281.5374.222

Detrick, R.S., Toomey, D.R., Collins, J.A., 1998. Three-dimensional upper crustal heterogeneity and anisotropy around Hole 504B from seismic tomography. J. Geophys. Res. 103, 30485–30504. https://doi.org/10.1029/98JB02409

Edwards, K.J., Bach, W., Klaus, A., the Expedition 336 Scientists, 2012. Proceedings of the Integrated Ocean Drilling Program Volume 336 Expedition Reports. Integrated Ocean Drilling Program Management International, Inc., Toyko.

Fisher, A.T., Alt, J., Bach, W., 2014. Hydrogeologic Properties, Processes, and Alteration in the Igneous Ocean Crust, in: Stein, R., Blackman, D.K., Inagaki, F., Larsen, H.-C. (Eds.), Developments in Marine Geology, Earth and Life Processes Discovered from Subseafloor Environments. Elsevier, pp. 507–551. https://doi.org/10.1016/B978-0-444-62617-2.00018-9

Fisher, A.T., Becker, K., 2000. Channelized fluid flow in oceanic crust reconciles heat-flow and permeability data. Nature 403, 71–74. https://doi.org/10.1038/47463

Fisher, A.T., Becker, K., 1995. Correlation between seafloor heat flow and basement relief: Observational and numerical examples and implications for upper crustal permeability. J. Geophys. Res. 100, 12641–12657. https://doi.org/10.1029/95JB00315

Fisher, A.T., Becker, K., Narasimhan, T.N., 1994. Off-axis hydrothermal circulation: Parametric tests of a refined model of processes at Deep Sea Drilling Project/Ocean Drilling Program site 504. Journal of Geophysical Research: Solid Earth 99, 3097–3121. https://doi.org/10.1029/93JB02741

Fisher, A.T., Davis, E.E., Becker, K., 2008. Borehole-to-borehole hydrologic response across 2.4 km in the upper oceanic crust: Implications for crustal-scale properties. Journal of Geophysical Research: Solid Earth 113. https://doi.org/10.1029/2007JB005447

Fisher, A.T., Davis, E.E., Hutnak, M., Spiess, V., Zühlsdorff, L., Cherkaoui, A., Christiansen, L., Edwards, K., Macdonald, R., Villinger, H., Mottl, M.J., Wheat, C.G., Becker, K., 2003. Hydrothermal recharge and discharge across 50 km guided by seamounts on a young ridge flank. Nature 421, 618–621. https://doi.org/10.1038/nature01352

Frippiat, C.C., Holeyman, A.E., 2008. A comparative review of upscaling methods for solute transport in heterogeneous porous media. Journal of Hydrology 362, 150–176. https://doi.org/10.1016/j.jhydrol.2008.08.015

Fryer, G.J., Miller, D.J., Berge, P.A., 1989. Seismic Anisotropy and Age-Dependent Structure of the Upper Oceanic Crust, in: Evolution of Mid Ocean Ridges. American Geophysical Union (AGU), pp. 1–8. https://doi.org/10.1029/GM057p0001

Giambalvo, E.R., Steefel, C.I., Fisher, A.T., Rosenberg, N.D., Wheat, C.G., 2002. Effect of fluid-sediment reaction on hydrothermal fluxes of major elements, eastern flank of the Juan de Fuca Ridge. Geochimica et Cosmochimica Acta 66, 1739–1757. https://doi.org/10.1016/S0016-7037(01)00878-X

Gillis, K.M., Robinson, P.T., 1988. Distribution of alteration zones in the upper oceanic crust. Geol 16, 262. https://doi.org/10.1130/0091-7613(1988)016<0262:DOAZIT>2.3.CO;2

Harris, M., Coggon, R.M., Wood, M., Smith-Duque, C.E., Henstock, T.J., Teagle, D.A.H., 2017. Hydrothermal cooling of the ocean crust: Insights from ODP Hole 1256D. Earth and Planetary Science Letters 462. https://doi.org/10.1016/j.epsl.2017.01.010

Harris, R.N., Chapman, D.S., 2004. Deep-seated oceanic heat flow, heat deficits, and hydrothermal circulation, in Hydrogeology of the Oceanic Lithosphere, in: Davis, E.E., Elderfield, H. (Eds.), Hydrogeology of the Oceanic Lithosphere with CD-ROM. Cambridge University Press, Cambridge, UK, pp. 311–336.

Hasterok, D., 2013. Global patterns and vigor of ventilated hydrothermal circulation through young seafloor. Earth and Planetary Science Letters 380, 12–20. https://doi.org/10.1016/j.epsl.2013.08.016

Herzfeld, U.C., 1993. A method for seafloor classification using directional variograms, demonstrated for data from the western flank of the Mid-Atlantic Ridge. Math Geol 25, 901–924. https://doi.org/10.1007/BF00891050

Hutnak, M., Fisher, A.T., Harris, R., Stein, C., Wang, K., Spinelli, G., Schindler, M., Villinger, H., Silver, E., 2008. Large heat and fluid fluxes driven through mid-plate outcrops on ocean crust. Nature Geosci 1, 611–614. https://doi.org/10.1038/ngeo264

Kadko, D., Baross, J., Alt, J., 1995. The Magnitude and Global Implications of Hydrothermal Flux, in: Humphris, S.E., Zierenberg, R.A., Mullineaux, L.S., Thomson, R.E. (Eds.), Geophysical Monograph Series. American Geophysical Union, Washington, D. C., pp. 446–466. https://doi.org/10.1029/GM091p0446

Karson, J.A., 2002. Geologic Structure of the Uppermost Oceanic Crust Created at Fast- to Intermediate-Rate Spreading Centers. Annu. Rev. Earth Planet. Sci. 30, 347–384. https://doi.org/10.1146/annurev.earth.30.091201.141132

Karson, J.A., Elthon, D., 1987. Evidence for variations in magma production along oceanic spreading centers: A critical appraisal. Geol 15, 127. https://doi.org/10.1130/0091-7613(1987)15<127:EFVIMP>2.0.CO;2

Langseth, M.G., Becker, K., Von Herzen, R.P., Schultheiss, P., 1992. Heat and fluid flux through sediment on the western flank of the Mid-Atlantic Ridge: A hydrogeological study of North Pond. Geophys. Res. Lett. 19, 517–520. https://doi.org/10.1029/92GL00079

Langseth, M.G., Hyndman, R.D., Becker, K., Hickman, S.H., Salisbury, M.H., 1984. The Hydrogeological regime of Isolated Sediments Ponds in Mid-Oceanic Ridges, in: Initial Reports of the Deep Sea Drilling Project, 78B, Initial Reports of the Deep Sea Drilling Project. U.S. Government Printing Office, pp. 825–837. https://doi.org/10.2973/dsdp.proc.78b.1984

Lindsey, C.R., Price, A.N., Burns, E.R., 2022. Exploring declustering methodology for addressing geothermal exploration bias, in: Geothermal Resource Council Transactions.

López, D.L., Smith, L., 1996. Fluid flow in fault zones: Influence of hydraulic anisotropy and heterogeneity on the fluid flow and heat transfer regime. Water Resour. Res. 32, 3227–3235. https://doi.org/10.1029/96WR02101

Los Alamos Grid Toolbox, LaGriT, 2019.

Macdonald, K.C., Fox, P.J., Alexander, R.T., Pockalny, R., Gente, P., 1996. Volcanic growth faults and the origin of Pacific abyssal hills. Nature 380, 125–129. https://doi.org/10.1038/380125a0

Matheron, G., 1963. Principles of geostatistics. Economic Geology 58, 1246–1266. https://doi.org/10.2113/gsecongeo.58.8.1246

McDuff, R.E., 1984. The chemistry of interstitial waters from the upper ocean crust, Site 395, Deep Sea Drilling Project Leg 78B. In Hyndman, R.D., Salisbury, M.H., et al., Init. Repts. DSDP, 78B: Washington, DC (U.S. Govt. Printing Office) 795–799. https://doi.org/10.2973/dsdp.proc.78b.114.1984

Neira, N.M., Clark, J.F., Fisher, A.T., Wheat, C.G., Haymon, R.M., Becker, K., 2016. Cross-hole tracer experiment reveals rapid fluid flow and low effective porosity in the upper oceanic crust. Earth and Planetary Science Letters 450, 355–365. https://doi.org/10.1016/j.epsl.2016.06.048

Olea, R.A., 2007. Declustering of Clustered Preferential Sampling for Histogram and Semivariogram Inference. Math Geol 39, 453–467. https://doi.org/10.1007/s11004-007-9108-6

Price, A.N., Fisher, A.T., Stauffer, P.H., Gable, C.W., 2022. Numerical Simulation of Cool Hydrothermal Processes in the Upper Volcanic Crust Beneath a Marine Sediment Pond: North Pond, North Atlantic Ocean. Journal of Geophysical Research: Solid Earth 127, e2021JB023158. https://doi.org/10.1029/2021JB023158

Pyrcz, M.J., Deutsch, C.V., 2018. Transforming Data to a Gaussian Distribution [WWW Document]. URL https://geostatisticslessons.com/lessons/normalscore (accessed 7.28.22).

Schmidt-Schierhorn, F., Kaul, N., Stephan, S., Villinger, H., 2012. Geophysical site survey results from North Pond (Mid-Atlantic Ridge), Proceedings of the IODP. Integrated Ocean Drilling Program. https://doi.org/10.2204/iodp.proc.336.2012

Schulze-Makuch, D., Carlson, D.A., Cherkauer, D.S., Malik, P., 1999. Scale Dependency of Hydraulic Conductivity in Heterogeneous Media. Groundwater 37, 904–919. https://doi.org/10.1111/j.1745-6584.1999.tb01190.x

Stauffer, P.H., Lewis, K.C., Stein, J.S., Travis, B.J., Lichtner, P., Zyvoloski, G., 2014. Joule–Thomson Effects on the Flow of Liquid Water. Transp Porous Med 105, 471–485. https://doi.org/10.1007/s11242-014-0379-3

Stein, J.S., Fisher, A.T., 2001. Multiple scales of hydrothermal circulation in Middle Valley, northern Juan de Fuca Ridge: Physical constraints and geologic models. Journal of Geophysical Research: Solid Earth 106, 8563–8580. https://doi.org/10.1029/2000JB900395

Stephen, R.A., 1981. Seismic anisotropy observed in upper oceanic crust. Geophysical Research Letters 8, 865–868. https://doi.org/10.1029/GL008i008p00865

Wheat, C.G., Becker, K., Villinger, H., Orcutt, B.N., Fournier, T., Hartwell, A., Paul, C., 2020. Subseafloor Cross-Hole Tracer Experiment Reveals Hydrologic Properties, Heterogeneities, and Reactions in Slow-Spreading Oceanic Crust. Geochemistry, Geophysics, Geosystems 21, e2019GC008804. https://doi.org/10.1029/2019GC008804

Wheat, C.G., McDuff, R.E., 1995. Mapping the fluid flow of the Mariana Mounds ridge flank hydrothermal system: Pore water chemical tracers. J. Geophys. Res. 100, 8115–8131. https://doi.org/10.1029/95JB00047

Zyvoloski, G.A., Robinson, B.A., Dash, Z.V., Kelkar, S., Viswanathan, H.S., Pawar, R.J., Stauffer, P.H., Miller, T.A., Chu, S., 2015. Software Users Manual (UM) for the FEHM Application Version 3.1 - 3.X. Los Alamos National Laboratory.

Chapter 3: Considerations in Meshing for Three-dimensional Simulation of Seafloor Hydrothermal Circulation, Including Bathymetric Relief and Patchy Sediment

Abstract

Constructing numerical computational meshes that accurately reproduce geologic features of interest is a key step in the investigation of environmental processes. However, there exists a substantial gap between software tools to perform the meshing and the application of meshes in numerical simulation. Here we present a framework for constructing geologically realistic meshes that uses North Pond, a ridge-flank hydrothermal system as an applied use case. We find that by making a suite of decisions prior to construction as well as using a nested grid structure, we are able to construct meshes that reproduce geological features and are numerically efficient. Additionally, we construct and distribute a suite of user-friendly, open-source tools that ensures reproducibility and the ability to adapt this workflow across mesh cases.

3.1. Study motivation, setting, and goals

3.1.1 Bridging the gap between development and application

Many types of software exist to construct, design specific portions (e.g. Sweeney et al., 2020), or size and type of specific elements of numerical simulation domains, henceforth referred to as “meshes or computational meshes” (Miller et al., 2007). However, there are relatively few studies that bridge the gap between theory and application that focus on the development of a mesh and the suite of decisions that are made in that process. Accurate representation of geometry and structure of geologic domains is paramount in numerical simulations focused on coupled fluxes of fluid and heat in hydrothermal systems. Here we develop an applied workflow that focuses on how to use data and knowledge about the geologic structure of the ocean crust, to construct a computational mesh while discussing the rationale behind the decisions made in mesh construction process.

Numerical modeling has been used in multiple studies of marine hydrothermal systems, but historically, little emphasis has been placed on the geometry, resolution, and geological realism or complexity of the system simulated. For example, many early models of mid-ocean ridge (MOR) systems used very coarse resolution, two-dimensional meshes with little to no geological complexity that resulted in large hydrothermal convection cells (Fehn & Cathles; 1979, Ribando et al., 1976, Patterson, 1976). As computational power and data quality improved, two-dimensional meshes with multiple resolutions, geologically realistic layering, and curvilinear elements to accurately represent seafloor topography were successfully used to elucidate marine hydrothermal processes (Fisher & Narasimhan, 1991; Fisher 1994). More recently, three-dimensional meshes were used in numerical simulation, but are very similar to early two-dimensional meshes in that they are highly idealized geometries (some with constant, coarse resolution), do not incorporate geological complexity, and lack key crustal features (Travis et al., 1991; Rabinowicz et al., 1998; 1999; Coumou et al., 2008; 2009; Fabrice et al., 2014; Hasenclever et al., 2014). At the bleeding edge of marine hydrothermal research, meshes used in studies of ridge-flank hydrothermal systems have been constructed to represent basement outcrops, reproduce important geological features, represent seafloor topography, and address multiple scales of physics by using a nested fine resolution area surrounded by a coarse resolution area (Lauer et al., 2018; Winslow & Fisher, 2015; Winslow et al., 2016). While each of these meshes has their inherent short-falls, the mesh constructed in this study incorporates realistic geological complexity with subsurface layering, seafloor topography, and targeted and varied mesh resolution in three-dimensions.

It is important when investigating marine hydrothermal systems, to not make assumptions our data is unable to support. For example, for many current tools one needs to know size, depth, orientation, and lateral continuity of fractures in the subsurface or complete many realizations and simulations. However, for marine hydrothermal systems and especially ocean worlds, we do not currently have that data and therefore cannot justify assumptions to achieve that level of detail. This study brings models/grids up to date as far as we can push the data, without going into the unknown and untestable.

3.1.2 North Pond, a marine sediment pond

For this study, we explore a ridge-flank hydrothermal system, North Pond, as a case study to explore the suite of decisions and workflow used in constructing a mesh. North Pond is a marine sediment pond that is surrounded by large areas of exposed volcanic crust, that sits on ~8 M.y. old seafloor at a depth of 4400 meters below sea-level (Hussong, 1979). The local and regional setting of North Pond is characterized by alternating horsts and grabens with abyssal hill topography that trends subparallel to the Mid-Atlantic Ridge (MAR) some 120 km to the east of the study site. North Pond is an especially useful study site because of the anomalously high amount of data collected in the area (for a submarine system) that have been used to constrain studies of the geochemical and microbiological signature produced by the transport of fluid and heat in the crustal aquifer beneath the sediment pond (Langseth et al., 1992; Orcutt et al., 2013; Price et al., 2022; Wheat et al., 2020).

3.1.3 Study goals and structure

This study provides a workflow and supplementary suite of tutorials and scripts for numerical modelers to incorporate bathymetric or topographic relief into meshes, representing first order and fundamental geometric characteristics needed to simulate ridge-flank hydrothermal systems with potential for application in other settings. The workflow presented takes a stepwise approach that combines constructing surfaces, defining simulation domain and subdomain volumes, mesh refinement, and material assignment. We discuss creation of numerical domains used for simulation of coupled fluid-heat transport in volcanic rocks and sediment in and around the North Pond field area, as a means to demonstrate conceptualization of key system features and properties, and how these may be implemented as part of mesh creation.

3.2. Steps for constructing geologically realistic, three-dimensional meshes

3.2.1 General workflow, nomenclature, and tools

A workflow for construction of geologically realistic mesh for simulation includes:

1. Defining surfaces
2. Creating a mesh with points and connections
3. Refining the mesh within volumes and along surfaces
4. Combining surfaces with simple geometric elements to define subseafloor regions and material zones
5. "Cleaning up" of the mesh to remove unnecessary components (**Figure 3-1**).

In this study, points are defined in cartesian space and denote vertices of elements, which finite element solvers use to discretize and solve governing equations for fluid, heat, solutes, etc. A set of points is created within space to define the extent of the mesh and are classified as falling within subregions that can be distinct or overlapping to define complex geological shapes and structures. Surfaces are defined by connections of sets of points, volumes are extruded surfaces but have no internal connections, domains are sets of points that have interior and exterior connections (**Figure 3-1a**).

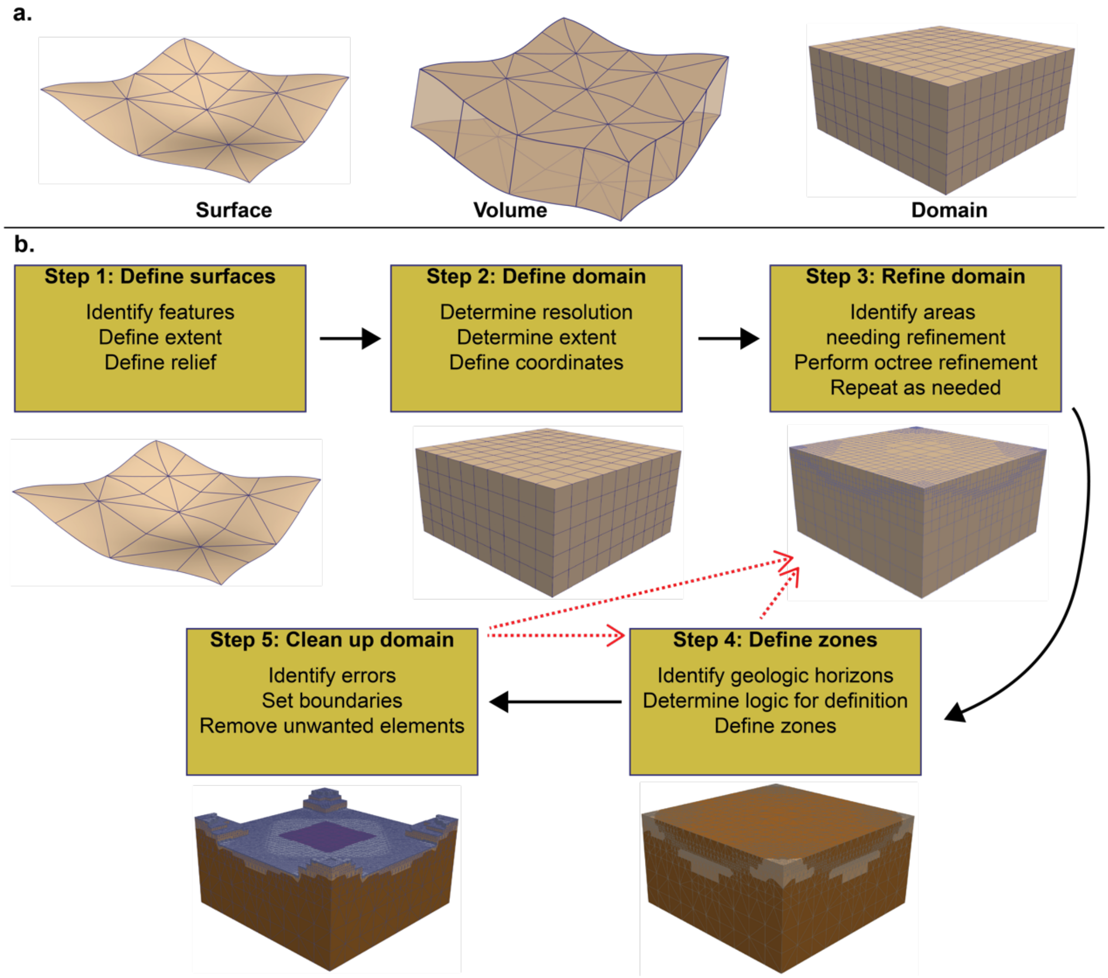

Figure 3-1: **a**. Visualizations for mesh objects used in workflow. **b**. Workflow for constructing meshes. Black arrows represent general flow while dashed red arrows represent steps that could be iterative.

We construct meshes with the Los Alamos Grid Toolbox (LaGriT). LaGriT is an open-source library of gridding tools that utilizes a Delaunay tetrahedralization algorithm for unstructured meshes generation in two- and three-dimensions ("Los Alamos Grid Toolbox, LaGriT," 2019). LaGriT has the capability to represent multiple element types including hexahedral and tetrahedral elements which are the primary elements used in this study.

A tutorial with all input files and scripts needed to recapitulate mesh construction for both use cases is included in the supplementary information (**Appendix B**).

3.2.2 Conceptual considerations for mesh geometry

During the construction of any mesh, a suite of decisions must be made about what geologic and physical processes we are interested in representing within the domain. Studies within North Pond have focused on scales of 10's to 1000's of meters due to spacing of borehole observatories and resolution of geophysical measurements within the sediment pond (Langseth et al., 1984, 1992; Wheat et al., 2020). This need to represent multiple scales of observation requires identification and reproduction of features that are important not only for accurately describing the hydrogeological flow regime of North Pond but are simultaneously valuable for other investigations and provide constraints for simulation outputs. The following mesh characteristics are important features we have identified that need to be represented in the North Pond mesh:

- A layered system with a seafloor above separate regions representing marine sediments, upper-volcanic crustal aquifer of varying thicknesses, and a lower volcanic unit of conductive crust. On ocean ridge flanks, such as North Pond, the uppermost 500 - 1000 m of the upper-volcanic ocean crust is permeable enough to allow fluid flux and facilitate advective removal of lithospheric heat (Fisher et al., 2014). At depths below the base of the crustal aquifer, conduction is the dominant mode of transport of lithospheric heat. The domain can be created to have uniquely specified layers, so that aquifer thickness can be treated as a "free parameter" in numerical simulations by modifying layer properties.

- Realistic geometry of the sediment pond with varying sediment thicknesses, asymmetric slopes along the sediment / basement contacts, and sediment "pinchouts" or thinning sediments along the margins of the sediment pond as observed in geophysical data (Schmidt-Schierhorn et al., 2012; Villinger et al., 2018)
- Geologic geometry that accurately represents the regional and local bathymetry relief.

3.2.3.1 Constructing representative surface for North Pond

The first step in the construction of a mesh is to construct surfaces that represent geologically realistic layers. These surfaces will define boundaries that allow assignment of specific material properties, boundaries between materials, and act as surfaces to refine the mesh. Defining coordinates for surfaces can be done with LaGriT or using separate calculations (e.g., with R, Python, or Matlab) and imported into LaGriT; the latter approach was used in development of North Pond grid surfaces. This approach allows a user to construct the fundamental properties of a surface and then use algorithms within LaGriT to ensure the best connections are made between points.

In the case of the North Pond mesh, mapping and seismic reflection data are used to define the geometries of specific surfaces, particularly the seafloor and the contact between sediment and the upper volcanic crust (Price et al., 2022; Price et al., *in review*). The seafloor surface (bathymetric relief) is determined with swath map data having regional resolution of 10 m (Villinger et al., 2018) and the subseafloor sediment-basement interface between is picked from seismic reflection data (Schmidt-Schierhorn et al., 2012) (**Figure 3-2**). In order to apply these observations to mesh construction, coordinates need to be shifted and rotated to align our mesh axis with the hypothesized primary direction of flow as well as to be consistent with the chosen cartesian reference frame (Anderson et al., 2015). Additionally, seafloor bathymetry is filtered to isolate low-order (large-scale) geometric features, and seismic two-way travel times converted to depths below seafloor.

To isolate first-order characteristics of the bathymetry of North Pond and the surrounding region, swaths of 70 - 90 km transects across and along the regional strike are down-sampled from 10 m to 60 m lateral resolution (**Figure 3-3**). High-frequency variations are suppressed with a low-pass filter, applied using a discrete Fourier transform, and the six dominant frequencies are used with an inverse Fourier transform to create smoothed bathymetry in the spatial domain. The key concept here is that the numerical study should focus on longer-wavelength features, so that the results will be general in nature and broadly applicable. Short-period features could be important for small-scale processes, but as discussed below, there are greater limitations in the resolution of subseafloor features, and the focus of numerical work is on coupled fluid and heat transport at the scale of North Pond (~kilometers) rather than processes that operate at the spacing of adjacent heat flux measurements (~10s to 100s of meters).

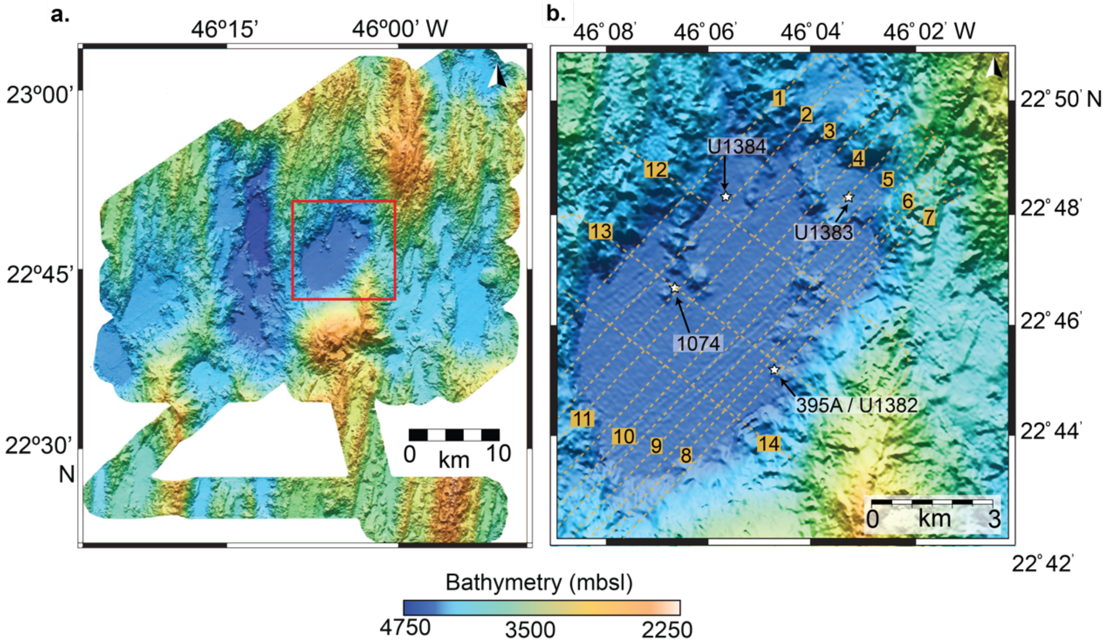

Figure 3-2: Regional and local bathymetric setting of North Pond. **a.** Regional bathymetric swath map with local North Pond area in red box. **b.** North Pond bathymetric sounding data with seismic lines from Schmidt-Scheirhorn et al., 2012. White stars represent borehole locations.

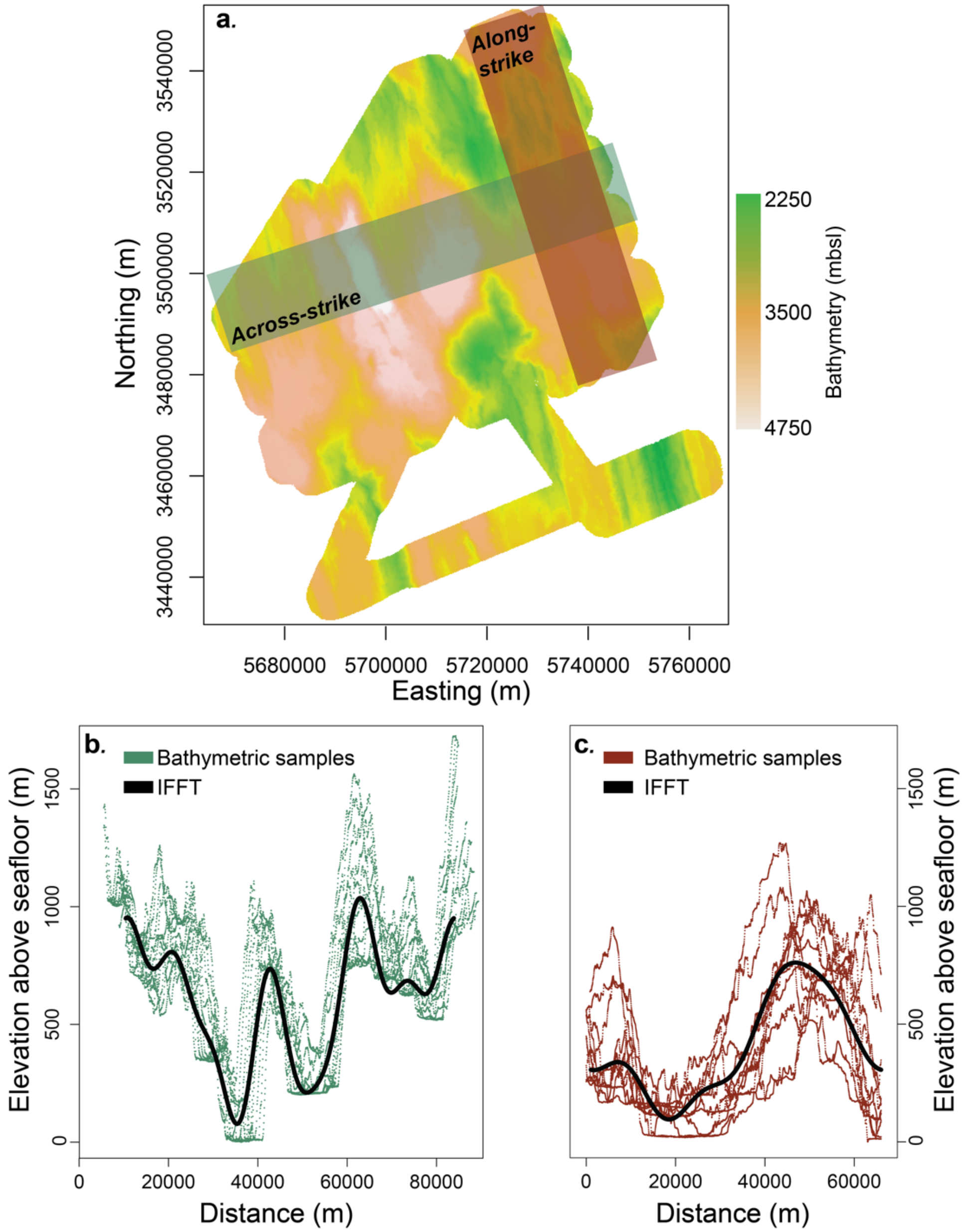

Figure 3-3: Figure adapted from Price et al., 2022 for bathymetric sampling and DFT results. **a.** Transect sample locations of bathymetric sound data from Villinger et al., 2018 for across- and along-strike transects. **b.** Across-strike bathymetric sounding samples **c.** Along-strike bathymetric sounding samples. Results of inverse Fourier transform in black for each sample transect.

Seismic reflection data are used to identify key horizons, especially to define the geometry of the sediment pond: the seafloor in North Pond (**Figure 3-4, light blue**), exposed volcanic crust around North Pond (**Figure 3-4, green**), and sediment-basement interface below North Pond (**Figure 3-4, brown**). The seafloor above North Pond sediments is easiest to pick as there are clear, subhorizontal double reflectors (positive-negative-positive) marking the seafloor impedance contrast. The lateral extent of this reflector defines the edges of North Pond, where sediments pinch out. Side echoes are absent at shallower depths, far above North Pond, allowing definition of the volcanic rock slopes extending upward from the edges of North Pond sediments. The sediment-basement transition is often well defined where this feature is relatively flat and horizontal but is less distinct along buried slopes where the boundary rises to meet the seafloor (**Figure 3-4**). Once these features are picked, shot point locations are converted to lateral distances using ship navigation data, and two-way travel time within North Pond sediment is converted to equivalent depth using seismic velocities from North Pond core data (Edwards et al., 2012).

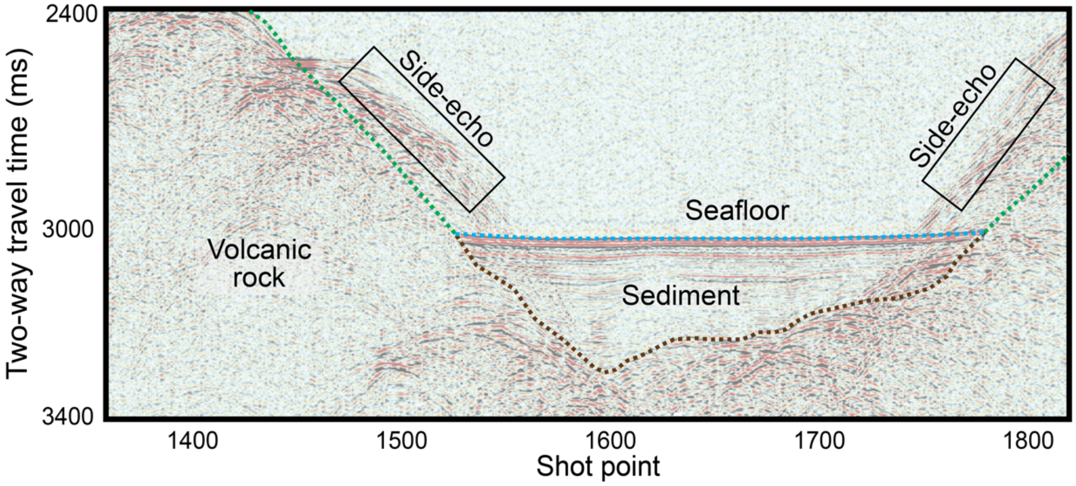

Figure 3-4: Seismic reflection profile of two-way travel time versus shot point from seismic line SCS-14 (Schmidt-Scheirhorn et al., 2012). Important features are noted on the plot such as: side-echoes (black boxes), seafloor (blue), sediment-basement contact (brown), exposed volcanic crust (green).

3.2.4 Define elements, extent, and resolution of mesh

There are many considerations in defining the overall shape and dimensions of the mesh (full simulation domain). It is generally wise to place the primary region of interest far from mesh boundaries, so we add buffer regions around the North Pond basin, resulting in a geometry that extends ~3x the size of North Pond in map view. Placing the domain boundaries in the far field area minimizes the influence of “hard” boundary conditions on the near field (e.g., Anderson et al., 2015; Haitjema, 1995). A similar approach is common in hydrologic modeling of catchments (e.g., Modica et al., 1997). It is also wise in coupled fluid-heat transport to define a domain base that is far from the bottom of the most hydrogeologically active region, by a factor of 3-4x, allowing conductive isotherms in the deeper crust to be warped by rapid flows in the shallow crust resulting in coupled feedback between fluid and heat transport. In contrast, if the lower domain boundary is placed immediately below the crustal aquifer, this will limit the extent of lateral heat flow that could occur as a result of shallow convection (Johnson et al, 2022).

Finite element shape is important for determining the nature of geologic features that can be represented. Careful consideration should be placed on resolution of the resulting elements as defined by the shape and dimensions of a mesh. In general, the aspect ratio for element sides should be close to 1 and ratios >5 should be avoided (e.g., Anderson et al., 2015). As described in the rest of this sections, a mesh is defined first with a relatively coarse resolution, then refined sequentially to achieve the desired geometry. The initial mesh is based on a rectangular grid with elements all having the same dimensions.

3.2.5 Refine mesh along surfaces and within volumes

Refinement along certain boundaries or within volumes increases the resolution of the mesh only in those areas and allows more accurate representation of the areas of interest. Nested refinement reduces the computational cost and memory footprint of numerical simulation, by increasing the resolution in specific areas of interest while maintaining a coarser grid outside of those areas (e.g., Sweeney et al, 2020). We use a technique called “octree-refinement” to refine the mesh along specified boundaries or surfaces, based on an octree data structure, where each "parent" element has eight smaller "child" elements, therefore converting any element intersected by the surface into eight elements, or octants (Meagher, 1982).

Within LaGriT this approach can be used to refine meshes using a single point (e.g., an injection point), line (e.g., well), surface (e.g., stratigraphic boundary), or a volume (e.g., tabular stratigraphic section). For this study, we refine only using surfaces. The order of which refinement is performed needs to be considered if multiple intersecting features are refinement targets, as over-refinement can occur, producing excess elements with very small dimensions. To avoid over-refinement of elements, LaGriT stores arrays that contain information about the number of refinements an element has experienced, which allows a user to filter out elements that have been refined beyond the desired correct resolution or refinement level.

3.2.6 Define material zones corresponding to stratigraphic units

The next step in the mesh generation process is to define material zones that correspond to stratigraphic units of interest. Similar to refining the mesh above, definition of material zones can be done with conditional statements that use points, lines, surfaces, and volumes. Defining material zones can be accomplished by selecting elements or points that intersected by a surface or are intersected or lie within a volume. Surfaces are used mainly to define the topographic surfaces or transitions between material zones, while volumes are used to define tabular sections of material zones such as a subregion of a stratigraphic section. Importantly, points can be assigned concurrently to multiple zones; this is helpful, for example, for assigning some seafloor points to be the top of the sediment section (part of a surface) or assigning a group of points in a section of aquifer (a volume).

3.2.7 Cleanup mesh, material zones, and removing elements

The final steps in construction of geologically realistic meshes are to clean up or address any issues that may have arisen in previous steps. Issues that commonly arise are elements with aspect ratios <<1 or >>1, removal of any unnecessary elements or material zones, and defining material zones for the seafloor and domain base to aid in setting numerical boundary conditions when running simulations.

3.3. Geometric and simulation characteristics of geologically realistic meshes

3.3.1.2 North Pond mesh

The North Pond mesh consists of 1.4 x 10^6 volume elements that comprise a mesh with dimensions of x_{min}, y_{min}, z_{min} = -24000, -40000, -6000 m to x_{max}, y_{max}, z_{max} = 16000, 55000, 937 m. Using the nested structure described above, the finest resolution is in the immediate area of North Pond, where the minimum length of the elements is ~10 m and the resolution far from North Pond is 750 m (**Figure 3-5**). Additionally, since the purpose of this mesh is for numerical simulation of heat and fluid flux beneath the sediment of North Pond, the contact between the sediment and the shallowest crustal layer is defined at high resolution. Elements near the center of the sediment pond (e.g., farther from the sediment-aquifer contact) have coarser resolution than do those near the interface with basement rocks (**Figure 3-6**).

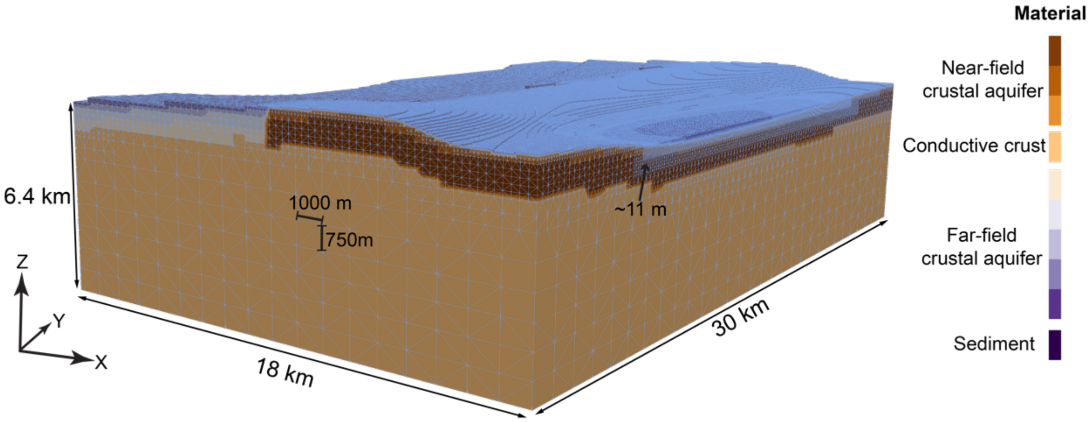

Figure 3-5: Detail view of nested material zones of high and low resolution in the area adjacent to and representing North Pond.

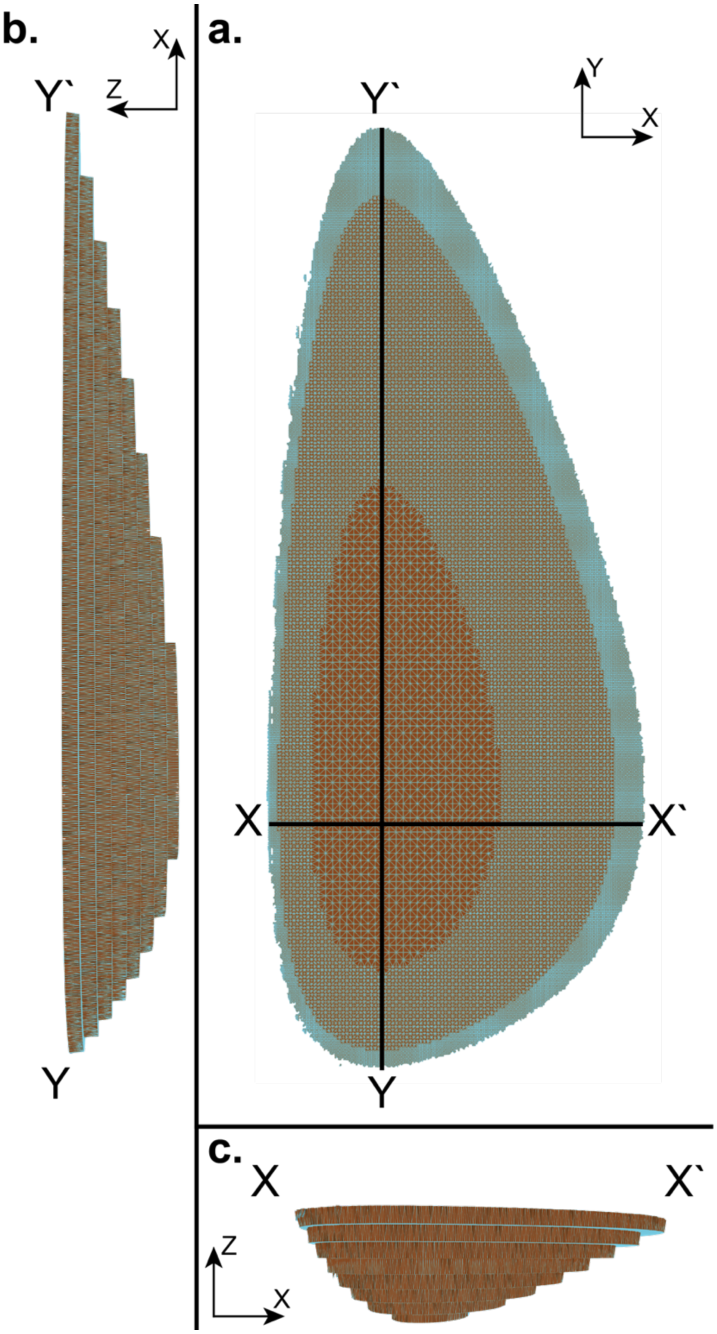

Figure 3-6: Sediment zone from final North Pond mesh with **a.** nested high- and low-resolution elements, **b.** along-strike profile of sediment thickness with steeper slopes to the south and shallower slopes to the north, **c.** across-strike profile of sediment thickness with steeper slopes to the west and shallower slopes to the east.

Having defined the general pattern of seafloor relief and the shape of the basin in which North Pond is located, we defined a continuous function that matches the first order characteristics of associated surfaces:

$$z(x,y) = \frac{1}{t} arctan\left(\frac{t * sin\,(x)}{1 - t * cos\,(x)}\right) - \frac{1}{t} arctan\left(\frac{t * sin\,(y)}{1 - t * cos\,(y)}\right)$$

where *t* determines the "tilt" of the function (generating asymmetry in the sediment-basement interface below North Pond), *y* is the distance along-strike of North Pond, and *x* is distance across-strike of North Pond. This function is then extended three wavelengths in both the along- and across-strike directions.

Additional surfaces that represent transitions between aquifer layers are constructed from the entire domain surface by duplicating this surface and incrementally shifting it downward by forming boundaries between crustal layers. Use of each of these boundaries with the top-of-basement surface defines crustal intervals having thicknesses of 100 m, 300 m, 600 m, and 1000 m, respectively. The mesh contains material zones defined to allow targeted classification of material properties. Truncated surfaces that comprise a fraction of the simulated region, define material zones and represent the highest resolution area of interest directly adjacent to North Pond (**Figure 3-6 and 7**). Surfaces that extend beyond the immediate area of interest define material zones corresponding to volcanic rocks comprising the crustal aquifer and conductive boundary layers at a coarser resolution to aid in numerical efficiency.

In order to reproduce the geologic structures of interest and place boundaries far from the area of greatest interest, the North Pond mesh comprises approximately three wavelengths of seafloor relief, with North Pond represented by an asymmetric, sediment-filled depression (~250 m maximum sediment thickness), four topographic highs, and eight partial "buffer ponds" (**Figure 3-7**). The mesh was partly truncated (buffer ponds are incomplete) to decrease the total number of elements, decreasing computational time. The asymmetric sediment pond has steeper (15%) sloping sediment-basement contacts on the western and southern margins and shallower (5%) sloping contacts on the northern and eastern margins (**Figure 3-6a and b**). This asymmetry results in the deepest part of North Pond being in the southwestern quadrant of the pond. The topographic highs surrounding the pond reach the 1000 m maximum height relative to the top of North Pond sediment.

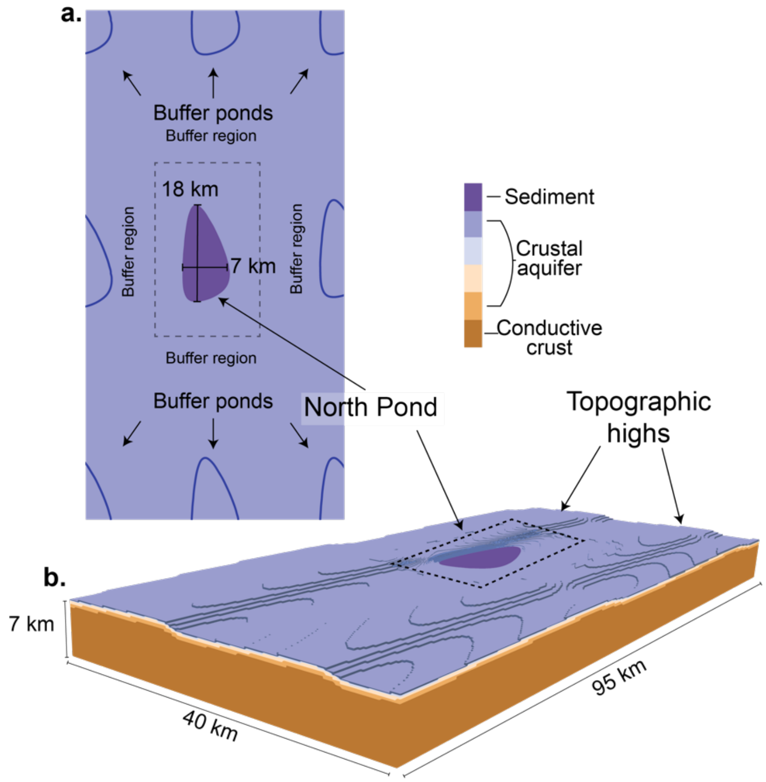

Figure 3-7: Entire North Pond domain with important features adapted from Price et al., 2022. **a.** Map view of final North Pond tetrahedral mesh showing buffer regions and eight buffer ponds. **b.** Perspective view of final North Pond tetrahedral mesh with geometric features and dimensions.

3.3.2 Simulation characteristics of North Pond mesh

Here we demonstrate some characteristics of conductive and coupled simulations of fluid-heat transport in and around North Pond, which helps to explain why decisions were made concerning issues such as grid resolution and material definitions. We begin with evaluation of heat flux refraction in a conductive simulation. Conductive refraction is the warping of subsurface isotherms as a consequence of contrasts in thermal properties and/or topography (Lachenbruch, 1968; Lees, 1910). The consequence of refraction in a conductive simulation of North Pond, with lower conductivity sediments filling a depression and surrounded by higher conductivity, volcanic rocks, is that ~38% of lithospheric heat entering the crust below North Pond exits beyond the limits of the sediment pinchout (Price et al., 2022; **Figure 3-8**). Even in the absence of coupled fluid-heat transport in the crust below North Pond, the expected seafloor heat flux through North Pond sediments is less than input below the basin.

Previous coupled simulations of fluid and heat show that the asymmetric shape of the sediment pond, due to the differing slopes of the sediment-basement contact of North Pond, greatly influences the geometry of advective removal of heat from beneath the pond (Price et al., 2022; Price et al., *in review*). The convective pattern of fluid flux beneath the sediment pond is characterized by two large convective cells that recharge cold fluids from the margins of the pond, rise at the point of maximum sediment thickness, and discharge warm fluids around the margins of the pond. The bulk of this fluid flow is along the short axis of North Pond, coinciding with the steeper asymmetric slopes, which is a fundamental characteristic of North Pond that we were able to reproduce. Additionally, sediment pinchouts observed and reproduced in the mesh are important hydrogeologic features that conduct high heat fluxes efficiently with no fluid flux through the sediment, which is an important observational constraint (McDuff, 1984; Price, et al., 2022). The takeaway from these simulations is that the low-order geometric characteristics of North Pond have a profound effect on the hydrogeologic and thermal regime in the volcanic aquifer beneath the pond. The ability for the North Pond mesh to capture this process places it at a clear advantage over other meshes that neglect geometry and geological complexity.

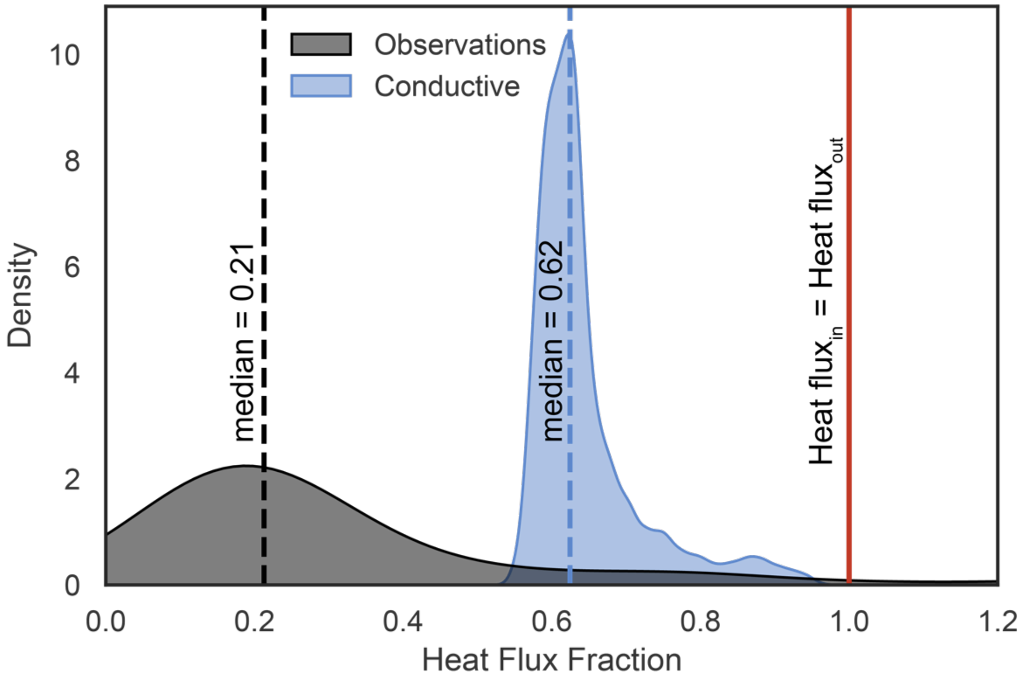

Figure 3-8: Multiple probability density plot of heat flux fraction (heat flux in / heat flux out) for heat flux observations from North Pond, conductive simulation using North Pond grid, and expected lithospheric input of North Pond. Dashed lines correspond to median (q_{50}) of distribution.

As discussed in previous sections, this mesh focuses on representing longer-wavelength features, general in nature of a geologic feature, and broadly applicable across the seafloor, disregarding small-scale variably. Many studies exist that address the appropriate grid resolution needed to capture coupled fluxes across complex geologic domains (Zyvoloski et al., 2006; Bower et al., 2006, Haitjema et al., 2001, LaForce et al., 2022). In our case, the mesh resolution for North Pond was guided by a combination of prior studies, geophysical data, and physical processes. The resolution of the geophysical data, that is the spacing of the heat flux measurements, bathymetric sounding data, and seismic reflection profiles are all on the order of 10's – 100's of meters while the hypothesized large-scale processes operate on the scale of 100's -1000's of meters. The resulting North Pond mesh has the coarsest resolution of 1 km on the largest volumes, far-field from the area of interest, and finest resolution of ~15 m on the smallest volumes near-field to the area of interest along the sediment-basement contact. Coupled simulations of the North Pond mesh, show that this resolution is sufficient to capture the convective flow patterns in the subsurface aquifer. Using a power-spectral density analysis to analyze the dominant periods of convection within the simulations, we found that convective cells on the order of ~175 m were the most dominant, although there were a broad range of pronounced periods from ~900m to ~45 m (**Figure 3-9d**). All of these dominant periods are larger than the smallest grid spacing and provide positive confirmation that our resolution is able to capture processes within the crustal aquifer.

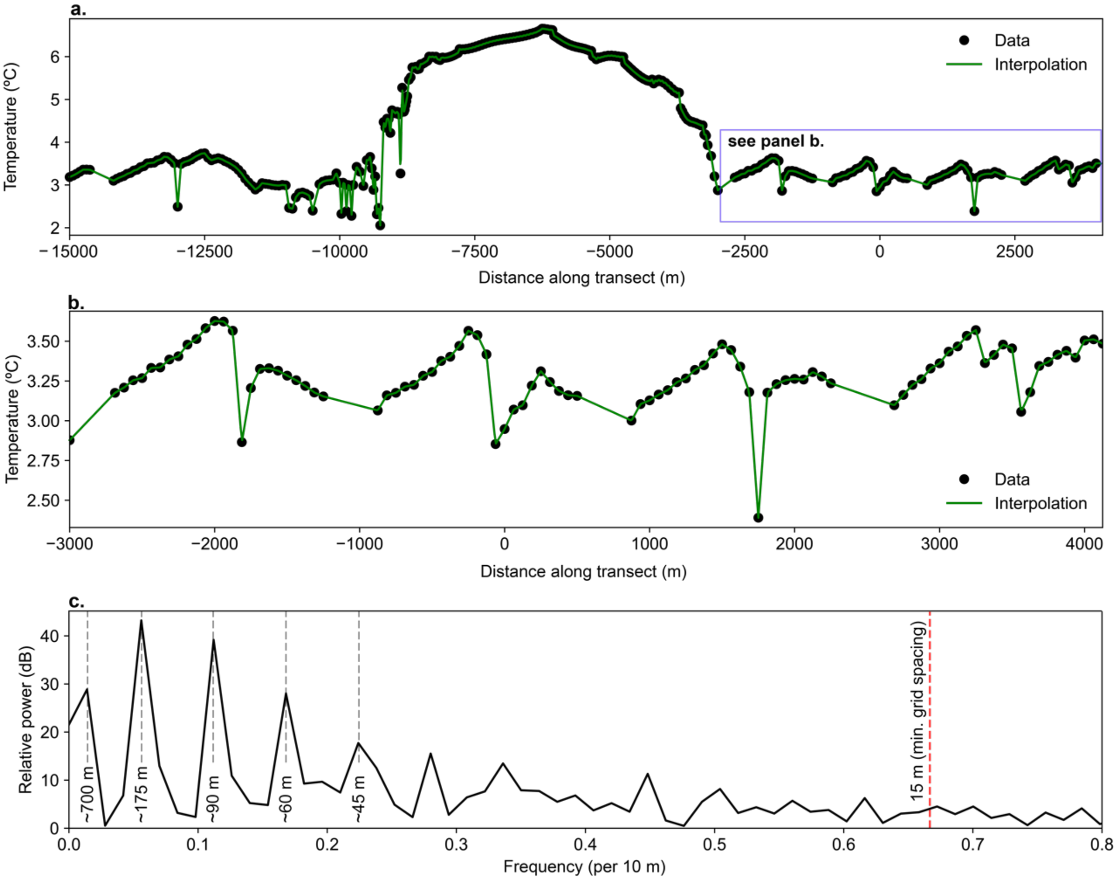

Figure 3-9: Temperature changes observed in aquifer beneath North Pond and resulting power spectral density analysis. **a.** Plot of simulated temperatures in the 100 m aquifer layer along mesh transect y = 12000 m from x = -15000 to x= 4000 in black and resulting interpolation at regular 10 m intervals in green. **b.** Detail plot of data shown in **Figure 3-9a**. **c.** Power spectral density analysis of data shown in **Figure 3-9a**, highlighting periods with relatively high power, with minimum grid spacing of 15 m marked in red dashed line. Frequencies are calculated relative to intervals of 10 days

Mesh resolution is not only important to correctly represent the geological complexity and physical processes of a system, but it also directly affects computational time. For example, the Courant number *(C*) is defined as:

$$C = \frac{u\Delta t}{\Delta x}$$

where *u* is the magnitude of velocity, Δ*t* is timestep, and Δ*x* is interval length (element size in our case), where *C* = ~1 to achieve numerical accuracy. Depending on the velocity of the system of interest, timesteps might have to be very small to bring the Courant number close to one. Therefore, maintaining a balance between number and more importantly size of elements needed to accurately represent a system is an important consideration. For example, simulations of the North Pond system that have very low mass and energy flux, total computational time was on the order of days with individual time steps of ~5 seconds for each year of simulated time. However, for simulations with higher mass and energy fluxes, total simulation time is on the order of months with individual steps of ~2.5 minutes for each year of simulated time. A caveat to this computation time is that FEHM is not currently parallelized, which could dramatically decrease simulation time.

3.3.3 Reproducibility

A key aspect of this study is the applied and open-source nature of the mesh construction workflow. As part of the study, we compiled an accompanying static tutorial document (**Appendix B**) that walks through each workflow step with background, syntax, and figures for the respective processes. Additionally, we include pseudo-code for the generalized and North Pond mesh cases that allow the user to adapt this workflow in a targeted approach by altering a few lines of code and include the input files as a data release (Price et al., 2022b). While we understand each of these tools has a learning curve, we provide as many resources as possible to construct meshes as well as for adaptation for other geologically realistic mesh use cases.

3.3.4 Limitations and future work

Generating computational meshes that accurately represent geologic complexity is important for accurate simulation, requiring integration of many kinds of data and tools, and often trial-and-error to assess impacts of many design choices as part of a complex workflow. The steps described and demonstrated in this study are useful, but the details will vary depending on the particular site conditions, available observations, and the numerical tools to be applied. In the case of North Pond, it is important to represent fundamental features like seafloor relief (including asymmetry), sediment thickness variations (including pinchouts), and contrasts in materials properties. However, there are small scale features that we chose to not represent, including local bathymetric highs within the sediment pond (**Figure 3-1b**). While these small-scale features are unlikely to affect the larger fluid and heat flow regime of North Pond, they certainly could influence local contrasts in heat flux and patterns of crustal recharge and discharge. Additionally, we assign aquifers to distinct, clearly defined units, but the upper ocean crust is complex and unlikely to be uniformly layered (e.g., Bartetzko et al., 2001; Fisher et al., 2014). This is less a result of the workflow shown, and more a consequence of limited understanding of three-dimensional layering and limits to key units. Boreholes are individual lines that sample basement rocks incompletely, and seismic reflection data has limited resolution. More accurate simulations can be generated on the basis of better understanding of subseafloor properties and conditions.

Future studies of constructing geologically realistic grids would ideally incorporate the use of a variety of gridding software, user-friendly open-source tools, and incorporate newer and wider varieties of geophysical data. We have made this tutorial open-source but these tools have a notable learning curve that could be slackened by using more user-friendly open-source computing languages. Stated in the limitations of the current mesh above, we suggest that future studies address irregular boundaries between stratigraphic sections, as well as provide a more user-friendly approach to quantifying the effects of grid resolution and boundary geometry on the results of numerical simulations.

3.4. Conclusions

This study presents a framework for constructing geologically realistic computational meshes for use in numerical simulations. This framework uses North Pond, a ridge-flank hydrothermal system for an applied mesh building case. We found that by using a nested grid structure and refinement along stratigraphic contacts of interest produce geologic meshes that are computationally efficient and stable (Price, et al., 2022; Price et al., *in review*). Furthermore, by providing a suite of user-friendly, open-source tools we ensure that users can reproduce and adapt the workflow to meet a broad suite of geologically realistic meshing use cases. Our ability to accurately represent these systems will improve with the adaptation of well-documented workflows, development of new tools, and new and continued sampling of geologic systems.

Acknowledgments

This chapter reflects a manuscript in preparation with the following coauthors: Andrew T. Fisher, Philip H. Stauffer, and Carl W. Gable.

This research was supported by National Science Foundation grants OIA-0939564 and OCE- 1924384. This work benefitted from discussions with K. Becker, T. Weathers, and many others involved in studies of North Pond and ridge-flank hydrogeology in general.

References

Anderson, M. P., Woessner, W. W., & Hunt, R. J. (2015). Applied Groundwater Modeling: Simulation of Flow and Advective Transport. Academic Press.

Bartetzko, A., Pezard, P., Goldberg, D., Sun, Y.-F., & Becker, K. (2001). Volcanic stratigraphy of DSDP/ODP Hole 395A: An interpretation using well-logging data. Marine Geophysical Researches, 22(2), 111–127.

Bower, K.M., Gable, C.W., Zyvoloski, G.A. (2005). Grid Resolution Study of Ground Water Flow and Transport. Groundwater 43, 122–132. https://doi.org/10.1111/j.1745-6584.2005.tb02291.x

Coumou, D., Driesner, T., Heinrich, C.A. (2008). The Structure and Dynamics of Mid-Ocean Ridge Hydrothermal Systems. Science 321, 1825–1828. https://doi.org/10.1126/science.1159582

Coumou, D., Driesner, T., Geiger, S., Paluszny, A., Heinrich, C.A. (2009). High-resolution three-dimensional simulations of mid-ocean ridge hydrothermal systems. Journal of Geophysical Research: Solid Earth 114. https://doi.org/10.1029/2008JB006121

Edwards, K. J., Bach, W., Klaus, A., & the Expedition 336 Scientists. (2012). Expedition 336, Mid-Atlantic Ridge Microbiology. In Proceedings of the Integrated Ocean Drilling Program (Vol. IODP, 336). Toyko: Integrated Ocean Drilling Program Management International, Inc. https://doi.org/10.2204/iodp.proc.336.101.2012

Fontaine, F.J., Cannat, M., Escartin,J., Crawford, W.C. (2014). Along-axis hydrothermal flow at the axis of slow spreading Mid-Ocean Ridges: Insights from numerical models of the Lucky Strike vent field (MAR). Geochemistry, Geophysics, Geosystems,15, 7, 2918-2931. https://doi.org/10.1002/2014GC005372

Fehn, U., Cathles, L.M. (1979). Hydrothermal convection at slow-spreading mid-ocean ridges. Tectonophysics 55, 239–260. https://doi.org/10.1016/0040-1951(79)90343-3

Fisher, Andrew T., Alt, J., & Bach, W. (2014). Hydrogeologic Properties, Processes, and Alteration in the Igneous Ocean Crust. In R. Stein, D. K. Blackman, F. Inagaki, & H.-C. Larsen (Eds.), Developments in Marine Geology (Vol. 7, pp. 507–551). Elsevier. https://doi.org/10.1016/B978-0-444-62617-2.00018-9

Fisher, A.T., Becker, K., & Narasimhan, T. N. (1994). Off-axis hydrothermal circulation: Parametric tests of a refined model of processes at Deep Sea Drilling Project/Ocean Drilling Program site 504. Journal of Geophysical Research: Solid Earth, 99(B2), 3097–3121. https://doi.org/10.1029/93JB02741

Haitjema, H. M. (1995). Analytic Element Modeling of Groundwater Flow. Elsevier.

Hasenclever, J., Theissen-Krah, S., Rüpke, L.H., Morgan, J.P., Iyer, K., Petersen, S., Devey, C.W. (2014). Hybrid shallow on-axis and deep off-axis hydrothermal circulation at fast-spreading ridges. Nature 508, 508–512. https://doi.org/10.1038/nature13174

Hussong, D. M. (1979). The geological and geophysical setting near DSDP Site 395, North Atlantic Ocean. Initial Reports of the Deep Sea Drilling Project, 45, 23.

Johnson, P.J., Stauffer, P.H., Omagbon, J., Moore, C.R., 2022. Implications of rootless geothermal models: Missing processes, parameter compensation, and imposter convection. Geothermics 102, 102391. https://doi.org/10.1016/j.geothermics.2022.102391

Lachenbruch, A. H. (1968). Rapid estimation of the topographic disturbance to superficial thermal gradients. Reviews of Geophysics, 6(3), 365–400. https://doi.org/10.1029/RG006i003p00365

LaForce, T., Ebeida, M., Jordan, S., Miller, T.A., Stauffer, P.H., Park, H., Leone, R., Hammond, G. (2022). Voronoi Meshing to Accurately Capture Geological Structure in Subsurface Simulations. Mathematical Geosciences https://doi.org/10.1007/s11004-022-10025-x

Langseth, M. G., Hyndman, R. D., Becker, K., Hickman, S. H., & Salisbury, M. H. (1984). The Hydrogeological regime of Isolated Sediments Ponds in Mid-Oceanic Ridges. In Initial Reports of the Deep Sea Drilling Project, 78B (Vol. 78B, pp. 825–837). U.S. Government Printing Office. https://doi.org/10.2973/dsdp.proc.78b.1984

Langseth, M. G., Becker, K., Von Herzen, R. P., & Schultheiss, P. (1992). Heat and fluid flux through sediment on the western flank of the Mid-Atlantic Ridge: A hydrogeological study of North Pond. Geophysical Research Letters, 19(5), 517–520. https://doi.org/10.1029/92GL00079

Lees, C. H. (1910). On the shapes of the isogeotherms under mountain ranges in radio-active districts. Proceedings of the Royal Society of London. Series A, Containing Papers of a Mathematical and Physical Character, 83(563), 339–346. https://doi.org/10.1098/rspa.1910.0022

Los Alamos Grid Toolbox, LaGriT. (2019). Los Alamos National Laboratory. Retrieved from http://lagrit.lanl.gov

McDuff, R. E. (1984). The chemistry of interstitial waters from the upper ocean crust, Site 395, Deep Sea Drilling Project Leg 78B. In Hyndman, R.D., Salisbury, M.H., et al., Init. Repts. DSDP, 78B: Washington, DC (U.S. Govt. Printing Office), 795–799. https://doi.org/10.2973/dsdp.proc.78b.114.1984

Meagher, D. (1982). Geometric modeling using octree encoding. Computer Graphics and Image Processing, 19(2), 129–147. https://doi.org/10.1016/0146-664X(82)90104-6

Miller, T., Vesselinov, V., Stauffer, P., Birdsell, K., Gable, C., (2007). Integration of Geologic Frameworks in Meshing and Setup of Computational Hydrogeologic Models, Pajarito Plateau, New Mexico. Mexico Geological Society Guide Book, 58th Field Conference, Geology of the Jemez Mountains Region II 492–500.

Orcutt, B. N., Wheat, C. G., Rouxel, O., Hulme, S., Edwards, K. J., & Bach, W. (2013). Oxygen consumption rates in subseafloor basaltic crust derived from a reaction transport model. Nature Communications, 4, 2539. https://doi.org/10.1038/ncomms3539

Patterson, P.L. (1976). Numerical modeling of hydrothermal circulation at ocean ridges. Dissertation. Georgia Institute of Technology

Price, A. N., Fisher, A. T., Stauffer, P. H., & Gable, C. W. (2022). Numerical Simulation of Cool Hydrothermal Processes in the Upper Volcanic Crust Beneath a Marine Sediment Pond: North Pond, North Atlantic Ocean. Journal of Geophysical Research: Solid Earth, 127(1), e2021JB023158. https://doi.org/10.1029/2021JB023158

Price, A. N., Gable, C. W., Fisher, A. T., & Stauffer, P. H. (2022b). Construction of Geologically Realistic, Three-Dimensional Meshes for Simulation of Subseafloor Hydrothermal Circulation, Including Bathymetric Relief and Patchy Sediment. Dryad, Dataset.

Price, A. N., Fisher, A. T., Lindsey, C. R., Stauffer, P. H., & Gable, C. W. (in review). The influence of permeability anisotropy in the upper ocean crust on advective heat transport by a ridge-flank hydrothermal system. Earth and Planetary Science Letters.

Rabinowicz, M., Boulègue, J., & Genthon, P. (1998). Two- and three-dimensional modeling of hydrothermal convection in the sedimented Middle Valley segment, Juan de Fuca Ridge. Journal of Geophysical Research, 103(B10), 24045– 24065, https://doi.org/10.1029/98JB01484

Rabinowicz, M., Sempere, J.C., & Genthon, P.(1999). Thermal convection in a vertical permeable slot: Implications for hydrothermal convection along mid-ocean ridges. Journal of Geophysical Research, 104, 29,275–29,292. https://doi.org/10.1029/1999JB900259.

Ribando, R.J., Torrance, K.E., Turcotte, D.L. (1976). Numerical models for hydrothermal circulation in the oceanic crust. Journal of Geophysical Research (1896-1977) 81, 3007–3012. https://doi.org/10.1029/JB081i017p03007

Schmidt-Schierhorn, F., Kaul, N., Stephan, S., Villinger, H. (2012). Geophysical site survey results from North Pond (Mid-Atlantic Ridge), In Proceedings of the IODP. Integrated Ocean Drilling Program 336. https://doi.org/10.2204/iodp.proc.336.2012

Sweeney, M. R., Gable, C. W., Karra, S., Stauffer, P. H., Pawar, R. J., & Hyman, J. D. (2020). Upscaled discrete fracture matrix model (UDFM): an octree-refined continuum representation of fractured porous media. Computational Geosciences, 24(1), 293–310. https://doi.org/10.1007/s10596-019-09921-9

Travis, B. J., D. R. Janecky, N. D. Rosenberg, 1991, Three-dimensional simulation of hydrothermal circulation at mid-ocean ridges, Geophysical Research Letters, 18(8); 1441-1444, https://doi.org/10.1029/91GL01776.

Villinger, H., Strack, A., Gaide, S., & Thal, J. (2018). Gridded bathymetry of North Pond (MAR) from multibeam echosounder EM120 and EM122 data of cruises MSM20/5 (2012) and MSM37 (2014) [Data set]. Department of Geosciences, Bremen University. PANGAEA. https://doi.org/10.1594/PANGAEA.889439

Wheat, C. G., Becker, K., Villinger, H., Orcutt, B. N., Fournier, T., Hartwell, A., & Paul, C. (2020). Subseafloor Cross-Hole Tracer Experiment Reveals Hydrologic Properties, Heterogeneities, and Reactions in Slow-Spreading Oceanic Crust. Geochemistry, Geophysics, Geosystems, 21(1), e2019GC008804. https://doi.org/10.1029/2019GC008804

Winslow, D. M., Fisher, A. T., Stauffer, P. H., Gable, C. W., & Zyvoloski, G. A. (2016). Three-dimensional modeling of outcrop-to-outcrop hydrothermal circulation on the eastern flank of the Juan de Fuca Ridge. Journal of Geophysical Research: Solid Earth, 121(3), 1365–1382. https://doi.org/10.1002/2015JB012606

Winslow, D. M., & Fisher, A. T. (2015). Sustainability and dynamics of outcrop-to-outcrop hydrothermal circulation. Nature Communications, 6(1), 7567. https://doi.org/10.1038/ncomms8567

Zyvoloski, G.A., Vesselinov, V.V., 2006. An Investigation of Numerical Grid Effects in Parameter Estimation. Groundwater 44, 814–825. https://doi.org/10.1111/j.1745-6584.2006.00203.x

Appendix A: Supporting Information for "Numerical Simulation of Cool Hydrothermal Processes in the Upper Volcanic Crust Beneath a Marine Sediment Pond: North Pond, North Atlantic Ocean"

Reprinted from:

Price, A.N., Fisher, A.T., Stauffer, P.H., Gable, C.W., 2022 "Numerical Simulation of Cool Hydrothermal Processes in the Upper Volcanic Crust Beneath a Marine Sediment Pond: North Pond, North Atlantic Ocean," Journal of Geophysical Research: Solid Earth 127.1, e2021JB023158 DOI: 10.1029/2021JB023158

Contents of this file

Text S1 - S3

Figures S1 - S8

Table S1-S2

Additional Supporting Information (Files uploaded separately)

Captions for Movies S1 to S2

Introduction

This supplement contains Text S1 - S3, which provides additional methodological details for domain construction, calculation of spatially varying basal heat flux, and calculation of Rayleigh numbers. It also contains figure S1 that describes the sampling and results from regional bathymetry and fast-Fourier transform, respectively. Figure S2 is an example seismic line taken from North Pond. Figures S3 and S8 are empirical distribution functions or the effects of conductive refraction and additional high-permeability simulations. Figure S4 is the resulting plot for calculations using the Rayleigh number equation in Text S3 for the range of physical conditions in North Pond.

Figures S5 and S6 are both figures illustrating the organizational structure of convection beneath North Pond. Figure S7 is a frequency analysis performed on simulation outputs. Table S1 lists the geometric constraints used in grid construction described in Text S1. Table S2 lists flow rates (specific discharge) statistics for figure S6. Movies S1 and S2 are two- and three-dimensional simulation output respectively that show the timescale and geometry of convection in the aquifer beneath North Pond.

Text S1. Bathymetric Sampling, Fourier transform specifics, and continuous function for grid construction

We analyzed the bathymetry of seafloor around North Pond in order to develop an analytical equation that could approximate the shape of the upper basement surface. We used 10 m bathymetric data from the field area (Villinger et al., 2014) and extracted profiles in each of the strike-normal (N20E) and strike-parallel (N70W) directions (**Figure S1a**), with sampling every 20 m. Each of the two sets of profiles were combined and subjected to a discrete Fourier transform to determine dominant frequencies of variation, then the strongest six frequencies were retained using an discrete Fourier transform (DFT) to determine the dominant characteristics in each direction (**Figure S1b and S1c**).

This function was found to approximate the shape of the basement surface around and below North Pond sediments:

$$z(x,y) = \frac{1}{t} arctan\left(\frac{t\sin(x)}{1 - tcos(x)}\right) - \frac{1}{t} arctan\left(\frac{\mathrm{t}\sin(y)}{1 - tcos(y)}\right)$$

where *t* determines the “tilt” of the function, *x* is the strike-normal distance, and *y* is the strike-parallel distance. This function was mapped onto x,y,z coordinates that correspond to characteristic normal- and parallel-strike wavelengths and amplitudes around North Pond (**Table S1; Figure S1**).

Text S2. Spatially Varying Heat Flux

We calculated lithospheric heat flux at the base of the simulation domain as:

$$q_{hf} = \frac{C}{\sqrt{age}}$$

where C is an empirically derived constant, t is the age of the crust in My, and q_{hf} is the heat flux in mW/m^2. The value of C has been estimated from numerous studies of global heat flux and bathymetric data to be ~475 to 510 (Parsons and Sclater, 1977; Stein and Stein, 1994; Hasterok, 2013). For simulations in the present study, we used an intermediate value of $C = 500$ mW m^{-2} My$^{-1/2}$, such that heat input varies modestly across two- and three-dimensional domains with lithospheric age (younger to the east, older to the west).

Established cooling models for young oceanic lithosphere are based mainly on a combination on bathymetric and heat flux data. However, heat flux provides a useful constraint in these models only for seafloor older that ~50-65 M.y., because the thermal state of younger ocean lithosphere is known to be impacted by hydrothermal circulation, both on and near seafloor spreading centers and on ridge flanks (Hasterok, 2013; Parsons and Sclater, 1977; Stein and Stein, 1994). As a result, the lithospheric heat flux through young ridge flanks likely has uncertainties on the order of 10% on a global basis, and perhaps up to 20% regionally (because not every ridge flank cools like the global average). Additional uncertainty comes from the possibility that ridge-flank crust may be cooled by earlier phases of deep circulation, followed by a period of conductive rebound years after deep circulation ends (Fisher, 2003; Hobart et al., 1985; Hutnak and Fisher, 2007; Spinelli and Harris, 2011) But even if ridge-crest circulation were to cool the crust to a depth of 5-6 km, rebound to 80-90% of lithospheric should occur by 8 M.y. (the approximate age of the crust below North Pond).

Heat flux data were filtered with a similar approach to other ridge-flank studies where values associated with measurements directly above or adjacent to buried basement highs or outcrops in the sedimented pond (Hutnak et al., 2008). Heat flux values associated with local bathymetric features are likely controlled more by conductive refraction or local advective processes rather than the sediment pond-scale heat transfer processes of this study.

Bathymetric highs were identified from the seismic and sounding data collected from North Pond and points within 750m radius of the local high were removed. 19 heat flux measurements were removed through this process reducing the mean from 56.4 mW/m^2 for the complete dataset to 45.9 mW/m^2 for the filtered dataset. The removal of these data points did not change the overall distribution of the heat flux data (**Figure 1b**).

Text S3. Rayleigh Number Calculation

To get an indication as to the expected occurrence and relatively intensity of convection, we calculated Rayleigh numbers across a range of aquifer thicknesses and permeability values (Figure S4). The Rayleigh is defined for a flat porous medium heated from below as (Ingebritsen and Sanford, 1999):

$$Ra = \frac{\alpha_w \rho_w^2 c_w g k L (T_b - T_t)}{\mu_w K_m}$$

where α_w = thermal expansivity (1/ºC), ϱ = density of the fluid (kg/m^3), c_w = heat capacity of the fluid (J/kg ºC), g = gravitational acceleration (m/s^2), k = permeability (m^2), L = aquifer thickness (m), T_b = temperature at aquifer base (ºC), T_t = temperature aquifer top (ºC), μ_w = fluid viscosity (Pa-s), and K_m = thermal conductivity of the saturated medium (W/m ºC).

These results provided an approximate Rayleigh number for comparison with numerical results presented in this study because the latter includes irregular geometries, incomplete sealing by sediments, and fluid properties that vary with pressure and temperature. For a closed, flat box with fixed upper and lower temperatures, the critical Rayleigh number that results in the onset of convection is Ra-c = 4π2 (~39.5), whereas for an open upper boundary and fixed heat flux at lower boundary, Ra-c = 17.65 (Nield, 1968).

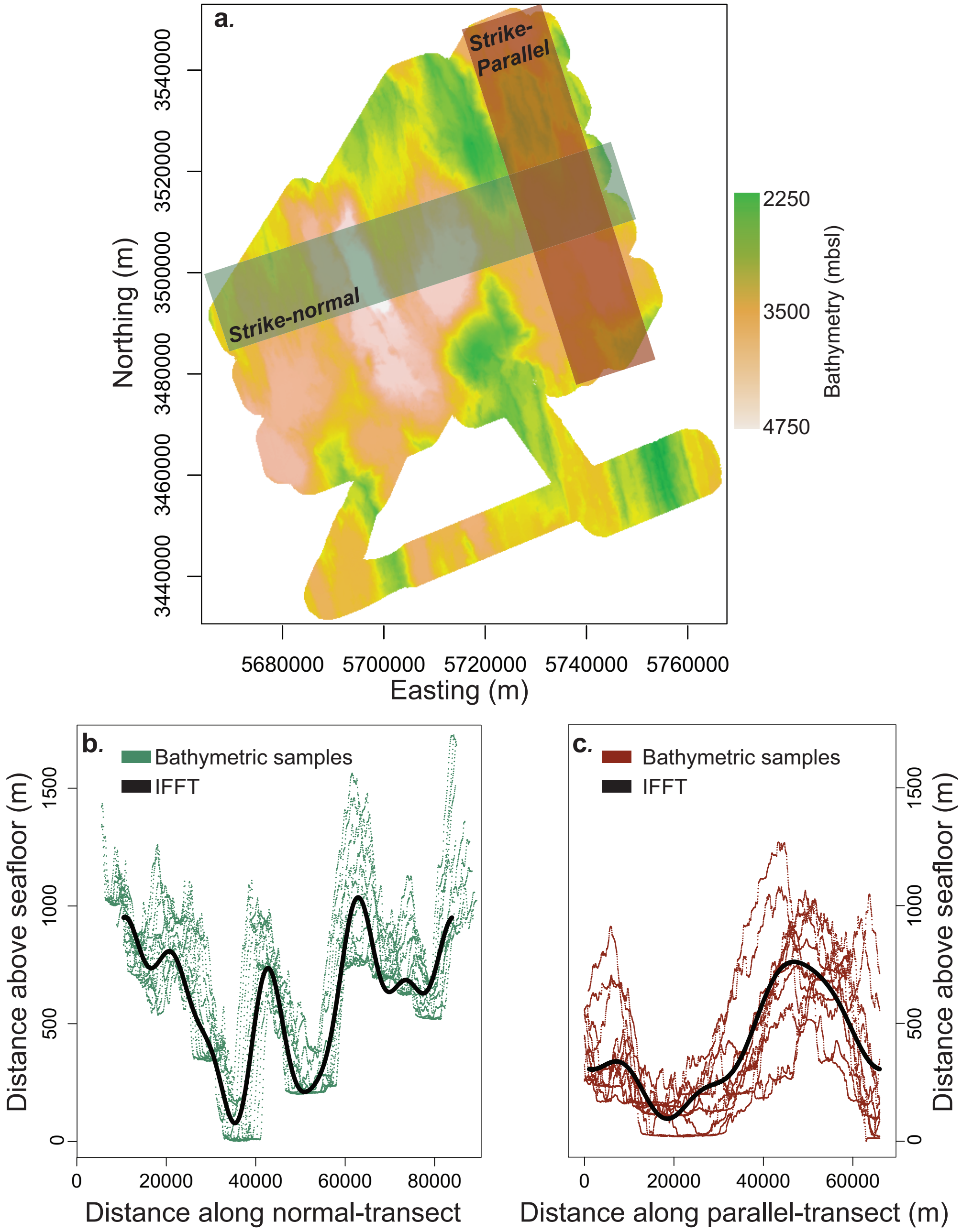

Figure S1. Regional North Pond bathymetric sounding data from *Villinger et al., 2018* and results of (DFT) analysis. **a.** Regional North Pond bathymetry overlain with transects used to sample bathymetric data in strike-normal and strike-parallel directions (shaded in green and brown, respectively). **b.** Strike-normal bathymetric transect data in green DFT results in black. **c.** Strike-parallel bathymetric transect data in brown with DFT results in black.

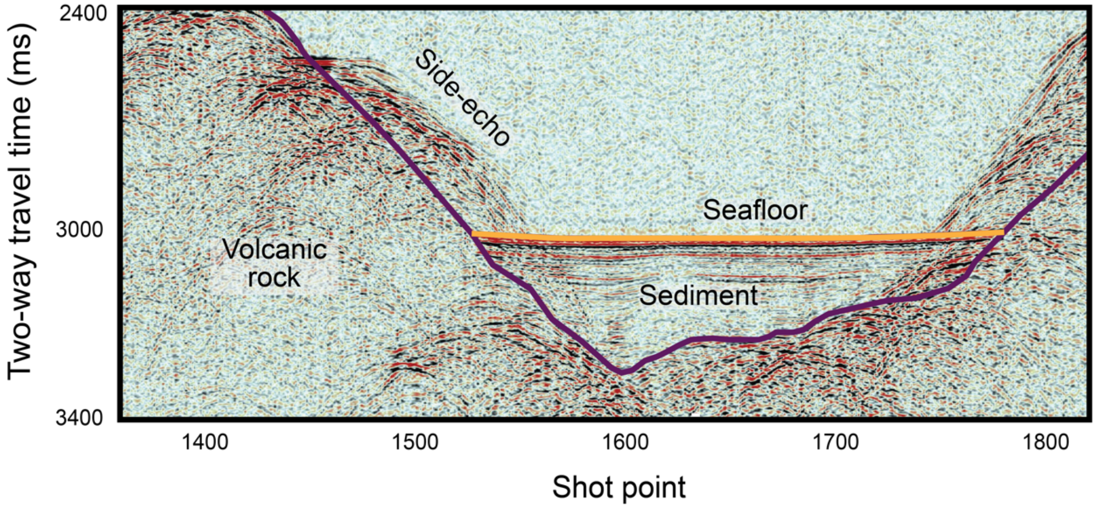

Figure S2. Seismic profile SCS-14 (*Schmidt-Schierhorn et al., 2012*) was used as the basis for two-dimensional simulations. The horizons are seafloor above North Pond sediments (orange), sediment-basement and seawater-basement (purple). Side echoes were inferred because sub-horizontal sediment (seafloor) reflectors defining the top of North Pond extend into the sloping side reflections.

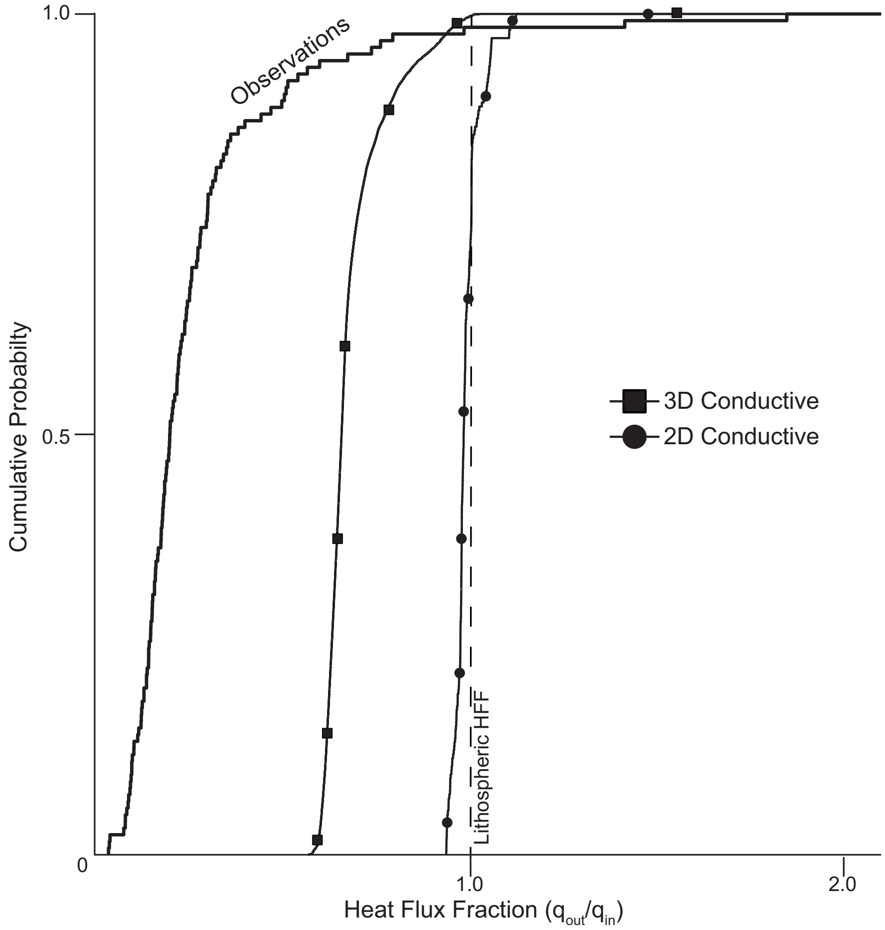

Figure S3. Empirical cumulative distribution plot of heat flux fraction for observations (solid thick line) and results from two- and three-dimensional conductive simulations (filled circles and filled squares respectively).

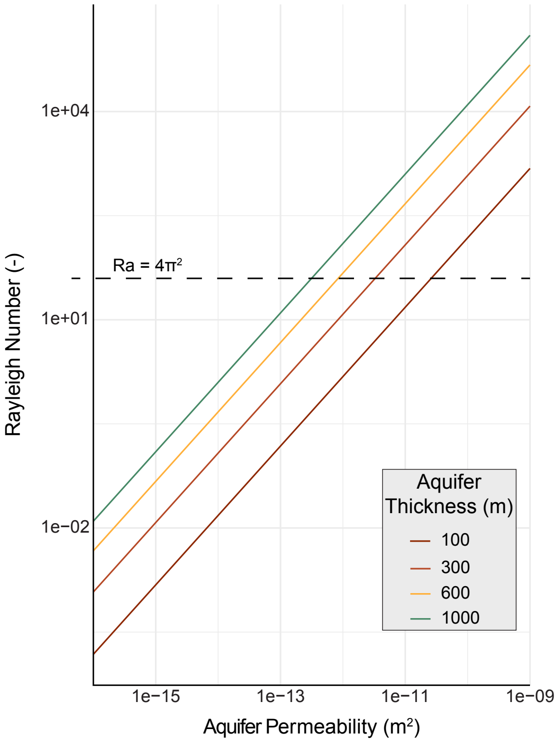

Figure S4. Calculated Rayleigh number as a function of aquifer permeability for aquifer thicknesses: 100 m (brown), 300 m (orange), 600 m (yellow) and 1000 m (green) for a flat domain. Dashed line marks critical Rayleigh number for a flat box sealed at top and bottom and heated from below, Ra-c = $4\pi^2$. This is an approximation for the present study, with irregular geometry, incomplete sealing of the upper boundary, and fluid properties that vary with pressure and temperature.

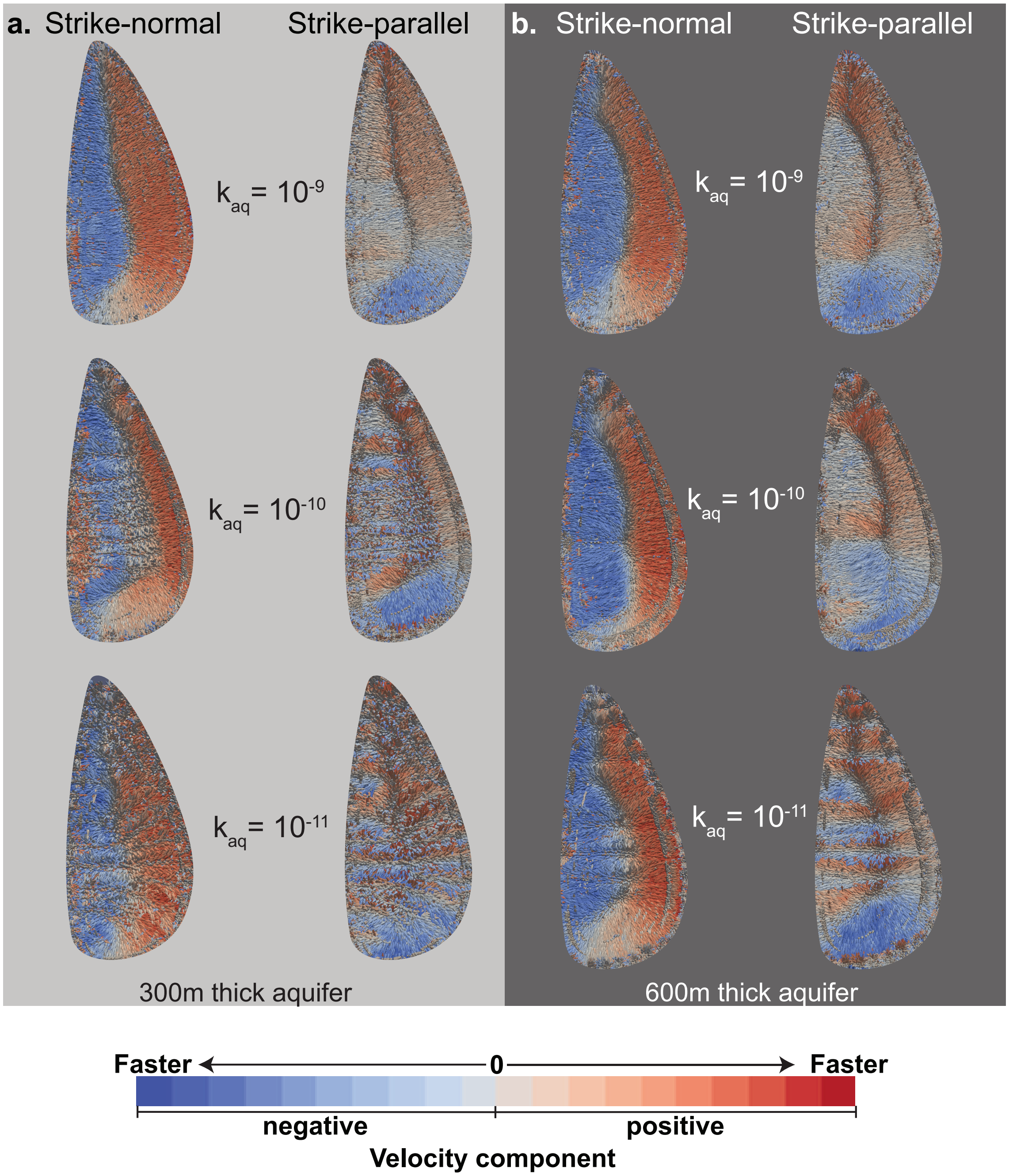

Figure S5. Representations of fluid flow vectors in the upper basement aquifer below North Pond sediment for simulations having a crustal aquifer thickness of (a) 300m – left and (b) 600m - right. Aquifer permeability values as noted ($k_{aq} = 10^{-11}$ to 10^{-9} m^2). Vectors are colored to highlight differences in flow direction, with red being in the positive vector component direction (E or N for strike normal and strike parallel, respectively) and blue being for flow in the negative vector component direction (W and S for strike normal and strike parallel, respectively).

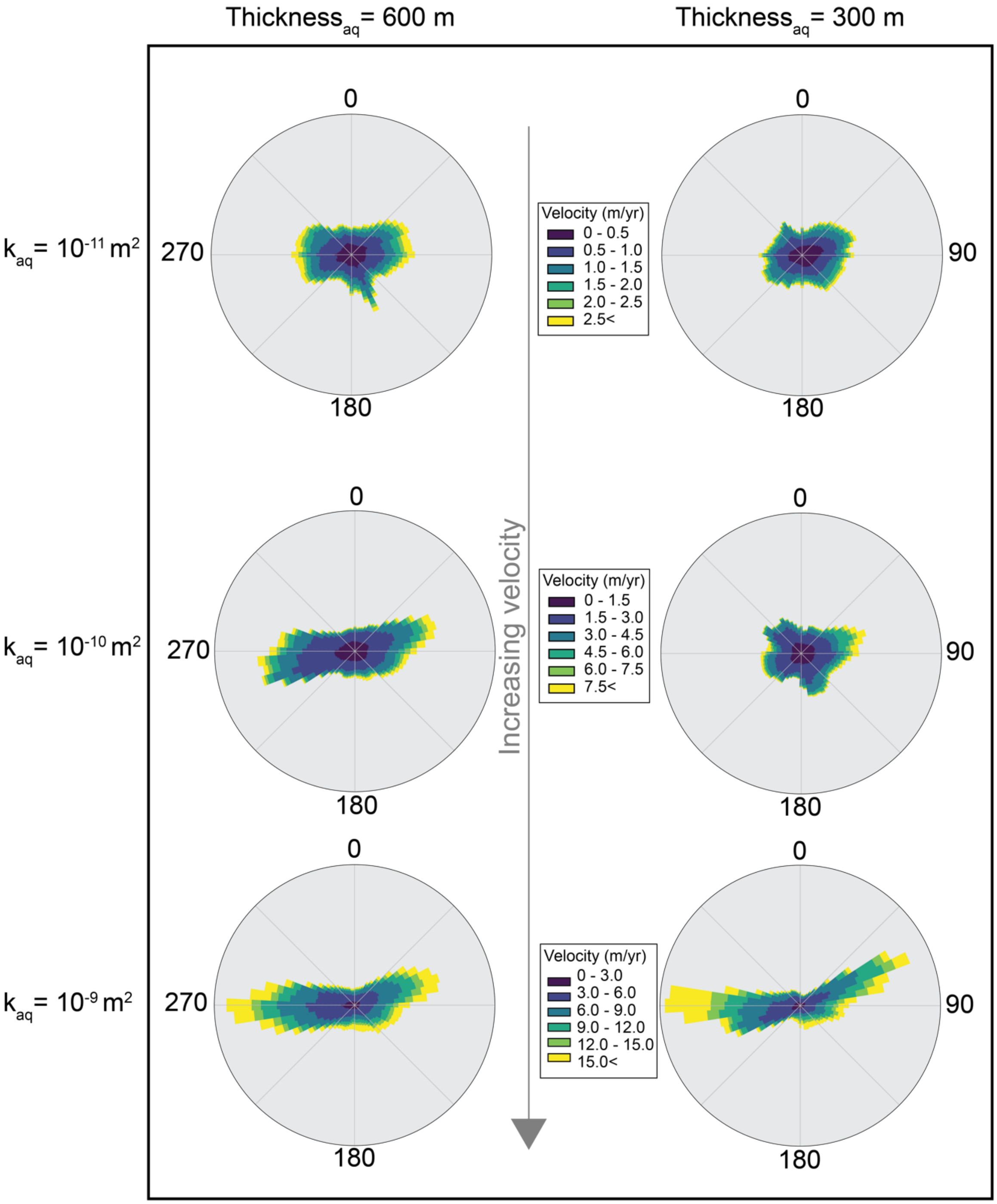

Figure S6. Rose diagrams of specific discharge for all flow vectors in aquifer layer below North Pond in three-dimensional simulations having an aquifer thickness of 300 m and 600 m, and aquifer permeability of $k_{aq} = 10^{-11}$ to 10^{-9} m^2. Note different color scales for different permeability values.

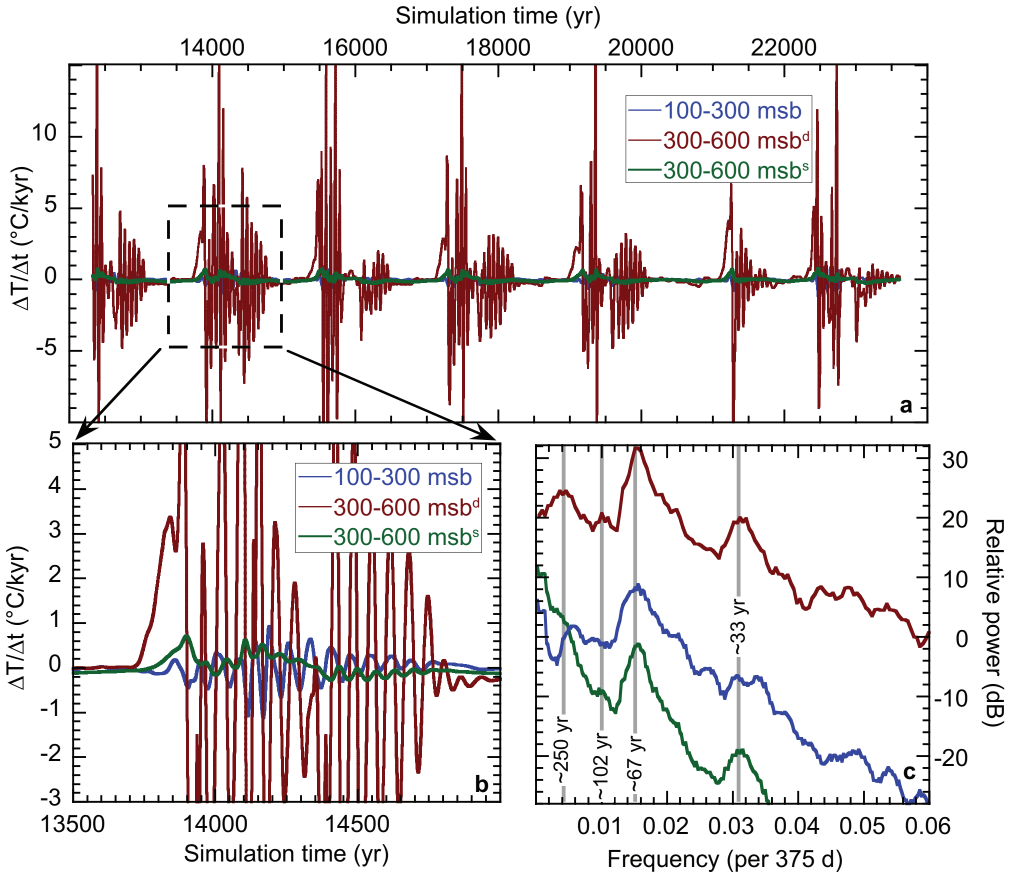

Figure S7. Temperature changes observed in aquifer beneath North Pond and resulting power spectral density analysis. **a.** Plot of change in temperature per change in time ($\Delta T/\Delta t$) versus time for 12,000 yrs. for aquifer thickness of 600 m and nodes located near the west side of North Pond (location shown with star in **Figure 7** in main paper). Selected nodes are located in 100-300 meters below seafloor (mbsf) in blue, 300-600 mbsf in red, and 300-600 mbsf in green. Time indicated by dashed box shown in detail in **Figure S7b**. **b.** Detail plot of 1,500 yr. of data shown in Figure S7a. **c.** Power spectral density analysis of data shown in **Figure S7a**, highlighting periods with relatively high power. Simulations were run with 25 d timesteps, to aid in numerical stability, and frequencies are calculated relative to intervals of 375 d, approximately 1 year.

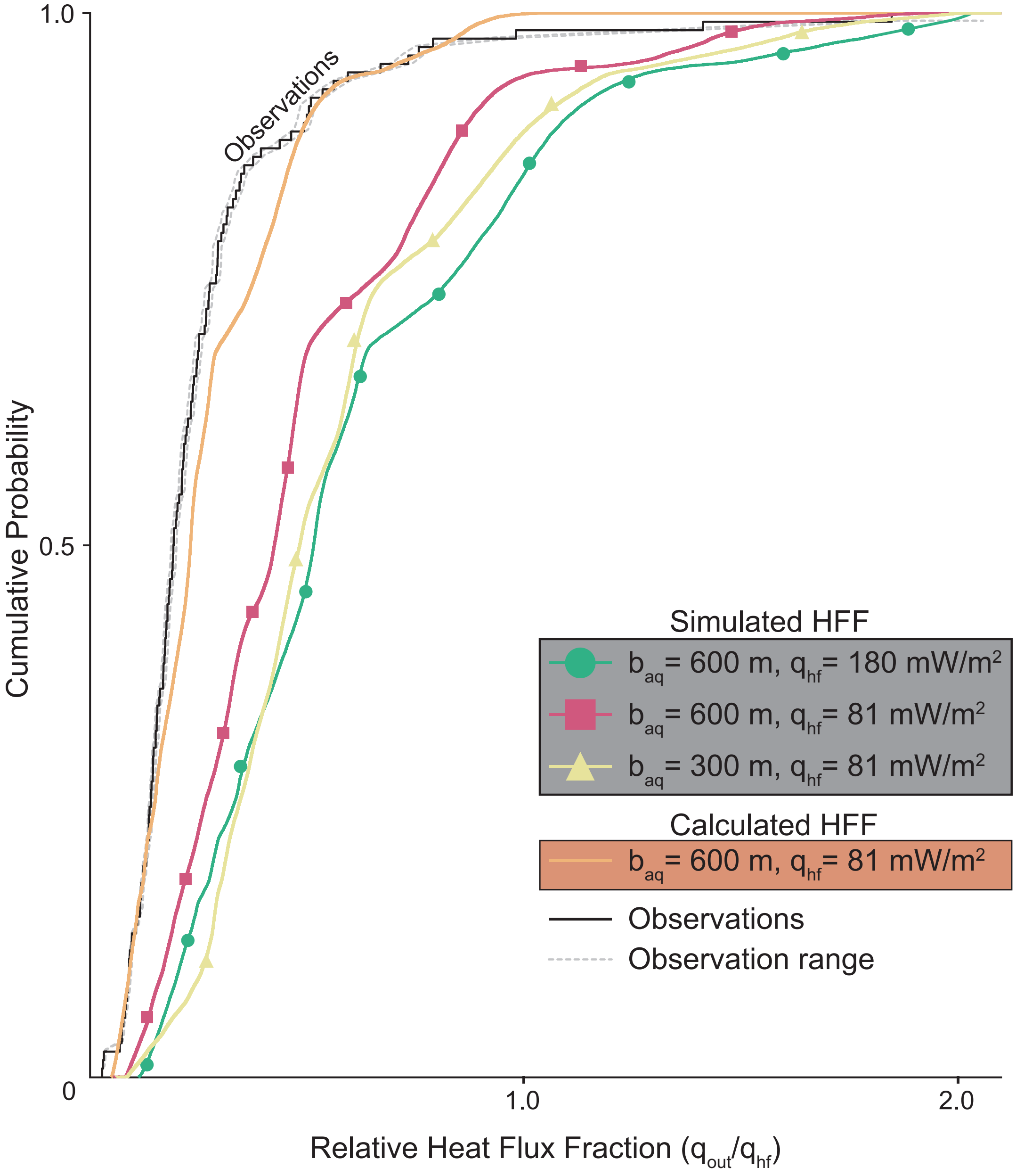

Figure S8. Empirical cumulative distribution plot (ECDF) of relative heat flux fraction (q_{out}/lithospheric input) for observations and simulation results for aquifer thickness 300 m and 600 m with aquifer permeability $k_{aq} = 10^{-9}$ m^2, and normal heat input at base of domain (green curve and dots). Results are compared for the same simulation with heat input that is 55% lower (red line and squares) and for low heat input with a 300 m aquifer (yellow line and triangles). Finally, results are shown for the output of 600 m simulation with full heat input, with results scaled by 55% (orange no marker), and observations of heat flux from North Pond sediments. Observations from North Pond are solid black line and observational ranges are in dashed grey lines.

Table S1. Geometric constraints from text S1.

Property	Value	Source
Strike parallel (SP) pond length	14 km	Bathymetric data
Strike normal (SN) pond length	8 km	Bathymetric data
Shallow slope in pond	5%	Seismic profile SCS-14
Steep slope in pond	15%	Seismic profile SCS-14
Sediment thickness	≤200 m	Seismic profile SCS-14
Strike-parallel topographic wavelength	50 km	Bathymetric data
Strike-normal topographic wavelength	20 km	Bathymetric data
Topographic relief	1000 m	Bathymetric data

Table S2. Flow rates (specific discharge) for aquifer thickness b= 100 m -1000m and aquifer permeability k_{aq} = 10-^{11} to 10^{-9} m^2.

Aquifer thickness (m)	**Aquifer permeability (m^2)**	**Median specific discharge (m/yr) Median (Min – Max)**
100	$k_{aq}= 10^{-11}$	1.9e-1 [7.5e-4 to 1.1e1]
	$k_{aq}= 10^{-10}$	1.9e-1 [4.7e-4 to 9.2]
	$k_{aq}= 10^{-9}$	5.3 [2.2e-2 to 2.6e2]
300	$k_{aq}= 10^{-11}$	7.6e-1 [2.8e-3 to 1.2e1]
	$k_{aq}= 10^{-10}$	2.2 [4.3e-2 to 6.3e1]
	$k_{aq}= 10^{-9}$	7.5 [7.7e-2 to 3.1e2]
600	$k_{aq}= 10^{-11}$	8.2e-1 [8.2e-7 to 1.7e1]
	$k_{aq}= 10^{-10}$	2.3 [8.1e-7 to 5.8e1]
	$k_{aq}= 10^{-9}$	6.7 [6.9e-7 to 2.5e2]
1000	$k_{aq}= 10^{-11}$	9.4e-1 [2.1e-2 to 1.3e1]
	$k_{aq}= 10^{-10}$	2.3 [5.1e-2 to 6.1e1]
	$k_{aq}= 10^{-9}$	--

Movie S1.
Animation of two-dimensional quasi-steady state North Pond simulation for $k_{aq} = 10^{-9}$ and 600 m crustal aquifer thickness. Steps between frames are 1e5 years for a total time of 1.2e6 years. Velocity vectors are colored by magnitude and direction. The background contour plot is of temperature within the aquifer layers.

Movie S2.
Animation of three-dimensional quasi-steady state North Pond simulation for $k_{aq} = 10^{-9}$ and 600 m crustal aquifer thickness. Steps between frames are 10 years for a total time of 2000 years. The locations of the across-strike transects are 6000 m, 7000 m, 8000 m and 10000 m and the along-strike transect is at -7000 m. All of these locations are based on the entire domain coordinates and can be referenced to the sediment pond via the red lines on the generalized pond in the upper left. Velocity transects at 6000 m and 8000 m show vectors oriented in the X-Z (across-strike and vertical) velocity components and are colored and scaled by magnitude and direction. The remaining transects (7000 m, 10000 m, and -7000 m) are all contour plots of temperature within the aquifer layers beneath the sedimented pond.

References

Fisher, A.T. (2003). Geophysical Constraints on Hydrothermal Circulation Observations and Models. In *Energy and mass transfer in submarine hydrothermal systems* (pp. 29–52).

Hasterok, D. (2013). A heat flow based cooling model for tectonic plates. *Earth and Planetary Science Letters*, *361*, 34–43. https://doi.org/10.1016/j.epsl.2012.10.036

Hobart, M., Langseth, M., & Anderson, R. N. (1985). A Geothermal and Geophysical Survey on the South Flank of the Costa Rica Rift: Sites 504 and 505. https://doi.org/10.2973/DSDP.PROC.83.122.1985

Hutnak, M., & Fisher, A. T. (2007). Influence of sedimentation, local and regional hydrothermal circulation, and thermal rebound on measurements of seafloor heat flux. *Journal of Geophysical Research: Solid Earth*, *112*(B12). https://doi.org/10.1029/2007JB005022

Hutnak, M., Fisher, A., Harris, R. *et al*. (2008) Large heat and fluid fluxes driven through mid-plate outcrops on ocean crust. *Nature Geosci* **1,** 611–614. https://doi.org/10.1038/ngeo264

Ingebritsen, S. E., & Sanford, W. E. (1999). *Groundwater in Geologic Processes*. Cambridge University Press.

Langseth, M. G., von Herzen, R. P., Becker, K., Müller, P., & Villinger, H. (2018, November 21). Heat Flux in Sedimented Ponds, MAR-flanks 22-24□N, RV Atlantis II 123-2, 1989. PANGAEA. https://doi.org/10.1594/PANGAEA.896168

Nield, D. A. "Onset of Thermohaline Convection in a Porous Medium." Water Resources Research 4, no. 3 (1968): 553–60. https://doi.org/10.1029/WR004i003p00553.Parsons, B., & Sclater, J. G. (1977). An analysis of the variation of ocean floor bathymetry and heat flow with age. *Journal of Geophysical Research*, *82*(5), 803–827. https://doi.org/10.1029/JB082i005p00803

Schmidt-Schierhorn, F., Kaul, N., Stephan, S., & Villinger, H. (2012). Geophysical site survey results from North Pond (Mid-Atlantic Ridge). In Edwards, K.J., Bach, W., Klaus, A., and the Expedition 336 Scientists, Proc. IODP, 336: Tokyo (Integrated Ocean Drilling Program Management International, Inc.). https://doi.org/10.2204/iodp.proc.336.107.2012

Spinelli, G. A., & Harris, R. N. (2011). Effects of the legacy of axial cooling on partitioning of hydrothermal heat extraction from oceanic lithosphere. *Journal of Geophysical Research: Solid Earth*, *116*(B9). https://doi.org/10.1029/2011JB008248

Stein, C., & Stein, S. (1994). Constraints on Hydrothermal Heat-Flux Through the Oceanic Lithosphere from Global Heat-Flow. *Journal of Geophysical Research-Solid Earth*, *99*(B2), 3081–3095. https://doi.org/10.1029/93JB02222

Villinger, H., Strack, A., Gaide, S., & Thal, J. (2018). Gridded bathymetry of North Pond (MAR) from multibeam echosounder EM120 and EM122 data of cruises MSM20/5 (2012) and MSM37 (2014) [Data set]. *Department of Geosciences, Bremen University*. PANGAEA. https://doi.org/10.1594/PANGAEA.889439

Appendix B: Supplemental Information for "Construction of Geologically Realistic, Three-Dimensional Meshes for Simulation of Subseafloor Hydrothermal Circulation, Including Bathymetric Relief and Patchy Sediment"

Introduction

This tutorial is a resource that accompanies a robust set of resources including a publication, psuedo-code, GitHub repository, and data repository for constructing a three-dimensional grid of geologically realistic representations of seafloor crustal relief. The three-dimensional simulation domain described here has been used in multiple publications focusing on the thermal and hydrogeologic regime of coupled fluxes beneath a marine sediment pond (Price et al., 2022; Price et al., *in review*).

The tutorial can be broken down into a workflow consisting of 5 main sections: constructing surfaces, constructing a domain, refining the domain, defining and assigning material types to regions, and a general clean-up of the domain. There will be two examples included for each step. One example will use a general case that will introduce the concepts in a simple manner and the other example will be for construction of the North Pond domain.

This tutorial will not be an exhaustive tutorial on the functionality of LaGriT as there are many examples that can be found online (https://lanl.github.io/LaGriT/pages/tutorial/index.html). Instead, this tutorial will serve as walkthrough; that allows the user to understand the steps used in construction of this simulation domain using the lessons and approaches explained below.

Happy gridding!

Data and software requirements

To complete this tutorial, you will need a stable version of LaGriT (version) and optionally Paraview.

LaGriT

LaGriT is available at https://github.com/lanl/LaGriT/releases and can be downloaded as a compiled version (preferred) or the source code for compiling. After downloading LaGriT, add the file to a location within your path, and modify the file permissions to executable.

Paraview (optional)

Paraview is a powerful visualization platform used for the primary grid viewer in this tutorial. Graphics here will be provided inline so there is no need to download for the purpose of this tutorial, but it is recommended to explore the full functionality of this workflow. Paraview can be downloaded athttps://www.paraview.org/download/

Data files

This tutorial utilizes scripts and data files from a GitHub repository that can be found at https://github.com/adamnicholasprice/GeologicGriddingData. This repository can be cloned via the command line or downloaded directly from the GitHub website. There are four directories:

- GeneralLaGriT - LaGriT scripts and csv surfaces for building the general grid case
- GeneralScene - Paraview scene files for general grid case used in this tutorial

- NorthPondLaGriT - LaGriT scripts and csv surfaces for building the North Pond grid case
- NorthPondScene - Paraview scene files for North Pond grid case used in this tutorial

Document styling, commands, and files

Document style

Throughout the document *italicized words* will denote either a file name or a variable within LaGriT.

Code blocks will be denoted by the following style:

```
>_ Code here
```

Commands

In lieu of repeating this code chunk in each of the following steps in the tutorial, any LaGriT input files (.lgi) that are run in the tutorial are done so by executing the following command in the command line:

```
>_ lagrit < filename
```

This will be denoted with the phrase execute *filename.lgi* in LaGriT.

Steps within the tutorial will be broken down by LaGriT file and have necessary inputs and outputs specified as such:

Filename	**Input**	**Output**
filename.lgi	*inputFilename*	*outputFilename*

File types

Extension	Filetype	Purpose
_ *.lgi	LaGriT control file	LaGriT input control file, specifies mesh generation.
_ *.mlgi	LaGriT control file	LaGriT input control file used to specify a subroutine within *.lgi file.
_ *.inp	AVS UCD (Unstructured Cell Data) file	Created by LaGriT and contains information about mesh objects. Can be opened in Paraview to visualize data.
_ *.zone*, .area, *.stor*, .fehmn _	FEHM files	LaGriT output files that are of general use but are specifically designed for FEHM porous flow and transport code
_ outx3dgen	LaGriT output file	Output file containing commands and output from commands executed in LaGriT (overwritten every time LaGriT command is called)
_ legx3dgen	LaGriT log file	Log file containing commands executed in LaGriT (overwritten every time LaGriT command is called)

Extension	Filetype	Purpose
_ *.csv	Text file (comma separated values)	In this tutorial, these are text files containing coordinates in meters for surfaces. Columns are x, y, z coordinates respectively.

Getting started

Before starting this tutorial make sure that LaGriT is executable within the working directory of this tutorial and ensure all needed materials have been synced from GitHub.

Surfaces

The first step in the construction of a simulation domain is to construct surfaces that represent geologically realistic layers. These surfaces will define boundaries that allow assignment of specific material properties and act as surfaces to refine the simulation domain. Surfaces can be constructed in LaGriT or in an outside programming language such as R, Python, or MATLAB and brought into LaGriT. In both cases in this tutorial, surfaces were constructed outside of LaGriT and brought in to define mesh objects. The general steps to construct surfaces are:

1. Save mesh coordinates (x,y,z) into a .csv file
2. Create mesh object that has coordinate system (x and y) of desired mesh resolution (have to define if different from .csv file coordinates)
3. Connect mesh objects with new coordinates in x and y.
4. Read in the .csv as a mesh object into LaGriT
5. Copy over z-coordinates from mesh in step 4 to connected mesh in step 2

This process forces LaGriT to make the “best” connections within an x-y plane to begin with and then the coordinates along the z-axis with relief to be defined, thereby preventing any connections outside the plane.

Generalized Mesh

For the general case, there is one control file (.lgi), one input file (*surface.lgi*), and four output surfaces.

Filename	**Input**	**Output**
1_create_surface.lgi	*surface.csv*	*1_surface_aq200.inp*
		1_surface_aq800.inp
		1_surface_zero.inp
		1_surface.inp

Overview

For the general case, *surface.csv* is the continuous function;

$$z(x, y) = -cos(x) - cos(y)$$

that replicates, but generalizes topography associated with topographic relief and a topographic low. The maxima of the function would be representative of seamounts or hills, whereas the minima would represent sediment ponds or a sedimented valley bottom, both common features on the earths surface.

Syntax

First, navigate to the directory for the general case

(i.e., GeologicGriddingData/GeneralLaGriT)

Next, execute the .lgi file

```
>_ lagrit < 1_create_surface.lgi
```

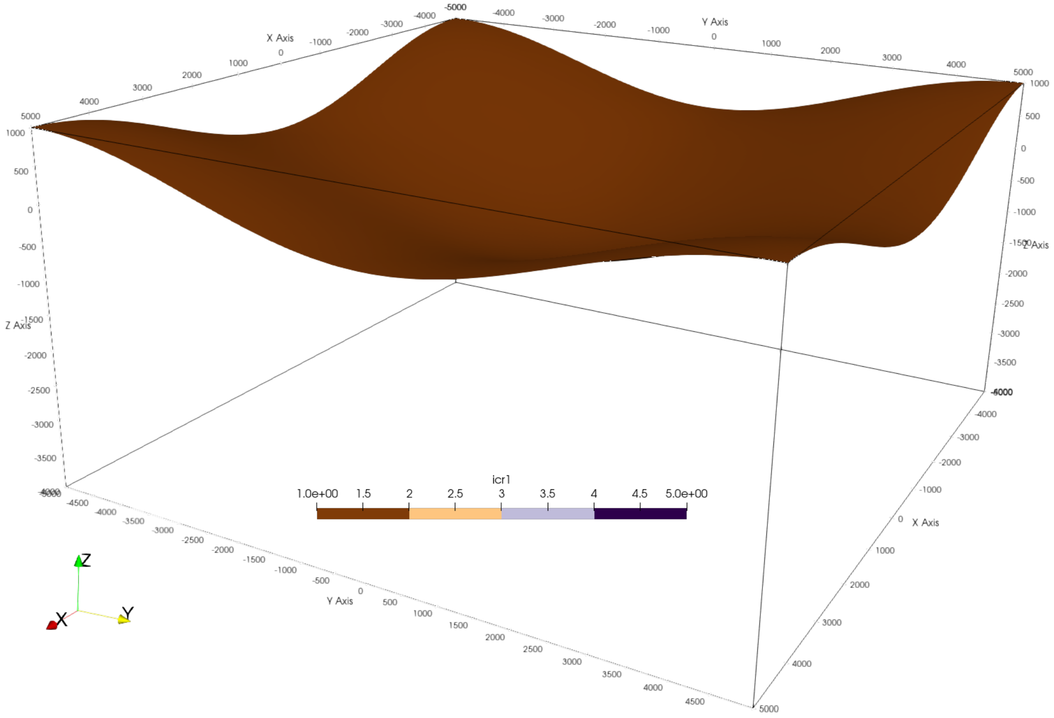

Figure B-1: Surface 1_surface.inp representing the initial surface used for topographic relief. The surface is outlined by the eventual domain and shows the extent and relief of our initial surface.

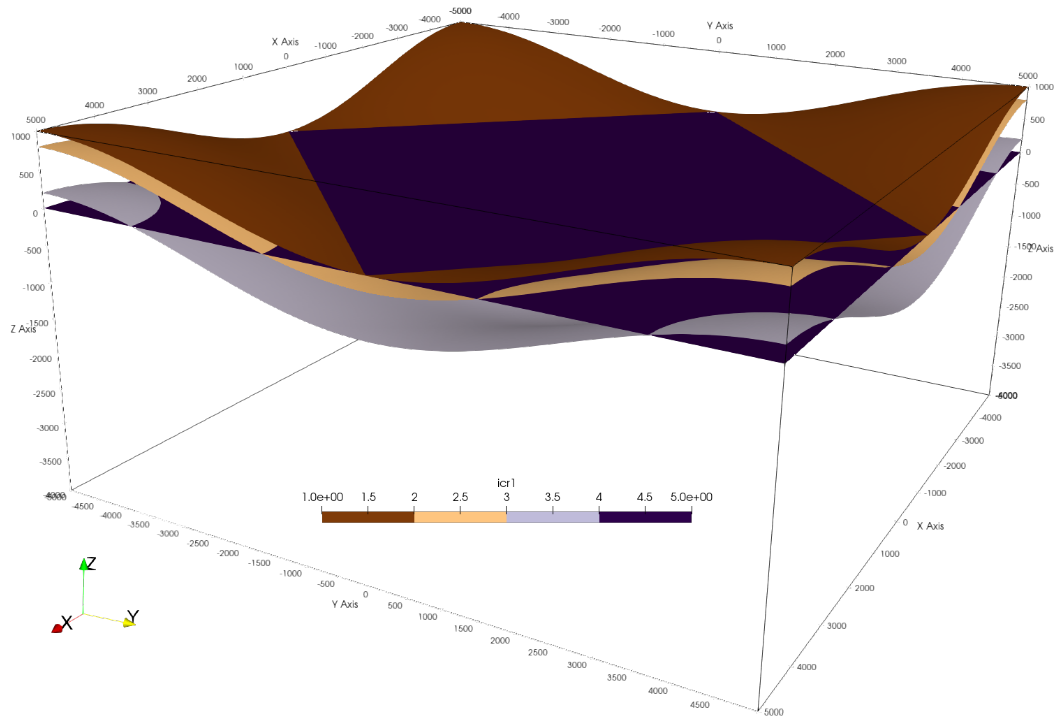

Figure B-2: All the surfaces output from *1_surface.inp*. Surfaces represent the upper most topography, layers at 200 and 800m below surface, and a surface at 0m. These surfaces will surface as boundaries for refinement as well as assigning materials to the simulation domain.

North Pond

For the North Pond case, the first seven .lgi files define surfaces. The initial surface that represents the regional bathymetry of North Pond, was constructed outside of LaGriT in R. The details of sampling data for surface construction can be found in section 3 of this publication or in the supplemental information here Price et al., 2022.

From samples of bathymetric data surrounding North Pond, a continuous function that best describes the region is:

$$z(x, y) = \frac{1}{t}\arctan\left(\frac{t * \sin(x)}{1 - t * \cos(x)}\right) - \frac{1}{t}\arctan\left(\frac{t * \sin(y)}{1 - t * \cos(y)}\right)$$

where t determines the “tilt” of the function, x is the strike-normal distance, and y is the strike-parallel distance. The inital surface is defined from -10 to 10 in the x and y directions.

Filename	**Input**	**Output**
1_surf_domain.lgi	*function6.csv*	*1_surf_domain.inp*

Overview

Create mesh object surface representing North Pond bathymetry using function6.csv. The surface created above is brought into LaGriT and assigned a new coordinate system that assigns the correct slopes to the areas of interest. This new coordinate system is from -75 km to 75 km along-strike, -30 km to 30 km in the across-strike direction, with an amplitude of 600 m.

Syntax

Navigate to the directory for the North Pond mesh case

```
>_ lagrit < 1_surf_domain.lgi
```

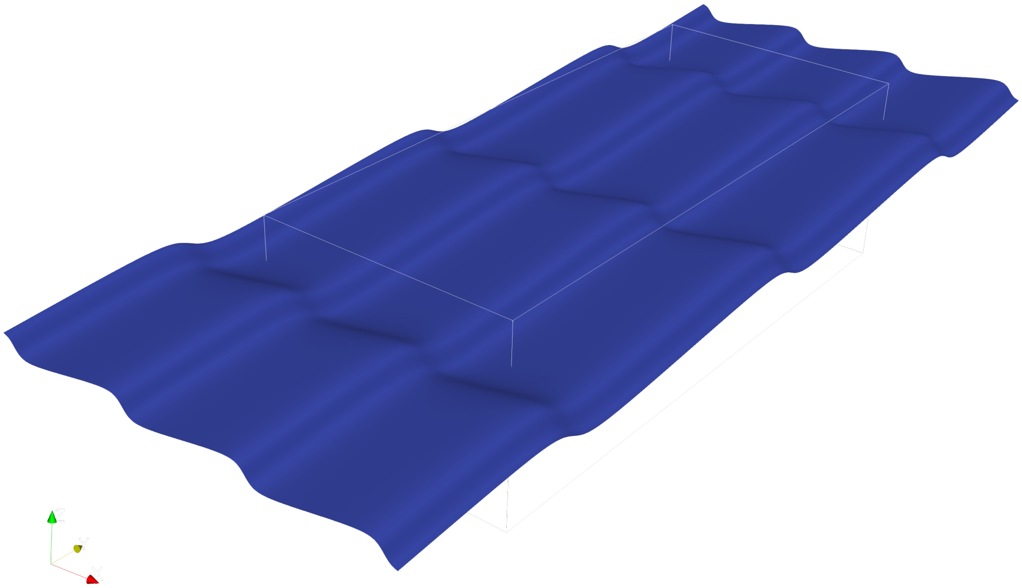

Figure B-3: Initial North Pond surface with 4x vertical exaggeration

Filename	**Input**	**Output**
2_surf_mid_grid.lgi	*2_middle_grid.csv*	*2_surf_mid_grid.inp*

Overview

Create mesh object surface from trimmed area of interest created from truncated bathymetric surface (*2_middle_grid.csv*) representing North Pond and immediately adjacent region.

Syntax

```
>_ lagrit < 2_surf_mid_grid.lgi
```

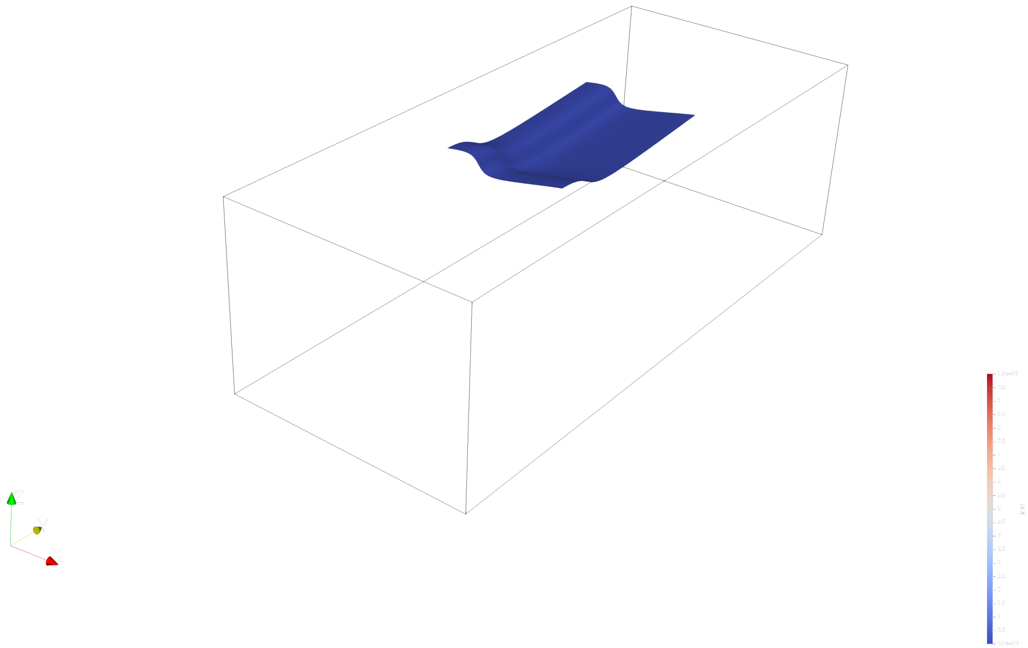

Figure B-4: Surface *2_surf_mid_grid.inp*, representing a subset of the initial surface above just in the area and immediately adjacent to North Pond with 4x vertical exaggeration.

Filename	**Input**	**Output**
3_surf_mid_sb.lgi	*3_middle_sb.csv*	*3_surf_mid_sb.inp*

Overview

Create mesh object surface from trimmed area of interest created from truncated bathymetric surface (*3_middle_sb.csv*) representing sediment / basement interface beneath North Pond.

Syntax

```
>_ lagrit < 3_surf_mid_sb.lgi
```

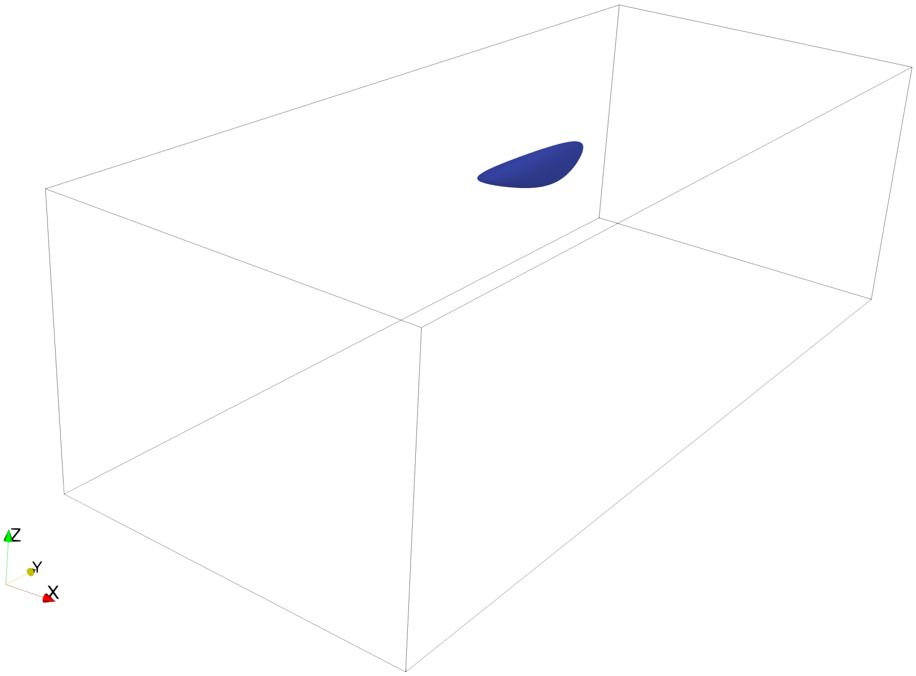

Figure B-5: Surface *3_surf_mid_sb.inp*, representing the sediment-basement contact directly below the sedimented pond in North Pond with 4x vertical exaggeration

Filename	**Input**	**Output**
4_surf_flat_zero.lgi	*None*	*4_surf_flat_zero.inp*

Overview

Construct a flat surface at z = 0 at the same spatial extent as *2_middle_grid.csv* just in the area of and immediately adjacent to North Pond.

Syntax

```
>_ lagrit < 4_surf_flat_zero.lgi
```

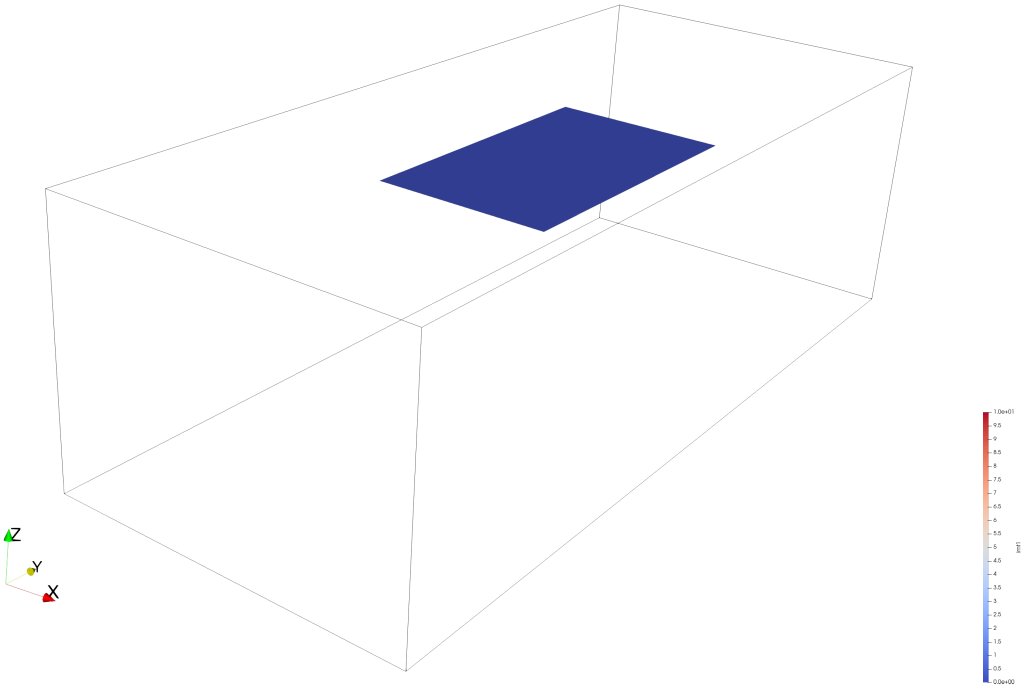

Figure B-6: Surface *4_surf_flat_zero.inp*, in the area of and immediately adjacent to North Pond.

Filename	**Input**	**Output**
5_surf_aq100.lgi	*3_surf_mid_sb.inp*	*5_surf_aq100.inp*

Overview

Construct a volume that represents a 100m thick aquifer section directly beneath the sediment-basement contact of North Pond with the same extent as *3_surf_mid_sb.inp*

Syntax

```
>_ lagrit < 5_surf_aq100.lgi
```

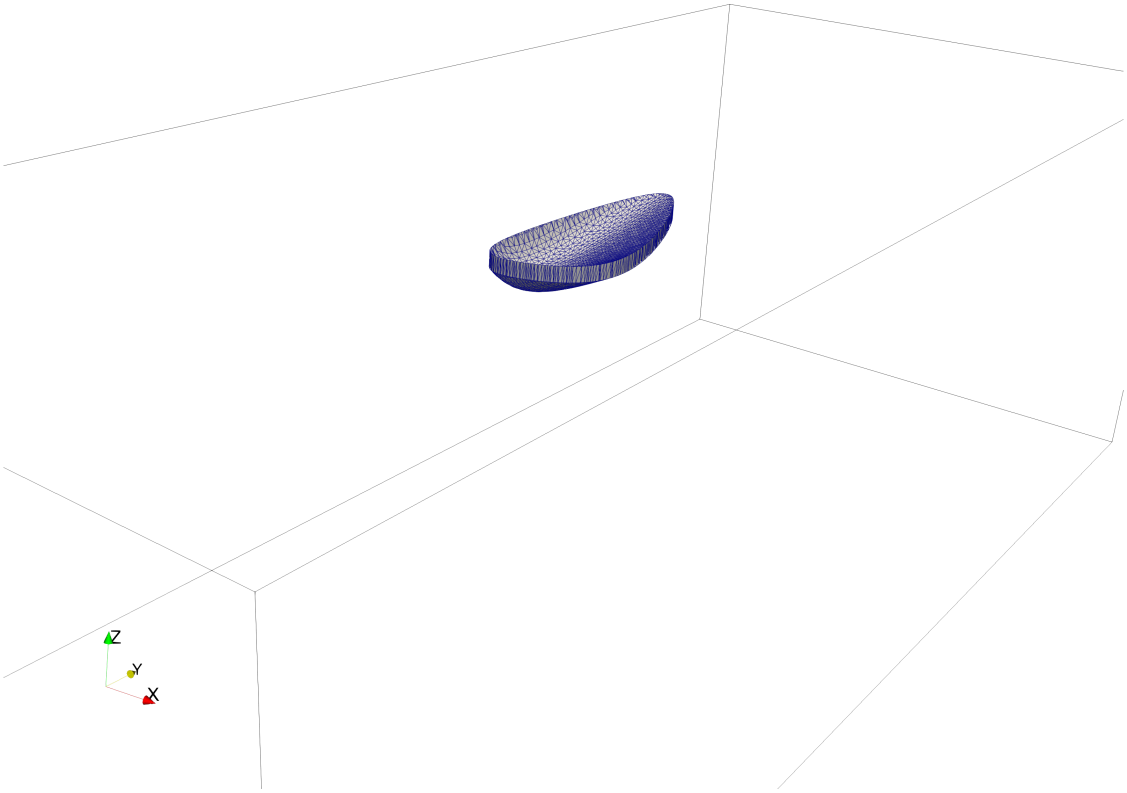

Figure B-7: Volume 5_surf_aq100.inp, representing a 100m thick aquifer section below North Pond 10x vertical exaggeration.

Filename	**Input**	**Output**
6_surf_aq300_1k.lgi	*2_surf_mid_grid.inp*	*6_surf_aq300_1k.inp*

Overview

Construct a volume that represents a 900 m thick aquifer section from the base of the 100m thick aquifer to the base of the 1000m thick aquifer directly beneath and adjacent to the region representing North Pond.

Syntax

```
>_ lagrit < 6_surf_aq300_1k.lgi
```

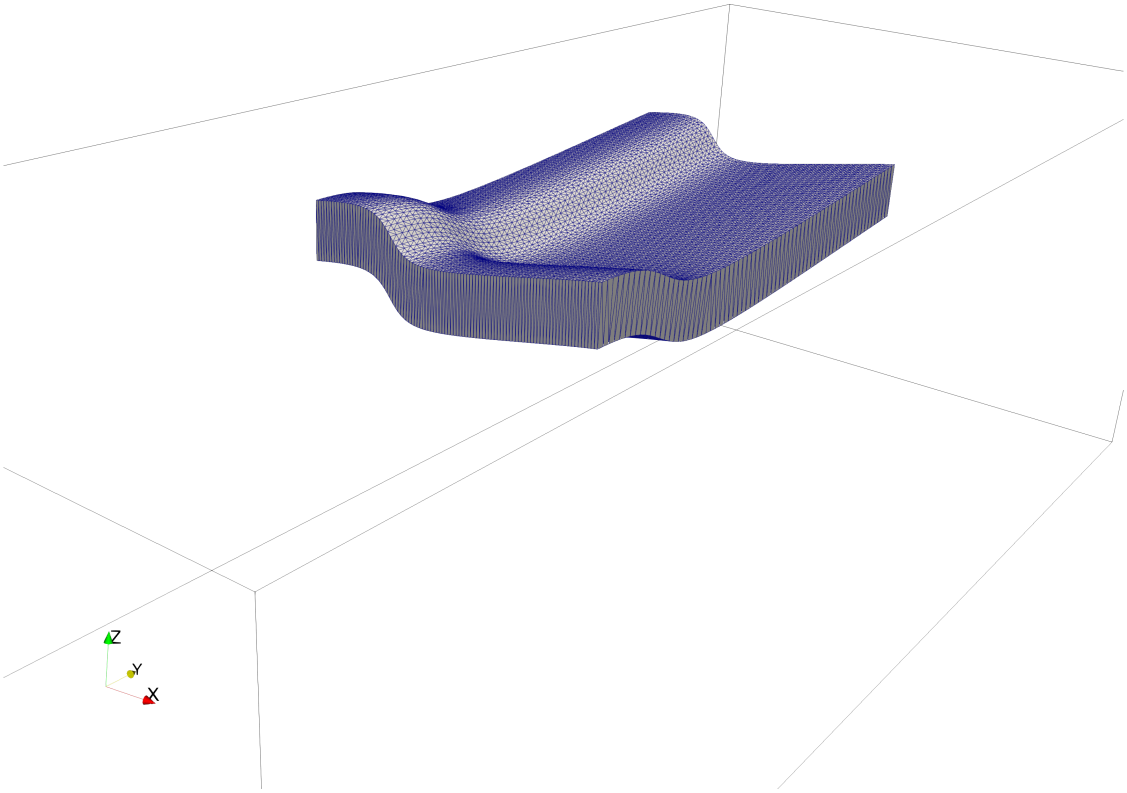

Figure B-8: Volume 6_surf_aq300_1k.inp, representing a 900m thick aquifer section 4x vertical exaggeration.

Filename	**Input**	**Output**
7_surf_filt.lgi	*1_surf_domain.inp*	*7_surf_filt_aq100.inp*
		7_surf_filt_aq300.inp
		7_surf_filt_aq600.inp
		7_surf_filt_aq1k.inp

Overview

Construct surfaces that represent the transitions from: - aquifer 100 m thickness to 200 m thickness (7_surf_filt_aq100.inp) - aquifer 200 m thickness to 300 m thickness (7_surf_filt_aq300.inp) - aquifer 300 m thickness to 400 m thickness (7_surf_filt_aq600.inp) - aquifer 400 m thickness to 500 m thickness (7_surf_filt_aq1k.inp)

```
>_ lagrit < 7_surf_filt.lgi
```

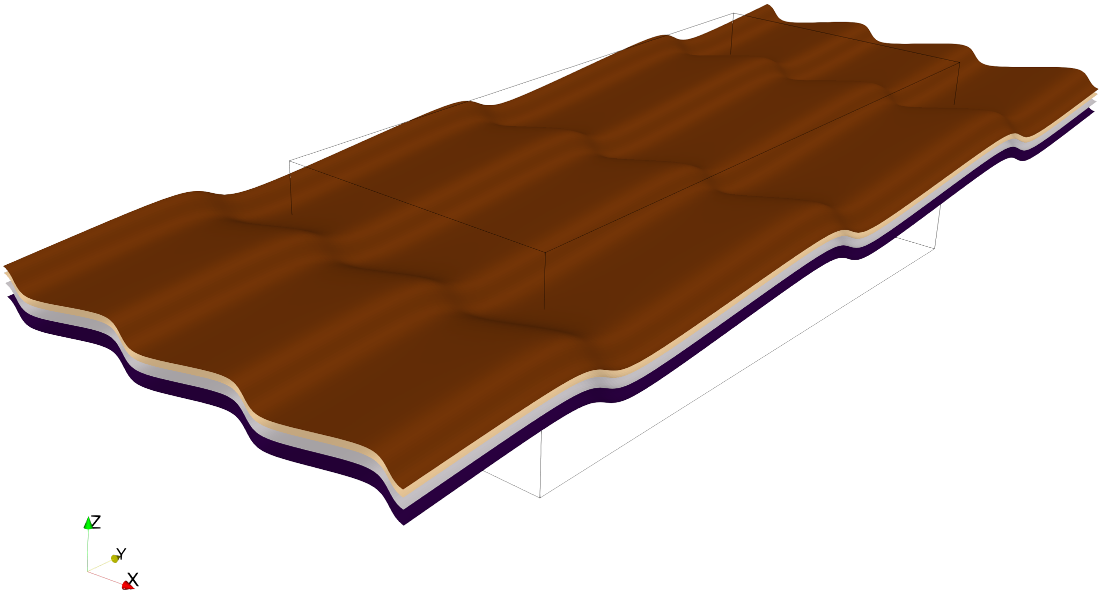

Figure B-9: Surfaces *7_surf_filt_aq100.inp* (brown), *7_surf_filt_aq300.inp* (tan), *7_surf_filt_aq600.inp* (light purple), and *7_surf_filt_aq1k.inp* (dark purple) with 4x vertical exaggeration.

Conclusion

Making surfaces to define material zones corresponding to stratigraphic sections and provide refinement boundaries is the most important and time-consuming step in this process. The final figure shows the 10 surfaces and volumes constructed to define and refined the North Pond mesh.

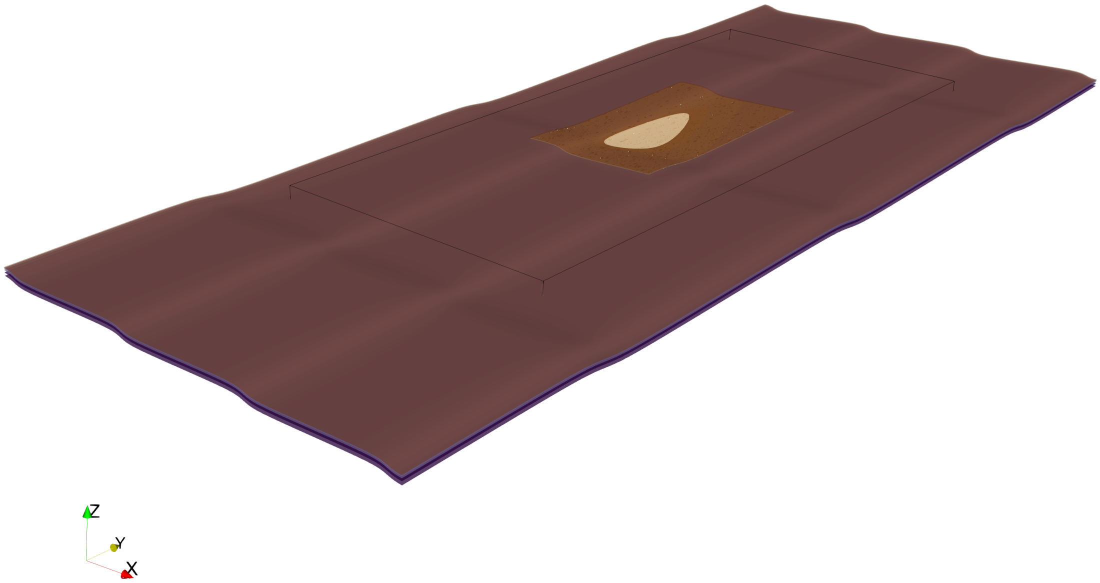

Figure B-10: All surfaces and volumes constructed for North Pond mesh.

Constructing and refining domain

The next step in constructing a mesh is to determine the size, shape, and type of elements that will make up the mesh. In both of the general case, we start with a rectangular mesh composed of hexahedral elements with a coarse geometry. Next, we use the surfaces constructed in the last section to refine the mesh along boundaries of interest. This allows the mesh to have a nested structure that has a high-resolution area in the near-field representing the geologic structure we are interested in simulating and lower-resolution in the far-field. This nested feature also increases computational efficiency of numerical models used to simulate processes using the mesh.

Generalized Mesh

Filename	Input	Output
2_refine_domain.lgi	*1_surface_aq200.inp*	*2_initial_domain.inp*
	1_surface_aq800.inp	*2_hexRefine_octree.inp*
	1_surface.inp	*2_surface_octree.inp*
		2_surfaceAQ200_octree.inp
		2_surfaceAQ800_octree.inp

Overview

For the general case, a rectangular mesh with dimensions 10km x 10km x 5km comprised of hexahedral elements resolution of 1km x 1km x 1km is defined as the initial mesh. Next, the mesh is refined along the surfaces of interest using the following conditionals: 1. One refinement step along the surface, *1_surface.inp* (initial surface, top of domain) 2. Two refinement steps are performed along the surface *1_surface_aq200.inp* (transition of the 200 m thick aquifer layer to the 800 m thick aquifer layer) 3. One refinement step along the surface *1_surface_aq800.inp* (transition from the 800 m thick aquifer layer and the conductive boundary layer at the base of the domain)

Syntax

```
>_ lagrit < 2_refine_domain.lgi
```

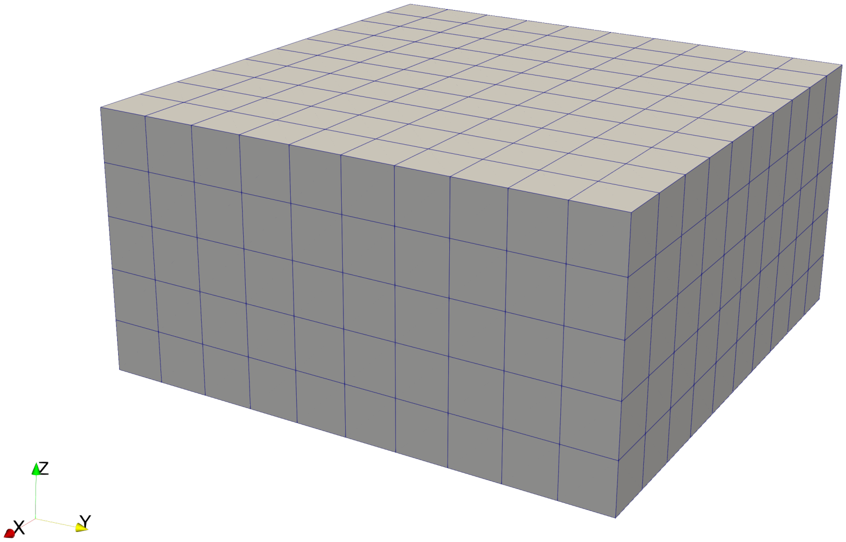

Figure B-11: Initial general case hexahedral mesh

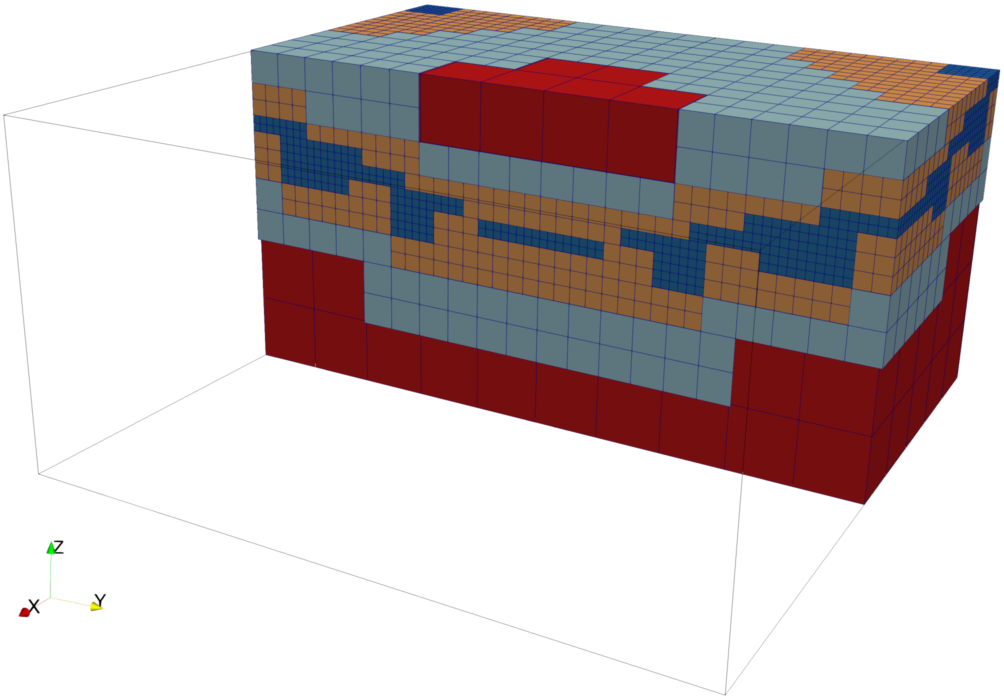

Figure B-12: General domain slice at x=0, showing levels of refinement in areas of interest.

North Pond

Filename	**Input**	**Output**
8_price_driver_high_resolution_clipped.lgi	*1_surf_domain.inp*	*8_inital_hex_domain.inp*
	3_surf_mid_sb.inp	*8_1_octree_NP.inp*
	4_surf_flat_zero.inp	*8_2_octree_aq100.inp*
	5_surf_aq100.inp	*8_3_octree_aq300.inp*
	6_surf_aq300_1k.inp	*8_4_octree_dom.inp*

Filename	Input	Output
	7_surf_filt_aq100.inp	*8_4_octree_domaq100.inp*
	7_surf_filt_aq300.inp	*8_5_octree_domaq1k.inp*
	7_surf_filt_aq600.inp	*8_6_octree_domaq300.inp*
	7_surf_filt_aq1k.inp	*8_7_octree_domaq600.inp*
		8_hex_refine_octree.inp

Overview

For North Pond, a rectangular mesh with 40km x 90km x 7.5km comprised of hexahedral elements with an initial resolution of 1km x 1km x 750m is defined. Refinement using the same subroutine as in the general case is used here with a much more sophisticated set of refinement conditionals. The following steps are taken in the refinement step:

1. One refinement of elements intersecting surface *3_surf_mid_sb.inp* (sediment-basement interface just in North Pond, the area of interest)
2. One refinement of elements intersecting volume *5_surf_aq100.inp* (100 m thick aquifer from seafloor to 100m below surface just below North Pond)
3. Two refinements of elements intersecting volume *6_surf_aq300_1k.inp* (900m thick aquifer layer from 100m below surface to 1000m below surface just below North Pond)
4. Two refinements of elements intersecting surface *1_surf_domain.inp* (bathymetric relief and sediment basement contact the across the entire domain)

5. One refinement of elements with less than two refinements intersecting the volume *7_surf_filt_aq100.inp* (transition from 100 m thick aquifer and 200 m thick aquifer just in North Pond)
6. One refinement of elements with less than two refinements intersecting the surface *7_surf_filt_aq1k.inp* (transition from 1000 m thick aquifer and the conductive basement layer just in North Pond)
7. One refinement of elements with less than two refinements intersecting the surface *7_surf_filt_aq300.inp* (transition from 200 m thick aquifer and 300 m thick aquifer layer just in North Pond)
8. One refinement of elements with less than two refinements intersecting the surface *7_surf_filt_aq600.inp* (transition from 300 m thick aquifer and 400 m thick aquifer layer just in North Pond)
9. One refinement of elements with less than four refinements intersecting the surface *2_surf_mid_grid.inp* (bathymetric relief and sediment basement contact just in and adjacent to North Pond)

Syntax

```
>_ lagrit < 8_driver_high_resolution_clipped.lgi
```

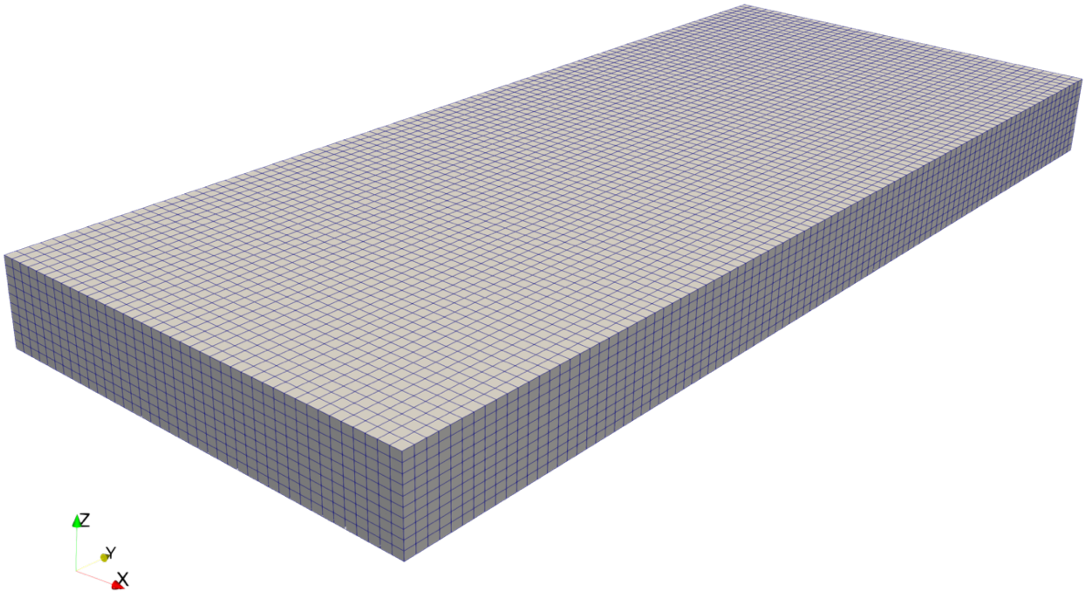

Figure B-13: Initial North Pond hexahedral mesh

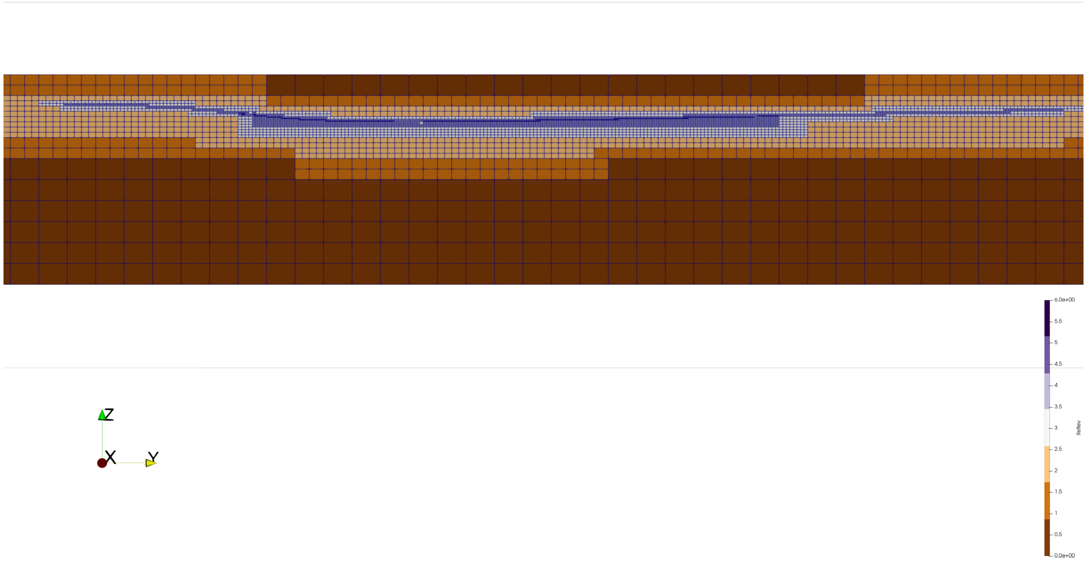

Figure B-14: Refined North Pond mesh subset at x = -6000m, colored by cell refinement level.

Conclusion

Now that we have a mesh that has the correct resolutions in the near- and far-field, we will move on to defining material zones.

- Zone 1: Sedimented pond of North Pond
- Zone 2: 100m thick aquifer layer adjacent but not including North Pond
- Zone 3: 200 m thick aquifer layer adjacent but not including North Pond
- Zone 4: 300 m thick aquifer layer adjacent but not including North Pond
- Zone 5: 400 m thick aquifer layer adjacent but not including North Pond

- Zone 6: Conductive basement layer adjacent but not including North Pond
- Zone 7: 100 m thick aquifer layer immediately adjacent to and including North Pond
- Zone 8: 200 m thick aquifer layer immediately adjacent to and including North Pond
- Zone 9: 300 m thick aquifer layer immediately adjacent to and including North Pond
- Zone 10: 400 m thick aquifer layer immediately adjacent to and including North Pond
- Zone 11: Represents elements and points outside the mesh, defined as not belonging to zones 1-10

However, these zones must be set in the correct order because any subsequent assignment of zones overwrites previous assignments. Therefore, the material zones are assigned in the following order:

1. Zone 11
2. Zone 1
3. Zone 2
4. Zone 3
5. Zone 4
6. Zone 5
7. Zone 6
8. Zone 7

9. Zone 8

10. Zone 9

11. Zone 10

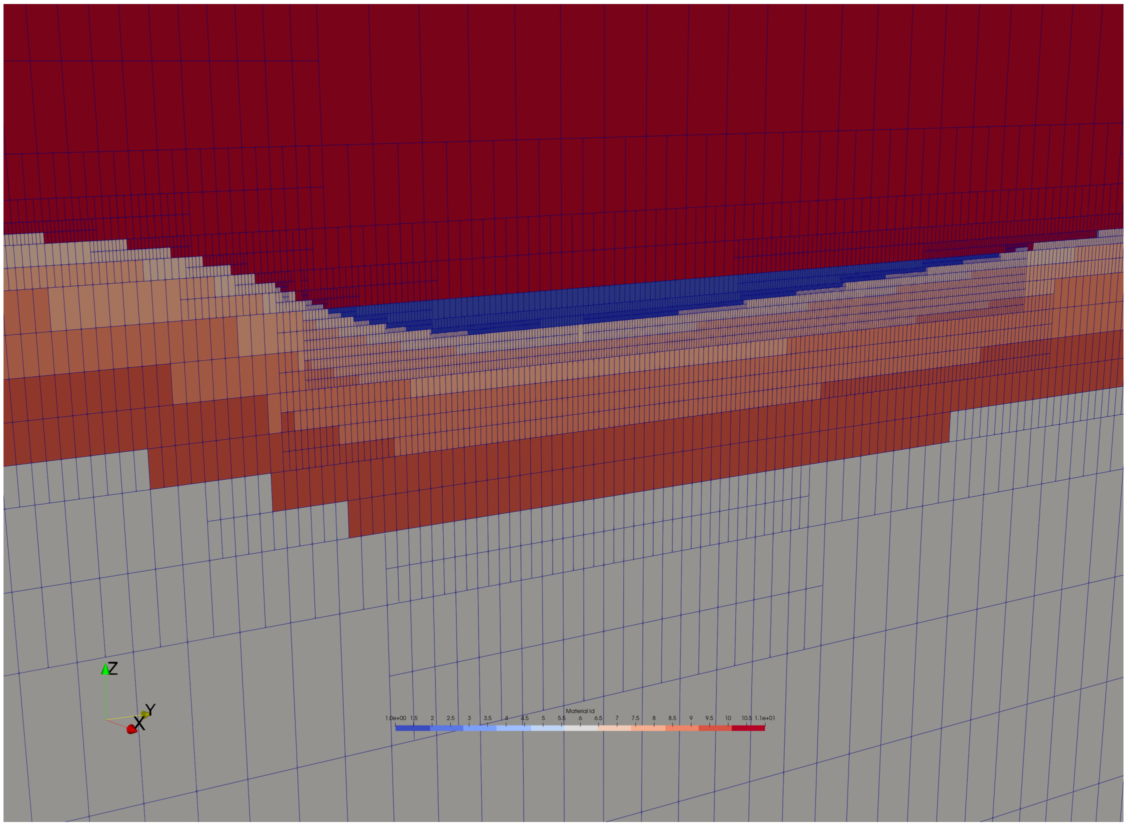

Figure B-15: North Pond hexahedral mesh with material zones defined. 4x vertical exaggeration.

Filename	***Input***	***Output***
12_remove_top.lgi	*11_hex_refine_octree.inp*	*12_tmp_hex_mesh.inp* *12_tmp_tet_interp.inp*

Convert to tetrahedral mesh and remove excess simulation domain

As stated above, the first step is to convert the elements in the mesh from hexahedral to a tetrahedral for use with legacy tools.

Since we started with a rectangular mesh but have refined our mesh to represent a topographic surface, we will remove any elements we do not want to simulation. In the above step, we set Zone 11 to represent this area of the mesh outside the area of interest.

Syntax

```
>_ lagrit < 12_remove_top.lgi
```

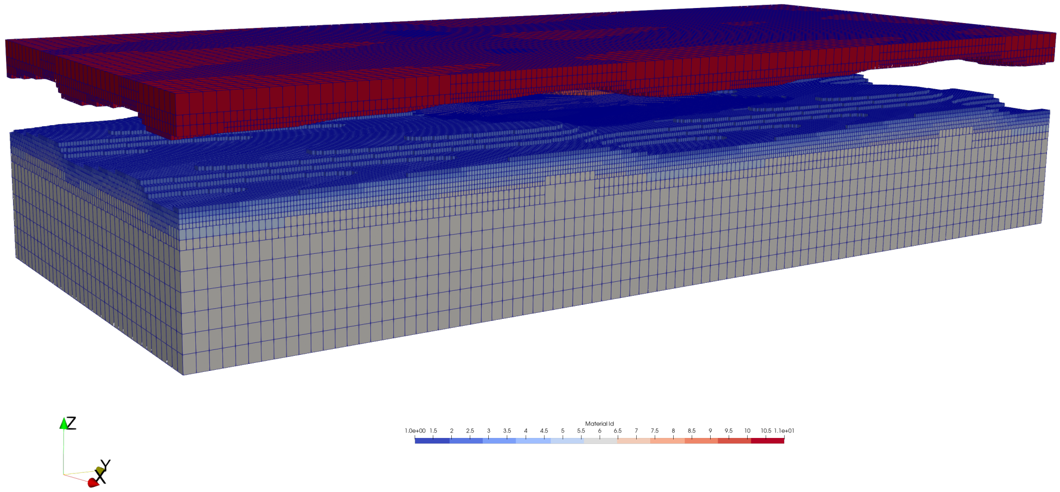

Figure B-16: North Pond hexahedral mesh with top zone being removed. 4x vertical exaggeration.

Filename	**Input**	**Output**
13_top_region_set.lgi	*12_tmp_tet_interp.inp*	*13_tet_reset_final.inp*
		{fehm.files}

Reset top zone of domain

The final step is to correctly assign zones that represent the top, bottom, and side of the mesh. Since we removed what was the top of the mesh in the previous step to reveal the refined topographic surface below, all the elements that were assigned as the top boundary no longer exist. We redefine the top zone of the mesh as elements belonging to the top zone and any material zone greater than one. Additionally, we export files used in Finite Element Heat and Mass Transfer Code (FEHM).

Syntax

```
>_ lagrit < 13_top_region_set.lgi
```

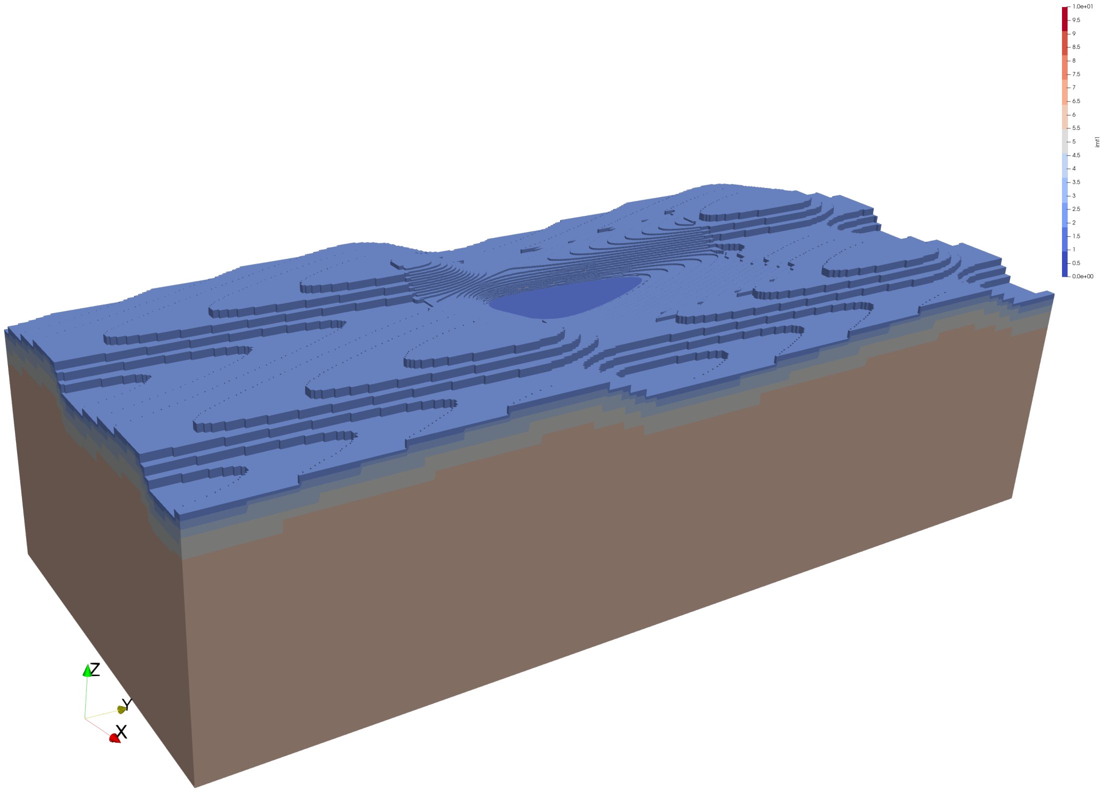

Figure B-17: North Pond tetrahedral mesh with top region set. 4x vertical exaggeration.

Conclusion

This concludes the walkthrough portion of the tutorial. The next pages will cover the final geologic meshes, pseudo code for both cases and an executable roadmap for each case.

Final mesh

Final Generalized Mesh

The general case mesh reproduces common topographic features with targeted refinement along areas of possible simulation intertest. This is a general case and therefore represents a proof of concept.

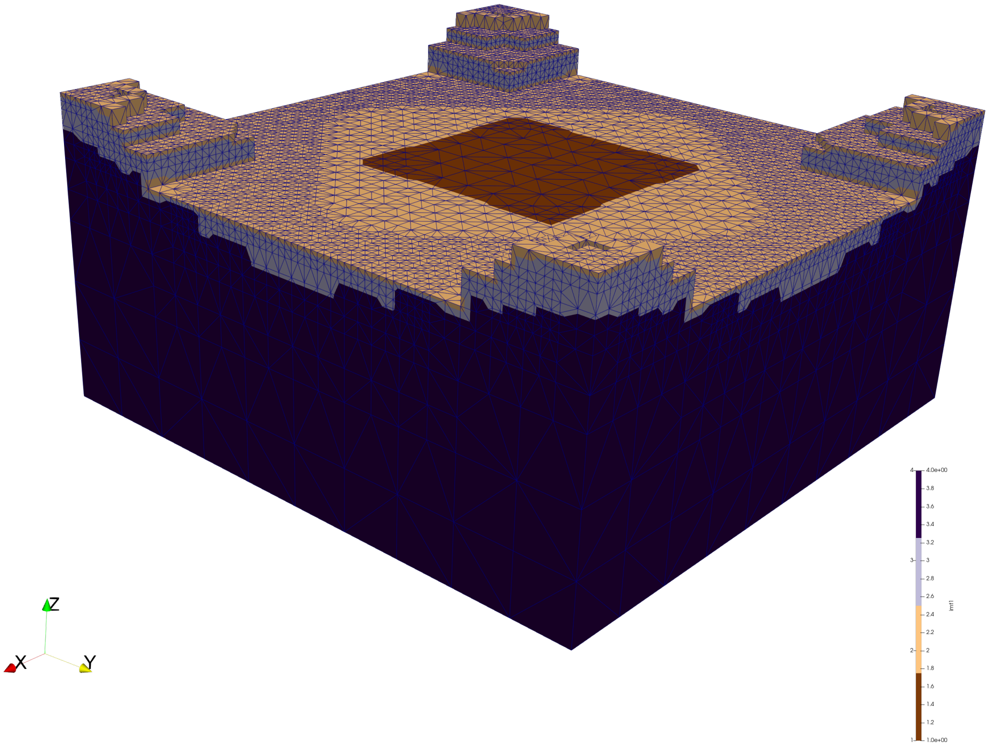

Figure B-18: Final tetrahedral general case mesh

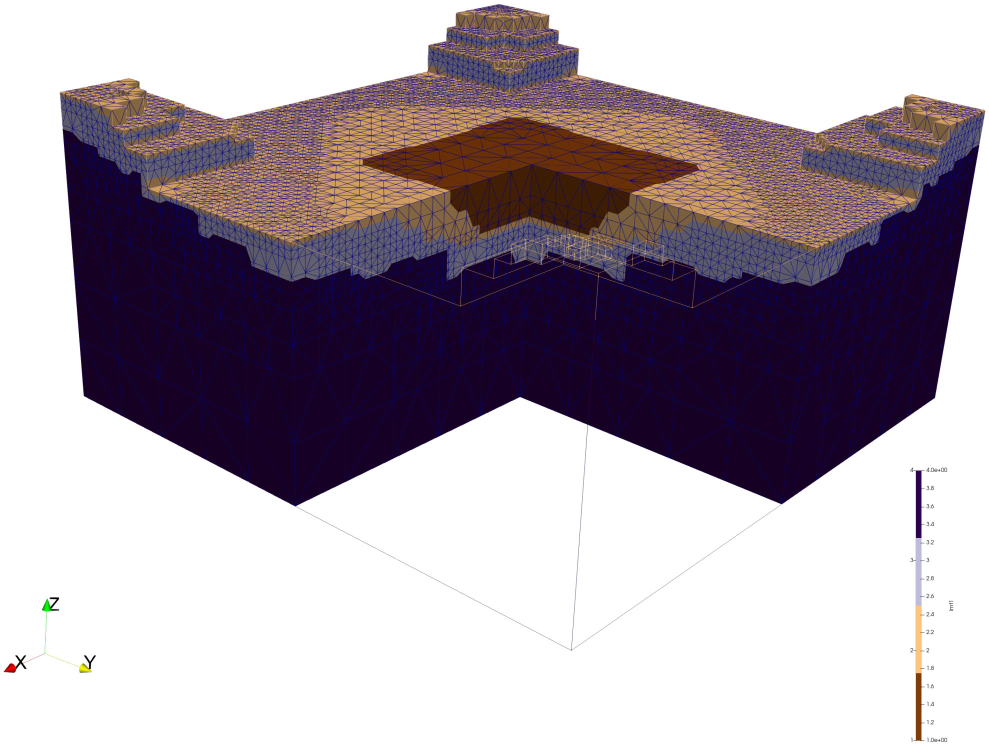

Figure B-19: Final tetrahedral general case mesh with cutaway showing topographic low and material zones.

North Pond

The final North Pond mesh reproduces important characteristics that we sought to reproduce in the mesh.

First, a layered system with separate regions representing seafloor sediments, upper-volcanic crustal aquifer of varying thicknesses, and a lower volcanic unit of conductive crust. Using the aquifer thickness as a “free parameter” in numerical simulations, allows assignment of a thicker or thinner unit in order to better represent heat and fluid flux processes. Price et al., 2022.

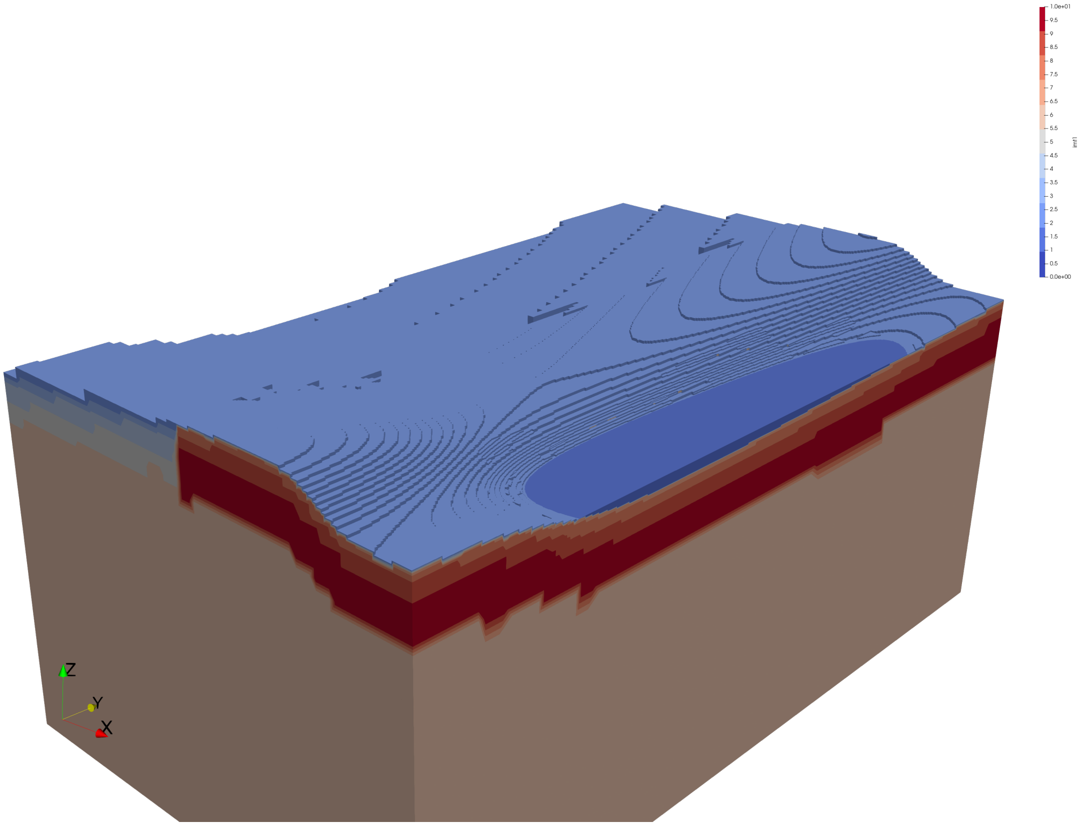

Figure B-20: North Pond mesh with layers representing sediment, conductive basement, and aquifer layers with varying thickness.

Second, geologic geometry that accurately represents the regional and local bathymetry relief. Which we see in the figure below, matches the wavelength and amplitude described in the accompanying publication and Price et al., 2022.

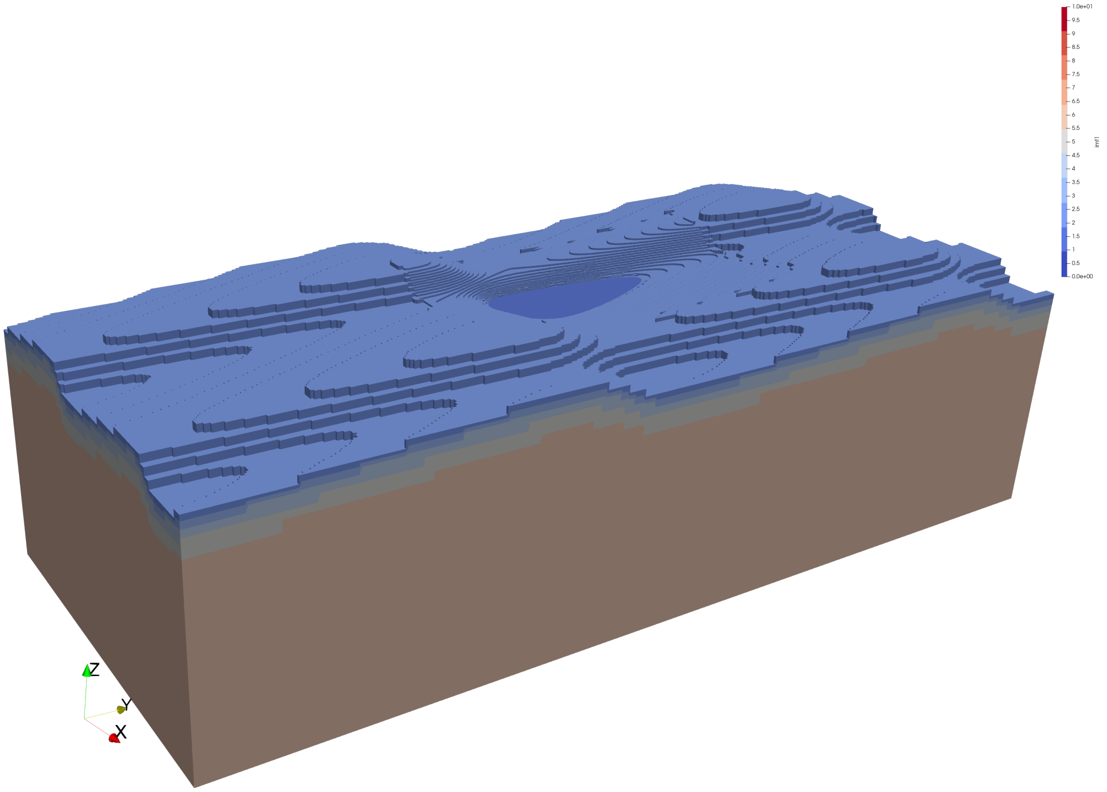

Figure B-21: Final North Pond tetrahedral mesh. 4x vertical exaggeration.

Finally, realistic geometry of the sedimented pond with varying sediment thicknesses, asymmetric slopes along the sediment / basement contacts, and sediment "pinchouts" or thinning sediments along the margins of the sedimented pond.

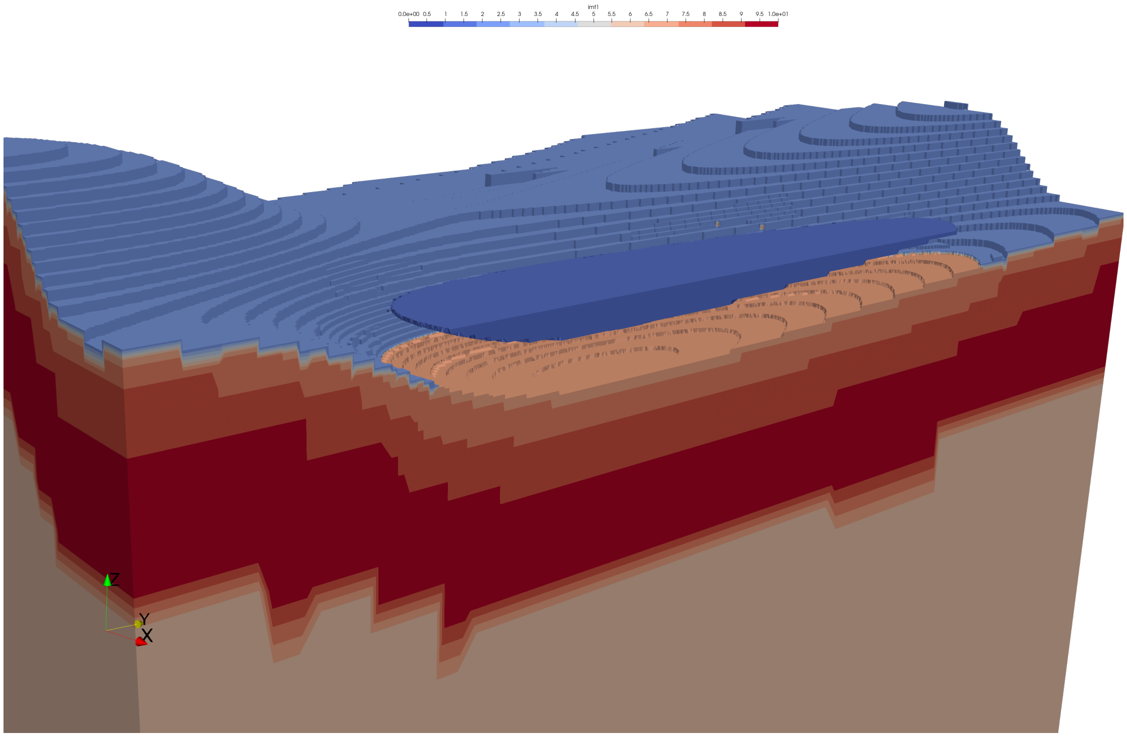

Figure B-22: Final North Pond tetrahedral mesh with sediment pond offset from aquifer layer to show asymmetric slopes and sediment thickness. 4x vertical exaggeration.

<u>Pseudo code: General Case</u>

General files description

Filename	File purpose
1_create_surface.lgi	*Constructing reference surfaces*
2_refine_domain.lgi	*Mesh building and refinement*
3_set_region_truncate.lgi	*Setting material regions based on surfaces, hex-to-tet mesh, removing top of mesh, setting top most zone, cleaning up mesh*

1_create_surface.lgi

Input	Output
2_middle_grid.csv	*2_surf_mid_grid.inp*

Overview

Create all surfaces needed in construction, refinement, and material assignment of general case mesh.

Lines 1 - 6

Assign coordinate system in meters from xmin, ymin, zmin = -5000,-5000 to xmax, ymax = 5000,5000 and number of points in x,y = 201,201.

Lines 9 - 13

Create mesh object *mo_surface* that has the above x and y dimensions with z = 0 and connect the points in the surface

Lines 16 - 21

Create mesh object *surface_plane* from surface *surface.csv*. Then copy over z coordinates from *surface_plane* to connected surface *mo_surface*

Lines 24 - 30

Set properties assocaited with surface (mostly used for visualization in this case) and dump mesh object surface *mo_surface* to *1_surface.inp*

Lines 34 - 54

Create copies of *mo_surface* named *mo_aq800* and *mo_aq200*. Subtract 200m and 800m from the z coordinate of surfaces *mo_aq200* and *mo_aq800*; respectively. Set properties associated with surface, and dump mesh objects to files - *mo_aq200* to *1_surface_aq200.inp* - *mo_aq800* to *1_surface_aq800.inp*

Lines 58 - 74

Create mesh object *mo_zero* at z = 0 with two points in x and y with the same extent as specified above. Set properties associated with surface and dump *mo_zero* to file *1_surface_zero.inp*.

2_refine_domain.lgi

Input	**Output**
2_middle_grid.csv	*2_surf_mid_grid.inp*

Overview

First, we create an initial hexahedral mesh. Next, we read in all the surfaces created in the previous files. Finally, the subroutine *refine_object.mlgi* is called to perform octree refinement along the elements intersected with the surfaces called and files are created for each of those refinement iterations.

Lines 2 - 14

Define xmin, ymin, zmin = -5000,-5000, -4000 to xmax, ymax, zmax = 5000,5000,1000 and number of points in x,y,z = 11,11,6. This sets the initial resolution at 1000m elements in x,y,z. Create the mesh object *domain_hex* and dump to file *2_initial_domain.inp*.

Lines 16 - 18

Read in surfaces

- 1_surface.inp = mo_surface

- 1_surface_aq200.inp = mo_aq200

- 1_surface_aq800.inp = mo_aq800

Line 23

Define the initial hexahedral mesh *domain_hex* as the object to refine.

Lines 24 - 27

This series of lines performs the octree refinement and will be performed many times in this file. The flow of these lines is:

- Line 24: Define the mesh object to refine with. Here is *mo_sb*
- Line 25: Perform octree refinement via the subroutine *refine_object.mlgi*
- Line 26: Dump the refined object to a file. Here *2_surface_octree.inp*
- Line 27: Check the quality of the refinement.

Henceforth, this series of steps will be denoted by: Refine {*name of mesh object*} - File: {*Output file*}

Lines 29 - 34

Refine x2 mo_aq200 - File: 2_surfaceAQ200_octree.inp

Lines 36 - 40

Refine mo_aq800 - File: 2_surfaceAQ800_octree.inp

Lines 45 - 46

Reset the *itetclr* variable. Dump the refined mesh *domain_hex* to file *2_hexRefine_octree.inp*

Refine_object.mlgi

Input	**Output**
{Element to be refined}	*{Refining element}*

Overview

Subroutine used to perform octree refinement of a mesh object along a specified surface or volume

Lines 1 - 2 Clear any variables from previous use of subroutine

Line 4 Create a mesh object attribute named *if_inter* that contains the intersection of the mesh object being refined and the mesh object being used to refine in this step. These are defined outside the subroutine

Line 5 Create an element set named *erefine* based on where *if_inter* is greater than 0 (i.e., where the meshes intersect)

Line 6 The selected set, *erefine,* is refined.

3_set_region_truncate.lgi

Input	Output
2_hexRefine_octree.inp	*3_hexDomain_defineZones.inp*
1_surface.inp	*{outside zone files}*
1_surface_aq200.inp	*3_tetDomain_regionSet.inp*
1_surface_aq800.inp	
1_surface_zero.inp	

Overview

Line 1

Read in refined mesh *2_hexRefine_octree.inp* as mesh object *domain_hex*

Lines 3 - 11

Read in surfaces as sheet surfaces as follows:

- *1_surface.inp* as sheet surface *surf*
- *1_surface_aq200.inp* as sheet surface *s_aq200*
- *1_surface_aq800.inp* as sheet surface *s_aq800*
- *1_surface_zero.inp* as sheet surface *zero*

Lines 13 - 14

Set attribute *itetclr* = 5 for mesh *domain_hex*

Lines 17 - 37

This section details the intersecting of sheets above with the refined mesh object in order to define individual zones that correspond to geologic units within the grid. The general workflow of this section takes example from Lines 33 - 35:

- Line 33 - Define the region of interest and name it *r1* which is less than or equal to the sheet zero and greater than the surface *surf*. (surf < r1 ≤ zero)
- Line 34 - Define an eltset (element set), *e_r1*, from the region *r1*.
- Line 35 - Set the itetclr attribut of *domain_hex* = 1

This process repeats for different conditions until line 37. The layers that correspond to the itetclr set in these lines are:

- 1 - Sediment
- 2 - Aquifer layer 0 - 200m
- 3 - Aquifer layer 200 - 800m
- 4 - Conductive basement < 800 m
- 5 - Everything else (i.e., the area above the refined topographic surface)

Lines 39 - 43

Check the quality of *domain_hex* and dump to file *3_hexDomain_defineZones.inp*

Line 45 - 49

Convert hexahedral mesh *domain_hex* to tetrehedral mesh *domain_tet* for ease of use for legacy tools from UCSC hydrogeology lab GitHub

Line 52 - 60

Reset imt and itp attributes for mesh *domain_tet*. Interpolate material regions from *domain_hex* to *domain_tet*. Dump mesh *domain_tet* to file *3_tetDomain_topConnected.inp*

Line 63 - 64

Remove material zone 5 corresponding to elements above refined topography.

Line 67 - 70

Reset attributes *cell_color* and *itp*. Check status of mesh

Line 73 - 78

Dump outside zone files to read back in later steps. Select points with material zone (imt) greater than 1 and in the top zone for mesh *domain_tet* and set attribute imt to zone 2.

Line 81

Dump completed mesh domain_tet to file 3_tetDomain_regionSet.inp

Pseudo code: North Pond

General files description

Filename	File purpose
1_surf_domain.lgi	Construct reference surfaces
2_surf_mid_grid.lgi	Construct reference surfaces
3_surf_mid_sb.lgi	Construct reference surfaces
4_surf_flat_zero.lgi	Construct reference surfaces
5_surf_aq100.lgi	Construct reference surfaces
6_surf_aq300_1k.lgi	Construct reference surfaces
7_surf_filt.lgi	Construct reference surfaces
8_driver_high_resolution_clipped.lgi	Mesh building and refinement
9_surf_north_pond_seafloor.lgi	Construct reference surfaces
10_surf_aq_volumes.lgi	Constructing reference volumes
11_region_set.lgi	Setting material regions based on surfaces/volumes
12_remove_top.lgi	Hex-to-tet mesh and removing top of mesh
13_top_region_set.lgi	Setting topmost zone, cleaning up mesh, exporting FEHM files

Files:

Function6.csv: CSV file with x,y,z of function representing bathymetry and sediment-basement contact

2_mid_grid.csv: Clipped bathymetry file representing North Pond and surrounding area. Used for high resolution filtering

3_middle_sb.csv: Clipped bathymetry file representing just the sediment = basement interface.

1_surf_domain.lgi

Input	**Output**
function6	*1_surf_domain.inp*

Overview

Create mesh object for bathymetric surface.

Lines 1 - 11

Assign coordinate system in meters from xmin, ymin, zmin = -30000,-75000, -5000 to xmax, ymax, zmax = 30000,75000,0 and number of points in x,y,z = 301, 301,6 to determine spacing.

Lines 14 - 18

Create a mesh object surface, *mo_tri*, that is the above x,y dimensions with singular z value (2D plane). Setting z coordinates to zero before connecting allows defining an explicit x,y coordinate system and connecting that surface without producing oddly shaped elements.

Lines 23-24

Creates mesh object (*sedbase*) from the topography function from R (*function6*)

Line 28

Assign z coordinates from *sedbase* to connected triplane mesh object *mo_tri*

Lines 32 - 37

Reset property values of mesh object to insure all the same value

Lines 39 - 41

Dump surface to file *1_surf_domain.inp*

2_surf_mid_grid.lgi

Input	Output
2_middle_grid.csv	*2_surf_mid_grid.inp*

Overview

Create mesh object from trimmed area of interest created from truncated bathymetric surface representing North Pond and immediately adjacent region created outside of LaGriT

Lines 4 - 8

Read in *2_middle_grid.csv,* create a mesh object (*sedbase*), set z coordinates to zero, then connect. Setting z coordinates to zero before connecting allows defining an explicit x,y coordinate system and connecting that surface without producing oddly shaped elements.

Lines 10 - 14

Read in *2_middle_grid.csv*, create a separate mesh object *temp*, then copy z coordinates from temp to connected surface *sedbase*.

Lines 17 - 22

Reset property values of mesh object to insure all the same value

Lines 26 - 28

Dump surface to file *2_surf_mid_grid.inp*

3_surf_mid_sb.lgi

Input	Output
3_middle_sb.csv	*3_surf_mid_sb.inp*

Overview

Create mesh object from trimmed area of interest created from truncated bathymetric surface representing sediment = basement interface beneath North Pond created outside of LaGriT

Lines 4 - 8

Read in *3_middle_sb.csv,* create a mesh object (*sedbase*), set z coordinates to zero, then connect. Setting z coordinates to zero before connecting allows defining an explicit x,y coordinate system and connecting that surface without producing oddly shaped elements.

Lines 10 - 13

Read in *3_middle_sb.csv,* create a separate mesh object (*temp*), then copy z coordinates from temp to connected surface *sedbase*

Lines 17 - 22

Reset property values of mesh object to insure all the same value

Lines 26 - 28

Dump surface to file *3_surf_mid_sb.inp*

4_surf_flat_zero.lgi

Input	Output
None	*4_surf_flat_zero.inp*

Overview

Construct a flat surface at z = 0 at the same spatial extent as *2_middle_grid.csv*.

Lines 2 - 5

Specify extent of surface xmin, ymin = -15000, -6000 to xmax, ymax = 4600, 28500

Lines 7 - 9

Specify number of x,y points (resolution) at 2 each

Lines 11 - 15

Create mesh object *mo_tri*, create points on that mesh object, and connect

Lines 17 - 18

Check quality of connections for oddly shaped elements

Lines 20 - 22

Dump mesh object *mo_tri* to file *4_surf_flat_zero.inp*

5_surf_aq100.lgi

Input	**Output**
3_surf_mid_sb.inp	*5_surf_aq100.inp*

Overview

Construct a volume that represents a 100m thick aquifer section directly beneath North Pond.

Line 1

Read in *3_surf_mid_sb.inp* to mesh object *mid_sb*

Line 4

Extrude a volume that goes from sediment = basement interface to 100m below that interface.

Line 6

Check the quality of the extrude

Lines 9 - 11

Convert the volume from hexagonal elements to tetrahedral elements and check the quality of that conversion

Lines 13 - 15

Dump *mo_tet* to file *5_surf_aq100.inp*

6_surf_aq300_1k.lgi

Input	**Output**
2_surf_mid_grid.inp	*6_surf_aq300_1k.inp*

Overview

Construct a volume that represents a 900 m thick aquifer section directly beneath the region representing North Pond.

Lines 2 - 4

Read in *2_surf_mid_grid.inp* to mesh object *mo* and subtract 100m from all z coordinates.

Lines 6 - 8

Extrude *mo* surface to a volume *mo_long* that goes from 100 - 1000m below *2_surf_mid_grid.inp* surface representing local North Pond bathymetry.

Lines 10 - 13

Convert the volume from hexagonal elements, *mo_long,* to tetrahedral elements, *mo_tet,* and check the quality of that conversion.

Lines 15 - 17

Dump *mo_tet* to file *6_surf_aq300_1k.inp*

7_surf_filt.lgi

Input	Output
1_surf_domain.inp	*7_surf_filt_aq100.inp*
	7_surf_filt_aq300.inp
	7_surf_filt_aq600.inp
	7_surf_filt_aq1k.inp

Overview

Construct four surfaces at -100, -300, -600, and -1000m at the extent of the entire domain.

Line 1

Read in *7_surf_filt.lgi* to mesh object *mo*

Lines 4 - 7

Create copies of *mo* to:

- mo_aq100
- mo_aq300
- mo_aq600
- *mo_aq1k*

Lines 12 - 15

Subtract 100, 300, 600, and 1000m from the z coordinates of the copied mesh objects respectively and check the quality of those objects

Lines 20 - 25

Dump mesh objects to files:

- mo_aq100 to 7_surf_filt_aq100.inp
- mo_aq300 to 7_surf_filt_aq300.inp
- mo_aq600 to 7_surf_filt_aq600.inp
- mo_aq1k to 7_surf_filt_aq1k.inp

8_driver_high_resolution_clipped.lgi

Input	**Output**
1_surf_domain.inp	*8_1_octree_NP.inp*
3_surf_mid_sb.inp	*8_2_octree_aq100.inp*
4_surf_flat_zero.inp	*8_3_octree_aq300.inp*
5_surf_aq100.inp	*8_4_octree_dom.inp*
6_surf_aq300_1k.inp	*8_4_octree_domaq100.inp*
7_surf_filt_aq100.inp	*8_5_octree_domaq1k.inp*
7_surf_filt_aq300.inp	*8_6_octree_domaq300.inp*
7_surf_filt_aq600.inp	*8_7_octree_domaq600.inp*
7_surf_filt_aq1k.inp	*8_hex_refine_octree.inp*

Overview

This file is the key file in building the domain. First, we read in all the surfaces created in the previous files. Next, the subroutine *refine_object.mlgi* is called to perform octree refinement along the elements intersected with the surfaces called and files are created for each of those refinement iterations. The final file with refinements along all desired surfaces is dumped to *8_hex_refine_octree.inp*

Lines 1 - 14

Define xmin, ymin, zmin = -24000,-40000, -6000 to xmax, ymax, zmax = 16000,55000,1500 and number of points in x,y,z = 41, 96,11. This sets the initial resolution at 1000m elements in x,y and 750m in z. Create the mesh object *mo_hex* for refinement.

Lines 17 - 25

Read in surfaces:

- 1_surf_domain.inp = domain
- 4_surf_flat_zero.inp = sf_zero
- 5_surf_aq100.inp = aq100
- 6_surf_aq300_1k.inp =aq300_1k
- 3_surf_mid_sb.inp = mo_sb
- 7_surf_filt_aq100.inp = domain_aq100
- 7_surf_filt_aq1k.inp = domain_aq1k
- 7_surf_filt_aq600.inp = domain_aq600
- *7_surf_filt_aq300.inp = domain_aq300*

Line 28

Define the mesh object *mo_hex* as the object to perform octree refinement on

Lines 32 - 36

This series of lines performs the octree refinement and will be performed many times in this file. The flow of these lines are:

- Line 32: Define the mesh object to refine with. Here is *mo_sb*
- Line 33: Perform octree refinement via the subroutine *refine_object.mlgi*
- Line 34: Dump the refined object to a file. Here *8_1_octree_NP.inp*
- Line 36: Check the quality of the refinement.

Henceforth, this series of steps will be denoted by: Refine {*name of mesh object*} - File: {*Output file*}

Lines 40 - 43

Refine *aq100* - File: *8_2_octree_aq100.inp*

Lines 47 - 52

Refine x2 *aq300_1k* - File: *8_3_octree_aq300.inp*

Lines 57 - 60

Refine x2 *domain* - File: *8_4_octree_dom.inp*

Lines 64 - 75

Refine *domain_aq100* - File: *8_4_octree_domaq100.inp*

This refinement has a few additional steps outside the subroutine but before dumping the mesh object.

- Line 68: Create a mesh object attribute named *in_inter* that contains the intersection of the mesh object being refined and mesh object being used to refine in this step
- Line 69: Create an element set named *erefine1* based on where *in_inter* is greater than 0 (i.e., where the meshes intersect)
- Line 70: Create an element set named *num_ref1* based on elements that have been refined less than 2 times.
- Line 71: Create an element set named *combined1* that is the union of elements from *erefine1* and *num_ref1*
- Line 72: Refine the element set *combined1*

These lines are very similar to the subroutine *refine_object.mlgi* with the caveat that we are also imposing an additional condition that we only want to refine elements that have 1 level of refinement. This ensures that we are not over-refining elements creating a computationally intensive simulation grid. Henceforth, we will refer to this process as *itet-refine*

Lines 79 - 91

Refine *domain_aq1k* - File: *8_5_octree_domaq1k.inp* plus *itet-refine*

Lines 96 - 108

Refine *domain_aq300* - File: *8_6_octree_domaq300.inp* plus *itet-refine*

Lines 112 - 126

Refine *domain_aq600* - File: *8_7_octree_domaq600.inp* plus *itet-refine*

Lines 128 - 142

Read in surface *2_surf_mid_grid.inp* to mesh object *mid_grid*. Perform a itet-refine on elements with less than 4 refinements (itetlev < 4).

Line 144

Reset all elements to color 7

Lines 146 - 151

Dump *mo_hex* to *8_hex_refine_octree.inp*

Input	**Output**
refine_object.mlgi	*{Element to be refined}*

Overview

Subroutine used to perform octree refinement of a mesh object along a specified surface or volume

Lines 1 - 2

Clear any variables from previous use of subroutine

Line 4

Create a mesh object attribute named *if_inter* that contains the intersection of the mesh object being refined and the mesh object being used to refine in this step. These are defined outside the subroutine

Line 5

Create an element set named *erefine* based on where *if_inter* is greater than 0 (i.e., where the meshes intersect)

Line 6

The selected set, *erefine,* is refined. ### **File link:**

9_surf_north_pond_seafloor.lgi

Input	Output
3_middle_sb.csv	*9_surf_north_pond_seafloor.inp*

Overview

Make a surface corresponding to x,y coordinates of North Pond sediment with z coordinates = 0

Lines 4 - 8

Create triplane mesh object *sedbase*. Read in *3_middle_sb.csv* as the x,y,z coordinates of *sedbase*. Set z-coordinates = 0 and connect points

Lines 11 - 15

Reset all material and color properties associated with *sedbase*

Lines 19 - 21

Dump mesh object *sedbase* to *9_surf_north_pond_seafloor.inp*

10_surf_aq_volumes.lgi

Input	Output
2_surf_mid_grid.inp	*10_surf_filt_mid_grid_aq100.inp*

Overview

Construct volumes corresponding to the aquifer units beneath North Pond and the adjacent region.

Line 2

Read in *2_surf_mid_grid.inp* as mesh object *mo*

Lines 5 - 11

Create copies of mesh object *mo*. Check quality and status.

Lines 13 - 28

Create volumes corresponding to aquifer layers beneath North Pond. Example syntax is:

- Line 13 - Subtract 100m from z-coordinate of mesh object *mo_aq100*
- Line 14 - Extrude *mo_aq100* in the positive z-coordinate direction 100m and name *mo_aq100long*

Repeat these steps for layers mo_aq300long (100m - 300m below *mo*), mo_aq600long (300m - 600m below *mo*), and mo_aq1klong (600m - 1000m below *mo*). Check status and quality of volumes.

Lines 30 - 33

Set attribute icr for volumes

Lines 35 - 38

Dump mesh objects to files:

- mo_aq100long to 13_surf_filt_mid_grid_aq100.inp
- mo_aq300long to 13_surf_filt_mid_grid_aq300.inp
- mo_aq600long to 13_surf_filt_mid_grid_aq600.inp
- mo_aq1klong to 13_surf_filt_mid_grid_aq1k.inp

11_region_set.lgi

Input	**Output**
8_hex_refine_octree.inp	*11_hex_refine_octree.inp*
1_surf_domain.inp	
4_surf_flat_zero.inp	
7_surf_filt_aq100.inp	
7_surf_filt_aq300.inp	
7_surf_filt_aq600.inp	
7_surf_filt_aq1k.inp	
3_surf_mid_sb.inp	
9_surf_north_pond_seafloor.inp	
10_surf_filt_mid_grid_aq100.inp	
10_surf_filt_mid_grid_aq300.inp	
10_surf_filt_mid_grid_aq600.inp	
10_surf_filt_mid_grid_aq1k.inp	

Overview

Read in previously made surfaces and set regions corresponding to layered seafloor units

Lines 1 - 30

Read in hexahedral mesh *8_hex_refine_octree.inp* as *mo_hex*. Read in surfaces and convert to sheets surfaces in order to intersect with elements and filter material zones:

- 1_surf_domain.inp = domain
- 4_surf_flat_zero.inp = sf_zero
- 7_surf_filt_aq100.inp = mo_aq100
- 7_surf_filt_aq300.inp = mo_aq300
- 7_surf_filt_aq600.inp = mo_aq600
- 7_surf_filt_aq1k.inp = mo_aq1k
- 3_surf_mid_sb.inp = mo_sb
- 9_surf_north_pond_seafloor.inp = np_sea
- 10_surf_filt_mid_grid_aq100.inp = mo_aq100b
- 10_surf_filt_mid_grid_aq300.inp = mo_aq300b
- 10_surf_filt_mid_grid_aq600.inp = mo_aq600b
- 10_surf_filt_mid_grid_aq1k.inp = mo_aq1kb

Lines 33 - 34

Select the refined simulation domain as the mesh object and attribute itetclr = 11. This attribute is what we will use to define material zones

Lines 37 - 84

This section details the intersecting of sheets above with the refined mesh object in order to define individual zones that correspond to geologic units within the grid. The general workflow of this section takes example from Lines 33 - 35:

- Line 37 - Define the region of interest and name it *r1* which is less than or equal to the sheet zero and greater than the surface *s_sb*. (s_sb < r1 ≤ zero)
- Line 38 - Define an element set, *e_r1*, from the region *r1*.
- Line 39 - See the itetclr of *mo_hex* = 1

This process repeats for different conditions until line 81. The layers that correspond to the itetclr set in these lines are:

- 1 - Sediment
- 2 - Aquifer layer 0 - 100m
- 3 - Aquifer layer 100 - 300m
- 4 - Aquifer layer 300 - 600m
- 5 - Aquifer layer 600 - 1000m
- 6 - Conductive basement
- 7 - Aquifer volume 100m (*mo_aq100b*)
- 8 - Aquifer volume 300m (*mo_aq300b*)
- 9 - Aquifer volume 600m (*mo_aq600b*)
- 10 - Aquifer volume 1km (*mo_aq1kb*)

Lines 89 - 97

Specify conditionals to set itetclr = 1 for all elements above *zero* and *sf* sheets. This is done very similarly to lines 27 - 58 and quality of elements is checked. This step makes sure no elements are taken out of the seafloor of North Pond.

Line 99

Dump mesh object *mo_hex* to file *11_hex_refine_octree.inp*

12_remove_top.lgi

Input	**Output**
11_hex_refine_octree.inp	*12_tmp_hex_mesh.inp*
	12_tmp_tet_interp.inp

Overview

Translate mesh with hexahedral elements to mesh with tetrahedral elements. Filter and remove domain area above North Pond and bathymetric surface. Translate regions set in *11_region_set.lgi* to tetrahedral mesh.

Line 1

Read in hexagonal mesh file *11_hex_refine_octree.inp* to mesh object *mo_octree*

Line 2

Convert hexagonal mesh *mo_octree* to "clean" hexagonal mesh *mo_hex*, and check quality. From LaGriT manual:

"Parent elements in octree_mesh will be removed, so only the leaf elements remain. The result will be stored in new_mesh. This is often used to ensure a single valid mesh for other commands or for use outside of LaGriT. The octree attributes itetpar, itetkid, and itetlev will be updated in the new_mesh."

Line 6

Dump *mo_hex* to file *12_tmp_hex_mesh.inp*

Line 8 - 14

Create new tetrahedral mesh object *mo_tet* and copy points from *mo_hex*. Set imt and itp attributes as constant for *mo_tet* and connect points

Lines 18 - 19

Interpolate the cell colors from *mo_hex* to *mo_tet*.(i.e., material zones)

Lines 21 - 22

Remove all of itetclr = 11 (i.e. region above North Pond and refined bathymetry) and remove any points without connections resulting from the removal.

Lines 26 - 27

Replace the node material (imt) with the corresponding cell color (itetclr) as well as set node type (itp) based on itetclr.

Lines 29 - 34

Check the quality of the mesh. Dump *mo_tet* to file *12_tmp_tet_interp.inp*.

13_top_region_set.lgi

Input	**Output**
12_tmp_tet_interp.inp	*13_tet_reset_final.inp*
	{zone files}
	{fehm files}

Overview

Set top region of North Pond to correct for removal of top of domain in *11_price_remove_top.lgi*. Reorder and sort nodes within simulation grid

Lines 1 - 4

Read in *12_tmp_tet_interp.inp* as mesh object *mo* and check status

Line 6

Dump outside zone numbers to zone files *tmp_test_outside_vor.area* and *tmp_test_outside.zone*

Lines 8 - 9

Define attribute node_num from node numbers from mesh object *mo* and check status

Lines 11 - 15

Filter points that lie on the top of the simulation domain given conditionals:

- Line 11 - Find points with "imt" attribute greater than 1 (i.e., points not in conductive basement) name them *todos*
- Line 12 - Find points with "top" attribute greater than 1 (i.e., points belonging to top zone) name them *ttop*
- Line 13 - Find the points that below to both of these point sets, name them *filter*
- Line 14 - Set imt = 2 to *filter* points in *mo*

Check the status and quality of steps above

Lines 19 - 21

Sort nodes based on the rank of the node number, then x-, y-, and z-coordinate respectively. Then reorder the nodes based on the sorting.

Lines 23 - 24

Dump the mesh object *mo* to file *13_tet_reset_final.inp*

Execute Scripts

Generalized Mesh

Syntax

```
>_ lagrit< 1_create_surface.lgi &&

    lagrit < 2_refine_domain.lgi &&

    lagrit < 3_set_region_truncate.lgi
```

North Pond

Syntax

```
>_ lagrit < 1_surf_domain.lgi &&

    lagrit < 2_surf_mid_grid.lgi &&

    lagrit < 3_surf_mid_sb.lgi &&

    lagrit < 4_surf_flat_zero.lgi &&

    lagrit < 5_surf_aq100.lgi &&

    lagrit < 6_surf_aq300_1k.lgi &&

    lagrit < 7_surf_filt.lgi &&

    lagrit < 8_driver_high_resolution_clipped.lgi &&

    lagrit < 9_surf_north_pond_seafloor.lgi &&

    lagrit < 10_surf_aq_volumes.lgi &&

    lagrit < 11_region_set.lgi &&

    lagrit < 12_remove_top.lgi &&

    lagrit < 13_top_region_set.lgi
```